ISTANBUL TECHNICAL UNIVERSITY ★ GRADUATE SCHOOL

A STATISTICAL ANALYSIS OF IONOSPHERIC JOULE HEATING DRIVEN BY INTERPLANETARY CORONAL MASS EJECTIONS AND HIGH SPEED STREAMS USING SWMF/BATS-R-US MHD MODEL

M.Sc. THESIS

Pelin ERDEMİR

Department of Meteorological Engineering

Atmospheric Sciences Programme

JULY 2022

ISTANBUL TECHNICAL UNIVERSITY ★ GRADUATE SCHOOL

A STATISTICAL ANALYSIS OF IONOSPHERIC JOULE HEATING DRIVEN BY INTERPLANETARY CORONAL MASS EJECTIONS AND HIGH SPEED STREAMS USING SWMF/BATS-R-US MHD MODEL

M.Sc. THESIS

Pelin ERDEMİR
(511191032)

Department of Meteorological Engineering

Atmospheric Sciences Programme

Thesis Advisor: Prof. Dr. Zerefşan KAYMAZ

JULY 2022

ISTANBUL TEKNİK ÜNİVERSİTESİ ★ LİSANSÜSTÜ EĞİTİM ENSTİTÜSÜ

SWMF/BATS-R-US MHD MODELİ KULLANILARAK GEZEGENLERARASI KORONAL KÜTLE ATIMLARI VE YÜKSEK HIZLI AKIŞLAR TARAFINDAN GELİŞEN İYONOSFERİK JOULE ISINMASININ İSTATİSTİKSEL ANALİZİ

YÜKSEK LİSANS TEZİ

Pelin ERDEMİR
(511191032)

Meteoroloji Mühendisliği Anabilim Dalı

Atmosfer Bilimleri Programı

Tez Danışmanı: Prof. Dr. Zerefşan KAYMAZ

TEMMUZ 2022

Pelin ERDEMİR, a M.Sc. student of İTU Graduate School student ID 511191032, successfully defended the thesis/dissertation entitled "A STATISTICAL ANALYSIS OF IONOSPHERIC JOULE HEATING DRIVEN BY INTERPLANETARY CORONAL MASS EJECTIONS AND HIGH SPEED STREAMS WITH USING SWMF/BATS-R-US MHD MODEL", which he/she prepared after fulfilling the requirements specified in the associated legislations, before the jury whose signatures

Thesis Advisor :	**Prof. Dr. Zerefşan KAYMAZ** İstanbul Technical University	.....
Jury Members :	**Dr. Öğr. Üyesi Dr. Cuma Yarım** Istanbul Technical University	.....
	Prof. Dr. Zafer Aslan Istanbul Aydın University	.....

Date of Submission : 27 May 2022
Date of Defense : 6 July 2022

To my family and friends,

FOREWORD

The Sun, being the source of every thing in our solar system, controls the life on Earth. Without it, we can not be present. However, the variations of the Sun, which is called space weather, could be hazardous if we did not have our atmosphere and magnetosphere. In this work, the effect of different solar phenomena structures and their driven geomagnetic storms on the ionospheric Joule heating has been investigated in detail to fill the gap in the solar wind-magnetosphere-ionosphere system.

First of all, I would like to thank my advisor Prof. Dr. Zerefşan KAYMAZ, who supported me for everything during this study, and also inspired me during my whole academic education since I was registered to the Meteorological Engineering Department of Istanbul Technical University in 2016. She is the first person who showed me that the “space is not empty” and also the person that guided me to find my passion in space weather. Secondly, I also would like to thank very much to Dr. Emine Ceren KALAFATOĞLU EYİGÜLER for her continuous support. She helped me every time when I had troubles with my data, models and results. My thanks also go to our collaborator and co-author in our various papers, Dr. Lutz RASTAETTER, for his help and support when I needed.

This study has been done by using the data provided from institutions and organizations. We acknowledge the use of NASA/GSFC's Space Physics Data Facility's OMNIWeb and CDAWeb service and OMNI data. The Dst and AE indices used in this paper was provided by the WDC for Geomagnetism, Kyoto (http://wdc.kugi.kyoto-u.ac.jp/wdc/Sec3.html). We acknowledge the use of SOHO’s coronagraph data. SOHO is a project of international cooperation between ESA and NASA. In this paper, SDO’s AIA data is used by courtesy of NASA/SDO and the AIA, EVE, and HMI science teams. Simulation results have been provided by the Community Coordinated Modeling Center at Goddard Space Flight Center through their public Runs on Request system (http://ccmc.gsfc.nasa.gov). The SWMF/BATS-R-US with CRCM Model was developed by Tamas Gombosi et al., Mei-Ching Fok et al., Gabor Toth et al. at the The Center for Space Environment Modeling (CSEM). We acknowledge use of the SWMF and BATS-R-US tools developed at the University of Michigan's Center for Space Environment Modeling (CSEM). The modeling tools described in this publication are available online through the University of Michigan for download and are available for use at the Community Coordinated Modeling Center (CCMC). I would like to thank to the CCMC scientists; Dr. Anne Michelle Mendoza and Dr. Maksym Petrenko for providing continuous support about all of my questions with the SWMF/BATS-R-US model.

Finally, I would like to express my gratitude for my close friends, my mother and my sister. And also I should not forget to thank the metal & pop-punk music playlists that have been playing in the background for hours and the blackest coffee I have been consuming during my studies.

July 2022 Pelin ERDEMİR

TABLE OF CONTENTS

Page

ABBREVIATIONS

ACE : Advanced Composition Explorer

AE : Auroral Electrojet index

AU : Auroral Electrojet upper envelope

AIA : Atmospheric Imaging Assembly

AL : Auroral Electrojet lower envelope

AMIE : Assimilative mapping of the ionospheric electrodynamics

BATS-R-US : Block-Adaptive Tree-Solarwind Roe-type Upwind Scheme

CCMC : Community Coordinated Modeling Center

CH : Coronal hole

CHIMERA : Coronal Hole Identification via Multi-thermal Emission Recognition Algorithm

CIR : Corotating interaction regions

CMD : Central meridian distance

CME : Coronal mass ejection

Dst : Disturbance storm time index

DMSP : Defense Meteorological Satellite Program

EIT : EUV Imaging Telescope

EUV : Extreme ultraviolet

FAC : Field aligned current

GGS : The Global Geospace Science

GM : Global magnetosphere

GPS : Global Positioning System

GSM : Geocentric solar magnetospheric coordinates

GNSS : Global Navigation Satellite System

HF : High frequency

HSS : High speed solar wind stream

ICME : Interplanetary coronal mass ejection

IE : Ionospheric electrodynamics

IM : Inner magnetosphere

IMF : Interplanetary magnetic field

Kp : Planetary K-index
LASCO : The Large Angle Spectrometric Coronagraph
LEO : Low Earth orbit
MC : Magnetic cloud
MFI : Magnetic Field Investigation
MHD : Magnetohydrodynamics
MLR : Multi linear regression
MO : Magnetic obstacle
PC : Geomagnetic Polar Cap Index
QL : Quick look
RCM : Rice Convection Model
RIM : Ridley Ionosphere Electrodynamics Model
SDO : Solar Dynamics Observatory
SECCHI : Sun Earth Connection Coronal and Heliospheric Investigation
SH : Sheath
SLR : Simple linear regression
SO : Storm onset
SOHO : Solar & Heliospheric Observatory
SSC : Storm sudden commencement
STEREO : Solar Terrestrial Relations Observatory
SuperDARN : The Super Dual Auroral Radar Network
SWE : Solar Wind Experiment
SWMF : Space Weather Modeling Framework
UT : Universal time

SYMBOLS

B, Bx, By, Bz : Magnetic field magnitude and x, y, z component**s**

β_p **:** Plasma beta

Cx **:** Complex

Dst* **:** Pressure corrected Dst index

E **:** Ejecta, Electric field

E_i **:** Original induction field

ε **:** Epsilon parameter

Fr **:** Flux-rope

Fr+ **:** Large rotation flux-rope

Fr- **:** Small rotation flux-rope

h **:** Ionospheric latitude

J **:** Height-integrated total ionospheric current

J_p **:** Net Pedersen current

JH **:** Joule heating

λ **:** Geomagnetic longitude

l_0 **:** Scale factor with the physical dimension of length

μ_0 **:** Vacuum permeability

n_p **:** Proton density

P_{dyn} **:** Dynamic pressure

Q_J **:** Joule heating density

R_E **:** Earth radius

R_S **:** Sun radius

r_{corr} **:** Correlation coefficient

S **:** Poynting flux

σ_p, σ_1 **:** Pedersen conductivity

σ_h, σ_2 **:** Hall conductivity

σ_c **:** Cowling conductivity

T **:** Temperature

θ **:** Polar angle of magnetic field line on the Y-Z plane

θ_c **:** Geomagnetic colatitude

U : Neutral wind

U_A : Auroral precipitation

U_J : Joule heating

U_R : Ring current injection

U_T : Total energy dissipation

V_{SW}, V_{TOT}, V : Solar wind speed

LIST OF TABLES

Page

LIST OF FIGURES

Page

A STATISTICAL ANALYSIS OF IONOSPHERIC JOULE HEATING DRIVEN BY INTERPLANETARY CORONAL MASS EJECTIONS AND HIGH SPEED STREAMS WITH USING SWMF/BATS-R-US MHD MODEL

SUMMARY

Space weather is the changes in the interplanetary space caused mainly by solar activity. Some of the space weather hazards are disruption of radio communication signals, disruption of electrical systems, increased satellite drag and increased radiation dosage on flights. Thus, the observations and predictions of these space weather events are significantly important with the developing space science and technology. Two major solar phenomena that affect the environment near Earth the most are classified as coronal mass ejections and high speed solar wind streams. Depending on the solar activity, the sunspot cycle, their occurrence rate changes. Due to their origin, occurrence, interplanetary structure and the geomagnetic disturbances they drive, they affect the space weather in different ways and intensities. Solar wind-magnetosphere-ionosphere coupling process is driven differently for each phenomena. The energy budget of the solar phenomena is dissipated into the magnetosphere-ionosphere system resulting in moderate to major geomagnetic disturbances, called geomagnetic storms. Geomagnetic storms are one of the highest contributions to this dissipation is via Joule heating, which is a frictional heating in the ionosphere caused by the electrical currents. Thus, in this study, the main aim is to reveal the differences of this two major phenomena (CMEs and HSSs) in the interplanetary space, then to investigate their driven geomagnetic storms in detail with their phases and finally to compare the Joule dissipation contributions (1) for their structural regions and (2) for the driven geomagnetic storm phases. Hereby, the differences of the coronal mass ejections and high speed solar wind streams would be tracked from their origin in the Sun, to the interplanetary space until they interact with the Earth's magnetosphere-ionosphere system. In the literature it is shown that the two phenomena have different structures and different driven geomagnetic storms.

CMEs in the interplanetary space are named as interplanetary coronal mass ejections (ICMEs) that consist of sheath (SH) and magnetic obstacle (MO) regions. The sheath region is followed just after the shock, thut it is a turbulent region with high temperature and speeds. On the other hand, a magnetic obstacle is the highly magnetized part of the ICME, which is generally referred to magnetic cloud with flux-rope pattern. The coronal hole high speed streams in the interplanetary space are named as corotating interaction region high speed streams (CIR/HSS) due to their continuous pattern with the Sun's rotation and longer presence. CIR/HSSs do not have a fast forward shock, thus the parameters do not have an abrupt increase but the density and magnetic field parameters increase before the others due to the compression of the fast and solar wind interaction region. Due to these differences it is thought that both phenomena have different Joule dissipation rate.

ICME driven storms are generally moderate to extreme in intensity, whereas the CIR/HSS driven storms are minor to moderate in intensity. Both phenomena have initial, main and recovery phases of their geomagnetic storms. But in the case of

ICMEs, the initial phase starts with a storm sudden commencement (SSC) differently from CIR/HSSs due to the fast forward shock. Also the main phase in the ICME driven storms are more intense. The recovery phase in both phenomena can last longer, but in CIR/HSS cases the full recovery is not that clear. Thus, the disturbances can last longer. Overall, it is expected that each phase has a different contribution in Joule heating of the ionosphere.

Joule dissipation is known as the heating of the upper atmosphere due to the ionospheric currents and friction of the ion-neutral collisions. It is not a directly observable parameter. And since it is a derived parameter, there are several techniques developed to estimate the heating rate. These methods include using ground based methods together with space-borne measurements and MHD models. Recently, the most preferred approach is to use physics-based models for the estimation of Joule heating. SWMF/BATS-R-US with RCM is one of the latest models developed by CCMC in order to obtain ionospheric electrodynamics parameters by solving MHD equations and then to estimate ionospheric dissipation. Thus, we decided to run the SWMF/BATS-R-US model to estimate Joule heating.

Firstly in this study, as solar phenomena, three CME and three HSS cases were selected to investigate. Then, the CME events were selected by using the SOHO/LASCO C2 coronagraph and HSS events were observed from the SDO/AIA telescope images. After the remote sensing observations, WIND spacecraft in L1 point was used to obtain in-situ data measurements. The event intervals are corrected by using ICME and CIR/HSS catalogs. Secondly, the SWMF/BATS-R-US magnetospheric MHD model was run in order to obtain Joule dissipation data covering the event intervals. After obtaining the model outputs, the structural intervals of CMEs and HSSs were determined and the corresponding Joule heating rates per unit time were determined. After, the ICME-driven and CIR/HSS-driven geomagnetic storm phase intervals were determined and the Joule heating rates corresponding to these phases were determined for each. To make a detailed comparison, simple linear regression and multi linear regression analyses were performed for the structural intervals. To compare the structural correlations in order to find out the controlling parameters, energy efficiency analysis was also performed for the geomagnetic storm intervals referring to the magnetospheric processes.

By the help of these analyses, it was found that the CMEs lead to the higher rates of Joule dissipation in the upper atmosphere rather than HSSs, mostly due to their magnetic obstacle regions. Also the geomagnetic storm interval resulted in more Joule heating for the CME cases. Main phases of the driven storms from both phenomena were found to relate with the highest Joule heating rate per unit time. With the SLR and MLR analyses, it was found for HSS that their controlling parameters are the geomagnetic activity parameters, whereas the controlling parameters of the CMEs are the solar wind parameters. This result revealed that the Joule heating driven by the HSSs are more effective and produced by the magnetospheric processes, whereas the Joule heating driven by CMEs are less effective and produced by the solar wind energy budget of the phenomena.

In Chapter 1, the aim of this study and literature work is introduced. In Chapter 2, solar activity and space weather are defined. Then CME and HSS phenomena are investigated in detail, followed by a description of geomagnetic storms and their phases and energy exchange processes. Chapter 3 explains the Joule heating, existing methods for estimations and the SWMF/BATS-R-US model. Chapter 4 consists of the selection of CME and HSS cases, run details of the MHD model, structural analysis of CMEs and HSS, geomagnetic storm analysis of ICMEs and CIR/HSSs, simple and

multi linear regression analyses for all cases and finally the energy efficiency analysis. In Chapter 5, the results are explained and the summary is given with future work recommendations.

SWMF/BATS-R-US MHD MODELİ KULLANILARAK GEZEGENLERARASI KORONAL KÜTLE ATIMLARI VE YÜKSEK HIZLI AKIŞLAR TARAFINDAN GELİŞEN İYONOSFERİK JOULE ISINMASININ İSTATİSTİKSEL ANALİZİ

ÖZET

Uzay havası, güneş aktivitesinin neden olduğu gezegenler arası boşluktaki değişikliklerdir. Uzay havası etkilerinden bazıları, radyo iletişim sinyallerinin bozulması, elektrik sistemlerinin bozulması, artan uydu sürüklenmesi ve uçuşlarda artan radyasyon dozajıdır. Dolayısıyla gelişen uzay bilimi ve teknolojisi ile bu uzay hava olaylarının gözlemleri ve tahminlerinin yapılması oldukça önemlidir. Dünya'yı ve yakın uzay ortamını en çok etkileyen iki büyük güneş aktivitesi olayı, taçküre kütle atımları ve yüksek hızlı güneş rüzgarı akımları olarak sınıflandırılır. Bu olayların Güneş aktivitesine, Güneş lekesi döngüsüne, bağlı olarak görülme sıklıkları değişir. Kökenleri, oluşumları, gezegenler arası yapıları ve sebep oldukları jeomanyetik bozunumlar nedeniyle uzay havasını farklı şekillerde ve şiddetlerde etkilerler. Güneş rüzgarı-manyetosfer-iyonosfer süreçleri, her olay için farklı şekilde gerçekleşir. Güneş olaylarının enerji bütçesi, jeomanyetik fırtınalar olarak adlandırılan orta ila büyük derecede jeomanyetik bozunumlara sebep olarak manyetosfer-iyonosfer sistemine dağılır. Bu dağılmaya en büyük katkılardan biri, elektrik akımlarının iyonosferde neden olduğu sürtünmeli bir ısınma olan Joule ısıtması tarafından gerçekleşir. Bu nedenle, bu çalışmada temel amaç, gezegenler arası uzayda bu iki ana olayın (TKA'lar ve YHGRA'lar) farklılıklarını ortaya çıkarmak, daha sonra sebep oldukları jeomanyetik fırtınalarını fazları ile ayrıntılı olarak araştırmak ve son olarak Joule ısınması katkılarını (1) yapısal bölgeleri ve (2) sürülen jeomanyetik fırtına fazları için karşılaştırmaktır. Böylece, taçküre kütle atımları ve yüksek hızlı güneş rüzgar akışlarının farklılıkları, Güneş'teki kökenlerinden, gezegenler arası uzaya kadar, oradan da Dünya'nın manyetosfer-iyonosfer sistemi ile etkileşime girmesine kadar izlenecektir. Literatürde, iki Güneş aktivitesi olayının da farklı yapılarda olduğu ve farklı jeomanyetik fırtınalara sebep olduğu gösterilmiştir.

Gezegenler arası uzaydaki TKA'lar, sheath (SH) ve magnetic obstacle (MO) bölgelerinden oluşan gezegenler arası taçküre kütle atımı (GATKA'lar) olarak adlandırılır. Sheath bölgesi şoktan hemen sonra gelir, ancak yüksek sıcaklık ve hızlara sahip türbülanslı bir bölgedir. Öte yandan, magnetic obstacle, genel olarak flux-rope yapısında olup magnetic cloud olarak adlandırılan GATKA'nın yüksek oranda manyetize olmuş kısmıdır. Gezegenler arası uzaydaki koronal delik kaynaklı yüksek hızlı akışlar, Güneş'in dönüşü ve uzun süre mevcudiyeti ile sürekli yapısından dolayı birlikte-dönen etkileşim bölgesi yüksek hızlı akışları (BDEB/YHA) olarak adlandırılır. BDEB/YHA'ların önünde şok yoktur, bu nedenle Güneş rüzgarı parametrelerinde ani bir artış olmaz, ancak hızlı ve güneş rüzgarı etkileşim bölgesinin sıkıştırılması nedeniyle yoğunluk ve manyetik alan parametreleri diğerlerinden önce artar. Bu farklılıklar nedeniyle her iki Güneş aktivitesinin de farklı Joule ısınması oranlarına sahip olduğu düşünülmektedir.

GATKA kaynaklı jeomanyetik fırtınalar genellikle orta ila aşırı şiddetteyken, BDEB/YHA güdümlü fırtınalar hafif ile orta şiddetlidirler. Her iki olayın da sebep olduğu jeomanyetik fırtınaların başlangıç, ana ve iyileşme evreleri vardır. Ancak GATKA'lar söz konusu olduğunda, hızlı ileri şok nedeniyle BDEB/YHA'larden farklı olarak ilk aşaması bir fırtına ani başlangıcı (FAB) ile başlar. Ayrıca GATKA kaynaklı fırtınalardaki ana evre daha şiddetlidir. Her iki Güneş aktivitesi olayında da iyileşme aşaması daha uzun sürebilir, ancak BDEB/YHA vakalarında tam iyileşme o kadar net değildir, belirsizdir. Bu sebeple jeomanyetik bozunumlar daha uzun sürebilir. Genel olarak, iyonosferin Joule ısınmasında her fazın farklı bir katkısı olması beklenir.

Joule ısınması, iyonosferik akımlar ve iyon-nötr çarpışmalarının gerçekleştirdiği sürtünme nedeniyle üst atmosferin ısınması olarak bilinir. Doğrudan gözlemlenebilir bir parametre değildir. Türetilmiş bir parametre olduğu için, ısıtma oranını tahmin etmek için geliştirilmiş birkaç teknik vardır. Bu yöntemler, uzay kaynaklı ölçümler ve MHD modelleri ile birlikte yer tabanlı yöntemlerin kullanılmasını içerir. Son zamanlarda en çok tercih edilen yaklaşım Joule ısınmasının tahmini için fizik tabanlı modellerin kullanılmasıdır. RCM ile çalışan SWMF/BATS-R-US modeli, MHD denklemlerini çözerek iyonosferik elektrodinamik parametreleri elde etmek ve ardından iyonosferik Joule ısınması değerini elde etmek için CCMC tarafından geliştirilen en son ve en yeni modellerden biridir. Bu nedenle, Joule ısınmasını elde etmek için bu çalışmada SWMF/BATS-R-US modeli kullanılmıştır. Bu çalışmada ilk olarak üç TKA vakası ve üç YHA vakası detaylı araştırmak ve istatistiksel analiz yürütmek için seçilmiştir. Daha sonra SOHO/LASCO C2 koronagraf ve AIA teleskop görüntülerinden TKA ve YHA olayları gözlemlenmiştir. Gözlemlerden sonra, veri ölçümleri için L1 Lagrange noktasındaki Güneş rüzgarı, WIND uydusu aracılığıyla alınmıştır. Olay aralıkları GATKA ve BDEB/YHA katalogları ile belirlenmiştir. İkinci olarak, olay aralıklarına tekabül eden Joule ısınması verisini elde etmek için SWMF/BATS-R-US manyetosferik MHD modeli çalıştırılmıştır. Model çıktıları elde edildikten sonra TKA'ların ve YHA'ların yapısal aralıkları belirlenmiş ve birim zaman başına karşılık gelen Joule ısınması değerleri belirlenmiştir. Daha sonra, GATKA ve BDEB/YHA sebebiyle gelişen jeomanyetik fırtınanın faz aralıkları belirlenmiştir ve bu fazlara denk gelen Joule ısınması oranları hesaplanmıştır. Karşılaştırmaları daha detaylı yapabilmek için basit doğrusal regresyon ve çoklu doğrusal regresyon analizleri uygulanmıştır. Bu iki Güneş aktivitesi olayının sebep olduğu Joule ısınmasını kontrol eden parametreleri bulmak için yapısal korelasyonları karşılaştırmanın dışında, manyetosferik süreçleri temsil eden jeomanyetik fırtına aralıkları için enerji verimliliği analizi de yapılmıştır.

Bu analizler sonucunda, TKA'ların, çoğunlukla magnetic obstacle bölgeleri nedeniyle, YHA'lardan ziyade üst atmosferde daha yüksek Joule ısınması oranlarına yol açtığı bulunmuştur. Ayrıca jeomanyetik fırtına aralığı baz alındığında, TKA olaylarında daha fazla Joule ısınması oranı elde edilmiştir. Her iki olaydan da kaynaklanan fırtınaların ana fazlarının, birim zaman başına en yüksek Joule ısınma oranı ile ilişkili olduğu bulundu. Regresyon analizleri ile YHA için Joule ısınmasını kontrol eden parametrelerin jeomanyetik aktivite parametreleri olduğu, TKA için Joule ısınmasını kontrol eden parametrelerin ise güneş rüzgar parametreleri olduğu bulunmuştur. Bu sonuç, YHA'lar sebebiyle ortaya çıkan Joule ısınmasının daha etkili olduğunu ve manyetosferik süreçler tarafından üretildiğini, TKA'lar sebebiyle ortaya çıkan Joule ısınmasının ise daha az etkili olduğunu ve güneş rüzgar enerji bütçesi tarafından üretildiğini ortaya koymuştur.

Bölüm 1'de bu çalışmanın amacı ve literatürdeki çalışmalar tanıtılmaktadır. Bölüm 2'de Güneş aktivitesi ve uzay havası detaylı bir şekilde açıklanmıştır. Daha sonra TKA ve YHA olayları, kökenleri, yapıları ve farklılıkları incelenmiştir. Sonrasında ise jeomanyetik fırtınalar tanımlanmış ve fazları açıklanmıştır. Bu bölümün son kısmında ise güneş rüzgarı-manyetosfer-iyonosfer sistemindeki enerji süreçleri açıklanmıştır. Bölüm 3, Joule ısınmasının detaylı açıklamasını, mevcut veri elde etme yöntemlerini ve manyetosferik SWMF/BATS-R-US MHD modelini açıklamaktadır. Bölüm 4, TKA ve THA olaylarının seçilmesini, MHD modelinin kullanım ayrıntıları, TKA ve YHA'ların yapısal analizlerini, TKA ve YHA'ların sebep olduğu jeomanyetik fırtınaların ve fazlarının incelemesini, basit ve çoklu doğrusal regresyon analizlerini ve son olarak enerji verimliliği analizini oluşturur. Bölüm 5'te, Böüm 4'te gerçekleştirilen analizler ile elde edilen çarpıcı ve önemli sonuçlar açıklanmış, gelecek çalışma önerileriyle birlikte özet şeklinde verilmiştir.

1. INTRODUCTION

Space weather has been increasing its importance with each passing day due to its threatening effects on human life on Earth and spacecraft missions in the interplanetary medium. Space weather is a term related to the activities of the Sun and its consequences for the solar system, mostly on our planet Earth and its protective and surrounding magnetosphere. A magnetosphere is considered as the surrounding dominant magnetic field region of a planet. And Earth's magnetosphere is protecting us, the life on our planet, by acting as a shield and deflecting most of the incoming highly energetic and hazardous particles by means of its strong magnetic fields. Solar activity is the general term for the activities developing on the Sun's surface caused by its gaseous structure resulting with changes in magnetic fields. The temporary dark and cold visible areas on the Sun's surface with 11-years of cycle including a solar minimum and a solar maximum, which are called sunspots, are the main indicator of magnetic disturbances causing solar activity such as solar flares, coronal mass ejections (CME), solar prominences, filaments, loops, coronal holes (CH) and high speed streams (HSS). During the ascending phase of the solar activity, it is more common to observe coronal mass ejections, the giant magnetized plasma bubbles belched out from the solar corona, due to the enhanced disturbance with increased number of sunspots and active regions on the Sun's surface. On the other hand, the descending phase of the solar activity is more likely to produce coronal hole high speed solar wind streams, where the dark areas on the solar surface allow solar wind particles to escape with very high speeds from the open magnetic field lines to interplanetary space. Since the solar activities can result with the interaction of the Earth's magnetosphere and the energetic particles and photons, it can give rise to geomagnetic storms on Earth. Magnetic disturbances caused by the long duration of the southward component of the interplanetary magnetic field that result in reconnection with magnetic field lines of Earth and lead to exchange of a great amount of energy is known as geomagnetic storms. Some of the hazards caused by geomagnetic storms are disruption of power systems and navigation systems, HF radio communication

blackouts, satellite damages and increased radiation for airline passengers. The exchange of energy during geomagnetic storms is also inducing electrical currents resulting in Joule heating in the upper atmosphere, which interacts with the thermosphere and leads to some hazardous consequences. One of the most important consequences is stronger atmospheric drag force in a short-time due to the increased temperature and density of the expanded atmosphere during geomagnetic storms, which can even lead to the loss of low Earth orbit (LEO) satellites. A recent example was during the first week of February 2022 when the solar activity was in the ascending phase of 25th cycle, the moderate geomagnetic storm driven by coronal mass ejections caused ionospheric Joule heating and resulted with a decrease in the altitude, thus led to the fall of about 40 Starlink satellites of SpaceX company. The statistical relationship between different solar phenomena and resulting Joule heating is yet unknown. In this study, we aim to explain the most common and powerful two space weather phenomena structures and their corresponding geomagnetic storms with their resulting Joule heating rates. And we try to build empirical relations between Joule heating and controlling solar wind parameters to be able to develop a simple prediction model for Joule heating on Earth's ionosphere. In many ways, building such a connection between solar wind parameters measured in the interplanetary medium and resulting Joule heating after magnetospheric energy exchange processes, geomagnetic storms, could put out improved forecasts and even early warning systems for unexpected hazardous effects in the Earth's ionosphere.

1.1 Purpose of Thesis

Since the 18th century, solar activity observations have been one of the most interesting topics in astronomy and since then they are being improved substantially with advancement in space technology. With the increasing numbers of space missions and the developments in technology, the importance of solar activity related topics such as space weather phenomena and forecasting have become the focus of researchers and raised its awareness among society. In our century, space weather hazards are also considered as a hazard, which is affecting human life on Earth. If the precautions of the space weather events are not taken and it is not forecasted accurately, it is posing a great risk for the spacecrafts in the interplanetary medium, exploration missions in space, flight passengers, electrical systems on Earth, navigation technologies,

pipelines, HF radio communication and so on. Two of the most effective examples for the space weather phenomena can be given as coronal mass ejections due to the mass and magnetic field strength it has and high speed solar wind streams due to their long durations. The origin and structure of the coronal mass ejections and high speed streams differ from each other, thus it is believed that their consequences after the interaction of Earth's magnetosphere is observed in a different way. Both of the events cause minor to extreme geomagnetic disturbances on Earth. And these disturbances with significant energy exchange rates called geomagnetic storms can result with changes in the Earth's ionospheric parameters due to the Joule heating. Thus, the main point of this research is evolved as observing the space weather phenomena on the Sun, then measuring its quantities within the L1 point (between the Earth and the Sun) and tracking it until it interacts with the Earth's magnetosphere and leads to the geomagnetic disturbances causing Joule heating in the upper atmosphere. In this way, the energy input from the phenomena to the ionosphere resulting with Joule heating is investigated in three main categories: the type of the phenomena, structure of the phenomena, the geomagnetic storm resulting from the energy input of the phenomena. The statistical analyses performed with observations, measurements and modeling results is going to provide an insight to the solar wind and geomagnetic activity parameters that are controlling the ionospheric Joule heating. With the observed correlations, empirical relations are expected to link the space weather phenomena to Joule heating. In the view of such information, the controlling parameters of Joule heating during different phenomena will be cleared up and it will lead future researches about the prediction of Joule heating.

1.2 Literature Review

Space weather has recently been one of the topics that has increased the awareness in the science world. The space weather term itself is defined as the environmental condition of the space taking the Sun and interplanetary medium into consideration (WMO, n.d.). Whilst, its main concern is stated as the events in space including charged particles with high energy, magnetic field, electromagnetic radiation and plasma properties that can have hazardous effects on expensive technological device systems including spacecrafts, communication or power systems (ESA, n.d.). A part of the energy coming from solar wind, which is defined as the non-stop flow of plasma

from the Sun, interacts with the Earth's magnetosphere and leads to the geomagnetic storms, substorms and aurora by causing disturbances in the geomagnetic activity (Rathore et. al., 2014). When the energy exchange efficiency is high between the solar wind and the near Earth environment, it results with a great geomagnetic disturbance called a geomagnetic storm (NOAA, n.d.). The driver mechanism of geomagnetic storms has also been another important research topic for space weather. One of the main drivers of geomagnetic storms is the strong interplanetary magnetic fields toward the south during long intervals that result with reconnection of the solar wind with Earth's magnetosphere leading to energy exchange in the magnetotail (Tsurutani & Gonzalez, 1997). Another driver is solar wind velocity with its importance in tail electric field, which is not considered as a major factor due to its small variability compared with magnetic field (Tsurutani & Gonzalez, 1997). Badruddin (2002) proposed that if the relationship between the solar wind plasma and magnetic field parameters, that driving the storm, is understood well, the prediction of geomagnetic storm can be done simply and solar wind-magnetosphere coupling can be explained in all ways. Plenty of articles are published suggesting that the coronal mass ejections and high speed solar wind streams are the drivers of geomagnetic storms. Verbanac et. al. (2013) suggest that energy transfer with magnetic reconnection is mostly dependent on strong southward interplanetary magnetic field, where the interplanetary coronal mass ejections and coronal hole high speed streams are the two large-scale solar drivers that correspond to the existence of it. Geomagnetic storms on Earth can be mostly resulted by interplanetary shocks, coronal mass ejections and high speed streams (Lu, 2006). Two of the large-scale examples as space weather phenomena are coronal mass ejections and high speed streams (Gopalswamy, 2008). Coronal mass ejections (CMEs) traveling the distance from the sun with speeds over 500 km/s and strong magnetic fields into the space environment are classified as solar phenomena (Tsurutani & Gonzalez, 1997). Fast streams with the continuous flow of plasma are defined as high speed solar wind streams (HSSs) (Gerontidou et. al., 2018). In the literature, there are some works explaining the differences of coronal mass ejections and high speed solar streams. One of the apparent differences is that high-speed streams present a continuous flow from the Sun, while the coronal mass ejections form an instantaneous disruption of the steadiness, where the background solar wind conditions result with large fluctuations (Temmer et. al., 2017). About near solar maximum, the strong geomagnetic storms with Dst < -100 nT are driven by the

interplanetary coronal mass ejections, while coronal hole high speed streams are the drivers of the activity in the interplanetary space around solar minimum (Gonzalez et. al., 1999). In order to make easier comparisons between two large-scale phenomena because of their differences, "geoeffectiveness" term has been another topic of interest. Geoeffectiveness is defined as the capability of large scale interplanetary structures with strong magnetic fields driving geomagnetic storms where geomagnetic activity indices Ap, Kp, AE, and Dst are used to measure it (Gopalswamy, 2008). Dynamic pressure increase as a parameter of solar wind, positive Dst and AE index increase associated with the shocks induce a sudden enhancement in the ionospheric electric potentials, Joule heating, auroral precipitation (Lu, 2006). Solar wind electromagnetic power ratio to magnetospheric energy dissipation, as an indicator of geoeffectiveness, for high speed streams is found as 1.80, while it is found as 0.80 for ICME events with magnetic clouds (Lu, 2006). The energy transfer within the magnetosphere and ionosphere has been another important topic, since each solar phenomena results with different mechanisms and geoeffectiveness of dissipation. Akasofu (1981) suggests that the auroral particle energy flux, Joule heating production rate and ring current injection rate are the most important processes in the dissipation of energy, while the sum of three is referred as the total energy consumption rate of the magnetosphere. Energy stored in the Earth's magnetosphere after the arrival of high energy particles from solar activity is dissipated by degrees in time (Robinson & Zanetti, 2021). Loss of energy from magnetosphere to ionosphere is possible with particle precipitation and also with Joule heating, which is the heating of the atmosphere caused by frictions related with ionospheric currents (Robinson & Zanetti, 2021). Østgaard et al. (2002) put out that during a substorm, the total energy dissipation is a sink of auroral flux, Joule heating and ring current respectively 15%, 56%, and 29%. On the other hand, in another study, Salice (2020) showed that the total energy dissipation in all storms is respectively the same amounts around 19.6%, 62.6% and 17.8% where Joule heating rate plays an important role as the major energy sink of the magnetosphere. In the light of this information, Joule heating as the main sink of total energy dissipation is decided to be investigated as a continuation of the literature research. Cole (1961) explained the Joule heating term for the first time as the increase of upper atmospheric heating caused by the electrical currents that is resulted by geomagnetic disturbances. The collision of ionospheric ions results with open magnetic field lines of Earth undergo a friction and lose energy because of Joule heating (Salice, 2020). Akasofu (1981)

suggested that Joule heating rate in the ionosphere is proportional to the AE index. After two years Ahn et. al. (1983) estimated a global Joule heating production rate (U_J) with a linear relationship to AE index, U_J= 2.3 x 10^8 AE. Later, Østgaard et. al. (2002) derived another equation using AE, but as a whole of north and south hemispheres, U_J [GW] = 54 AE + 1.8. The dominant factor of Joule heating is stated as ion-neutral collisions and this information is used in order to obtain total Joule heating rate in terms of current density, neutral wind velocity, electric field, magnetic field, Pedersen and parallel conductivities (Richmond, 2021). Aikio & Selkälä (2009) also derived another equation called "height-integrated Joule heating", with variables of current density, Pedersen conductivity and electric field. For accurate Joule heating estimation, real time measurements of electric field, Pedersen conductivity and neutral winds in E-region must be done (Aikio & Selkälä, 2009). In some studies, the AMIE method is also used to obtain the required parameters for Joule heating estimations. Assimilative mapping of the ionospheric electrodynamics (AMIE) method that is developed to obtain parameters such as ionospheric electric fields, currents and corresponding magnetic variations from observations of radars, satellites and ground measurements (Richmond & Kamide, 1988). Poynting flux inflowing into the ionosphere measured from satellites is one of the other methods to calculate Joule heating (Aikio & Selkälä, 2009). Electromagnetic energy exchange within the magnetosphere-ionosphere system is measured by the Poynting flux (Rastaetter et. al., 2016). Olsson et. al. (2004) suggested a method as downward Poynting Flux equation that is derived into a form consisting of electric and magnetic field variables taken from satellite measurements to estimate Joule heating in GW. Li et. al. (2011) showed that enhanced Joule heating estimated Open Geospace General Circulation Model (OpenGGCM) is coherently related with strong downward Poynting flux. To compare the electric field and magnetic field from model predictions to estimate Joule heating, Weimer (2005) used the measurements from DMSP. In the literature, Global magnetohydrodynamic simulation Grand Unified Magnetosphere Ionosphere Coupling Simulation (GUMICS-4) is also another method used for Joule heating estimation (Palmroth, 2005). Electrodynamics solvers coupled to magnetosphere MHD models is another approach stated by Rastaetter et. al. (2016), that is estimating Joule heating by the ionospheric Pedersen conductance and electric field. As a magnetospheric MHD model, Block-Adaptive Tree-Solarwind Roe-type Upwind

Scheme (BATS-R-US) coupled with the Rice Convection Model (RCM) and Ridley Ionosphere Electrodynamics Model (RIM) is one of the models in Space Weather Modeling Framework (SWMF) to estimate Joule heating with high resolution simulations (Gombosi et. al., 2021). It is shown that there are many ways to calculate Joule heating, empirically, simulative or with coupled models. Some comparisons of energy efficiency of different solar phenomena and their corresponding storms is performed by Turner et al. (2009), where the Dst value peaks had apparent differences, but the difference of Joule heating calculated from PC and Dst indices between the two events (CMEs and CIRs) was not statistically separable. With the literature search performed, there is no current works comparing high resolution estimated model Joule heating, as the highest determined ratio for total energy dissipation in the literature, resulted with the energy dissipation after the interaction of two large scale solar phenomena (CMEs and HSSs) with the Earth's magnetosphere and with their structural properties, driven storms and phases.

1.3 Hypothesis

After the interaction of solar phenomena with the magnetosphere, there is an energy exchange process causing disturbances on Earth. While the energy input is dissipated into the magnetosphere-ionosphere system in many forms such as auroral precipitation, ring current and Joule heating, it has proven that Joule heating has the highest partitioning rate amongst others, thus having a great importance. Upper atmospheric Joule heating as a consequence of geomagnetic disturbances driven by different solar phenomena such as coronal mass ejections and high speed solar wind streams can cause different rates of heating mainly depending on the type and structure of the phenomena and also depending on their driven geomagnetic storm phases. The giant plasma bubbles, CMEs, with very high speed and strong magnetic fields are expected to cause a higher Joule heating per unit time referring to that event interval, whilst the coronal hole high speed streams are expected to put relatively lower amounts of unit time heating. Due to the short-duration of CMEs, it is estimated to result with less total heating, when in the meantime HSSs with well known characteristics such as long durations are expected to put out much more total Joule heating within the time interval corresponding to the event duration. Geomagnetic storms driven by ICMEs also are expected to be more powerful, thus the heating in the ionosphere, when it is

compared to the ones driven by CH HSSs. When the development of a geomagnetic storm is considered with its corresponding phases, it is expected to observe the highest Joule heating per unit time during the main phase for both types of phenomena. Another point of view is that the energy input into Earth's magnetosphere will differ by both phenomena, resulting with the controlling solar wind and geomagnetic activity parameters of the heating to be different. And since the solar wind speed and southward interplanetary magnetic field are the parameters that play an important role in the development of geomagnetic disturbances, these parameters are expected to show the highest correlations among the other parameters. In this we study, upper atmospheric Joule heating obtained from the SWMF/BATS-R-US with RCM magnetospheric MHD model output will be statistically analyzed in the light of the structural differences of coronal mass ejections and high speed streams and their corresponding driven geomagnetic storms and their phases as a case study.

2. SOLAR ACTIVITY AND GEOMAGNETIC EFFECTS

2.1 Solar Activity and Space Weather Definitions

Space weather is one of the most important topics out there for space science.The changing state of our Sun in the interplanetary medium is defined as space weather. Our Sun has the continuous charged particle outflows named as solar wind, averagely with 400 km/s speeds. The activity on the Sun can cause the outflow of the energetic particles to increase. Events on the Sun and in interplanetary space cause space weather phenomena that affect the environment near Earth (WMO, 2021). Space weather impacts can be disruptions in electric power grids, HF radio communication, satellite communication, disruption in GPS/GNSS signals, increased satellite drag and even changes in climate (NOAA, n.d.). Since the main concern of the space weather science is the Sun and solar activity, it should be explained in more detail. Our Sun is a giant sphere consisting of charged electrical gasses on its surface, which leads to the strong magnetic forces called magnetic fields (NASA, n.d.). Solar activity is created by these moving gasses that start to tangle, stretch and twist the magnetic field ropes of the Sun (NASA, n.d.). With the rotation of the gasses with different speeds on the Sun's latitudes, the twisted magnetic field lines lead to the sunspot formation on the surface, which is the main indicator of solar activity. The dark regions spotted on the Sun's surface, that are as big as a planet's size are sunspots (UCAR, 2011). Space weather forecasting is done by monitoring the sunspots, since they are related with the solar activity and it can be used in the prediction of solar storms (UCAR, 2011). When the sunspot numbers is increasing, the solar activity is increasing as well. On the other hand the decreasing sunspot numbers refer to the lower solar activity. The solar activity is depending on the ascending and descending phases of the solar activity cycle consisting of total sunspot numbers. The Sun has patterns of sunspot numbers changing with time, called periodicities. The 11-years periodicity of the sunspot cycle and the Sun's 27-day rotation is important for solar activity as well as the periodicity of 22-years where the magnetic field of the Sun changes its polarity is playing an important role (Suess & Tsurutani, 2003). In Figure 2.1, the solar cycle is shown for

about the last 100 years where the latest cycle, 25th cycle, has started around 2020 and it is in the ascending phase.

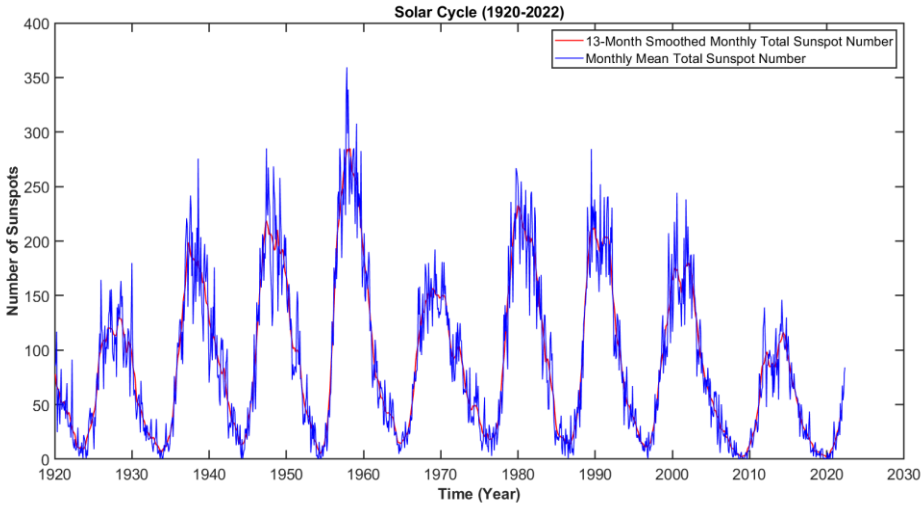

Figure 2.1 : Solar cycle showing the number of monthly total sunspots. (Data is obtained from WDC-SILSO, Royal Observatory of Belgium, Brussels).

The quiet sun with low solar activity have some features such as spicules, granules and coronal holes whereas the active sun forms sunspots, active regions, coronal loops, solar filaments and prominences, solar flares and coronal mass ejections as a space weather phenomena causing disturbances in the Earth's magnetosphere-ionosphere-thermosphere system, geomagnetic storms. Two of the large-scale solar phenomena causing geomagnetic activity are coronal mass ejections (CMEs) and high speed solar wind streams (HSSs). Since CMEs mostly occur near solar maximum, and most of the HSSs are observed during solar minimum, this study will be focused on both phenomena in the next sections for a comparison of solar phenomena and activity.

2.2 Coronal Mass Ejections (CMEs)

2.2.1 Definition and characteristics of coronal mass ejections

Coronal mass ejections, the giant plasma bubbles with magnetic fields thrown outwards from the Sun's corona, are one of the main solar phenomena that can cause geomagnetic activity on Earth. Coronal mass ejections are defined as the dramatic glimpses of solar activity in with the 1-10 million tons of thrown material from the Sun to the interplanetary medium (Gosling, 1993). Occurrence within the time interval of a few minutes to hours and the characteristics in the coronagraph as visibility of

particularly new, bright and white light are the two trackable changes in the structure of corona, which refers to the coronal mass ejections (Hundhausen et. al., 1984). They are highly energetic and they can have very high speeds compared to solar wind. Because of their speeds, they disturb the solar wind in a short time where their effect on Earth can be observed from a few hours to some days. Their speeds can be spread from under 10 km/s to over 2000 km/s (Burkepile & St. Cyr, 1993). With kinetic energies that can exceed $1x10^{16}$ Joules, coronal mass ejections are considered as the most energetic structures of the Sun (Hudson et. al., 2006). At 1 AU, magnetic field strength is 15-30 nT for the CMEs with magnetic cloud structure (Lepping et al. 1990). In Figure 2.2, one of the first coronagraph images from 14 April 1980 is showing the expansion of a coronal mass ejection through the Sun in the structure of a bubble.

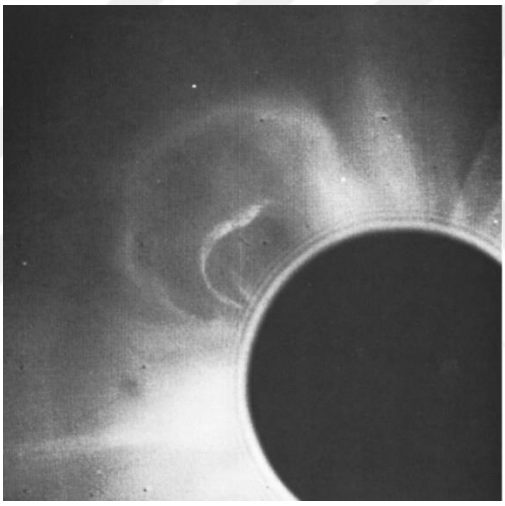

Figure 2.2: One of the first observed coronal mass ejection coronagraph image on April 14, 1980 by the SMM. (Hundhausen et.al., 1984).

They are generally formed in the closed magnetic field regions expanding from the Sun. Instabilities in the coronal magnetic field result with the propelling of the magnetic loops containing the closed magnetic fields of coronal streamers by the subjacent lifting force of the coronal cavities (Gosling, 1993). Active regions, filament and prominences are marked as the origination regions of the coronal mass ejections where the closed magnetic fields with large-structure exist (Gopalswamy, 2003).

2.2.2 Structure of coronal mass ejections

After the coronal material is thrown out to interplanetary space, its observed structure plays a great role for space weather. The interplanetary demonstrations of the coronal

mass ejections are called interplanetary coronal mass ejections (Gopalswamy, 2007). As long as the giant plasma structure travels through space, its regions with different properties can result with different outcomes on Earth. Thus, it is important to determine the structure and the properties of ICMEs. Coronal mass ejections in the interplanetary space (ICMEs) consist of three structural parts: a forward shock front, sheath region, magnetic cloud (Illing & Hundhausen 1985). The shock is the region where all parameters have an abrupt increase, then followed by a region of the increased and fluctuating parameters, called sheath, and the less dense and colder magnetic structure with enhanced magnetic field following the sheath (Figure 2.3).

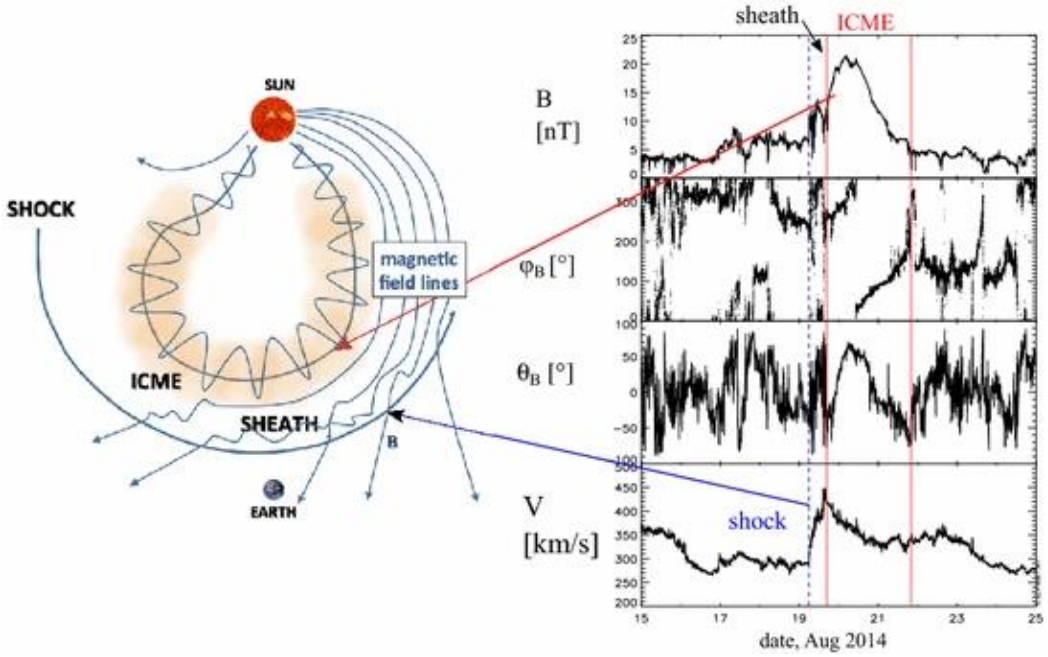

Figure 2.3: A structural schema of an interplanetary coronal mass ejection (ICME) with the forward shock, sheath and magnetic cloud region on the left and respectively measured solar wind quantities from ACE spacecraft corresponding to the ICME; the magnetic field magnitude, the longitude and latitude angles of the magnetic field and the solar wind speed (Kilpua et. al., 2017).

When the solar wind speed in 1 AU distance is exceeded by CMEs with speeds greater than 500 km/s, a shock wave disturbance is generally formed in the background solar wind (Gosling, 1993). But not all the coronal mass ejections develop a shock. After the shock, there is the turbulent sheath region. The density of the solar wind and the proton thermal speed increase in the sheath region (Gopalswamy, 2007). The sheath of the ICME has more variable magnetic field, more increased temperature and density than the magnetic cloud part has (Hosteaux et. al., 2019). The ICME shock and sheath are found to be followed by the magnetic cloud, where the change of rotating magnetic

fields almost parallel to the plane was determined steadily by the crossing of a magnetic loop (flux-rope) (Burlaga et. al., 1981). The coronal mass ejection bright front in the coronagraph images is relevant with the sheath region, where the dark cavity is associated with the magnetic cloud (Gopalswamy, 2007). Magnetic cloud region has a strong magnetic field in the shape of a large closed field and is relatively colder than the surrounding temperature, where the magnetic field lines rotate precisely (Hosteaux et. al., 2019). In this region, ICMEs show a flux rope structure within the magnetic cloud. Observations of a typical ICME with a magnetic cloud (MC) from Advanced Composition Explorer (ACE) spacecraft is shown Figure 2.4. The magnetic cloud region in Figure 2.4, clearly shows the features of strong magnetic field, decreased thermal speed, which refers to the lower temperature, and smooth rotation of the magnetic field that can be observable from the latitude and longitude parameters.

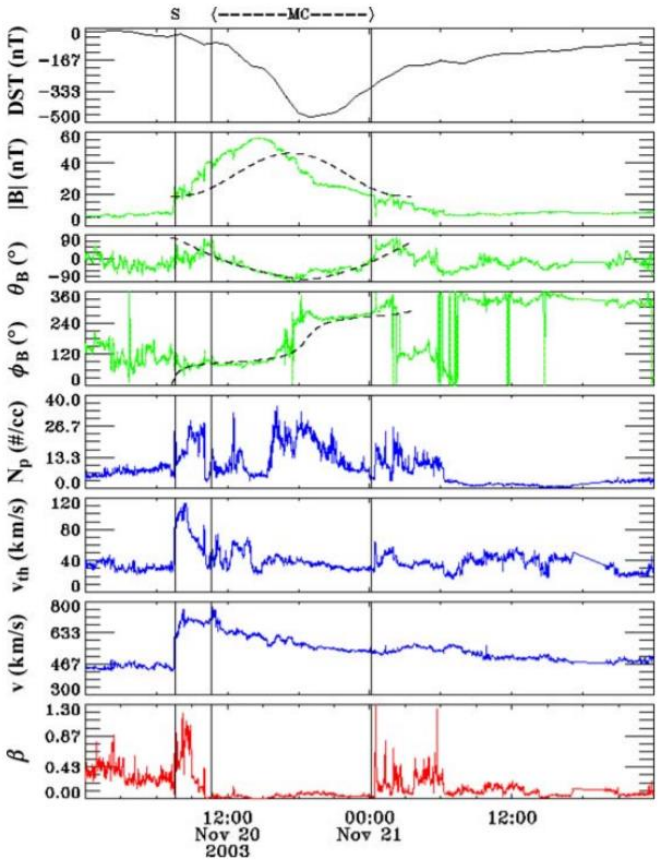

Figure 2.4: Observations from ACE spacecraft showing the passage of an ICME with shock, sheath and magnetic cloud. Parameters respectively show the Dst index, magnetic field strength, magnetic field latitude and longitude, proton density, thermal speed, solar wind speed and plasma beta where the vertical lines represent the shock and start/end times of the magnetic cloud. (Gopalswamy, 2005).

To determine the magnetic clouds (MC), some criteria is taken into account: plasma beta lower than 0.3, smooth change in magnetic field direction, increased magnetic field more than 8 hours, average magnetic field strength equal to or more than 8 nT, low proton thermal speed equal to or less than 30 km/s and difference in the latitude angle of magnetic field equal to or more than 45 degrees (Lepping et al., 2005). In Figure 2.5, the six different spacecraft passages through the coronal mass ejections with or without shocks are schematically shown (Gopalswamy, 2007).

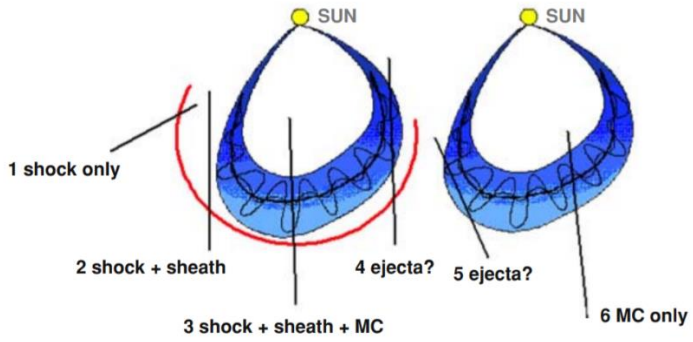

Figure 2.5: A schema showing different observation paths of a spacecraft passing through a coronal mass ejection with (left) and without fast forward shock (right). (Gopalswamy, 2007).

Thus, depending on the position of the spacecraft and its passage, the features of the CMEs cannot be sensed accurately sometimes and flux rope patterns cannot be detected. Some sources in the literature define the magnetic cloud part as a "magnetic obstacle" to separate the ICMEs with flux rope structures from others. As a less limiting expression, magnetic obstacle (MO) is used as an alternative to magnetic cloud (MC) to express the ICME structure with its magnetic configuration to include the changes of interplanetary evolution such as distortion or disruption of magnetic fields of coronal mass ejections, the magnetic structure embedded in an ICME (Nieves-Chinchilla et. al., 2018). This leads the terminology in this study to use magnetic obstacle (MO) rather than magnetic cloud (MC) for more accurate denotation. Depending on their rotation, there are 5 types of magnetic obstacles defined by their rotation criteria: single rotation flux-rope (Fr) between 90◦ – 180◦ , small rotation flux-rope (F-) lower than 90◦, large rotation flux-rope (F+) greater than 180◦, complex (Cx) with multiple rotations or ejecta (E) with unclear rotations (Nieves-Chinchilla et. al., 2019). In the light of all this information, the interplanetary coronal mass ejections showing a flux rope characteristic as a magnetic obstacle (MO)

are classified as ICMEs with magnetic clouds (MC). Whereas the complex or ejecta structures involved in the ICMEs are still named as magnetic obstacles (MO) but not magnetic clouds (MC). In this study, flux rope structures are the main focus of the magnetic obstacles. The study of Nieves-Chinchilla et al. (2019) put out that %43 of the investigated events showed a single rotation, where %16 of them showed small-rotation and about %18 of them showed large-rotation flux ropes that are suggested to be investigated in the further studies. It was said that large-rotation flux rope structures can be the indicators of remarkable curvature or distortion (Nieves-Chinchilla et al., 2018).

2.2.3 Measurements and observations of coronal mass ejections

Since the 1970s, coronagraphs have been the main instruments observing the eruptions from the Sun's corona. With the observation of Thomson scattered light, coronagraphs can track and monitor the coronal mass ejections (Webb & Howard, 2012). Their working mechanism is blocking the light from the solar disk to detect the changes, such as material releases, in the corona. The Large Angle Spectrometric COronagraph (LASCO) C2 and C3of SOHO mission and two white-light coronagraphs COR1 and COR2 of STEREO's SECCHI instrument are the most used coronagraphs. Lately, heliospheric imagers are also in use to detect the solar phenomena in different channels. H-alpha, X-ray and EUV images and coronagraphs provide a source for remote CME observations. Figure 2.6 shows the coronal mass ejection event occurred on 27 February 2000 through the SOHO/LASCO C2 and C3 coronagraphs.

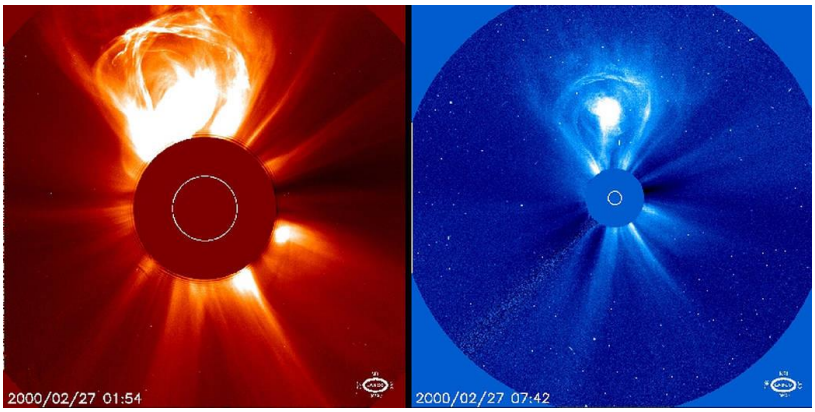

Figure 2.6: Coronagraph images from SOHO LASCO C2 (left) and C3 (right) obtained on 27 February 2000 during a coronal mass ejection (SOHO, 2000).

Nowadays, there are also CME catalogues (CACTus, HELCAT WP2, SOHO LASCO, DONKI M2M, etc.) that detect the solar phenomena automatically, in addition to the ones detected manually. With the detection of the coronal mass ejections (CMEs) through remote sensing observations, the structure of the ICMEs is determined with in-situ measurements from spacecrafts. In Figure 2.7, the average parameters through in-situ measurements of ICMEs with shocks are shown with corresponding structure.

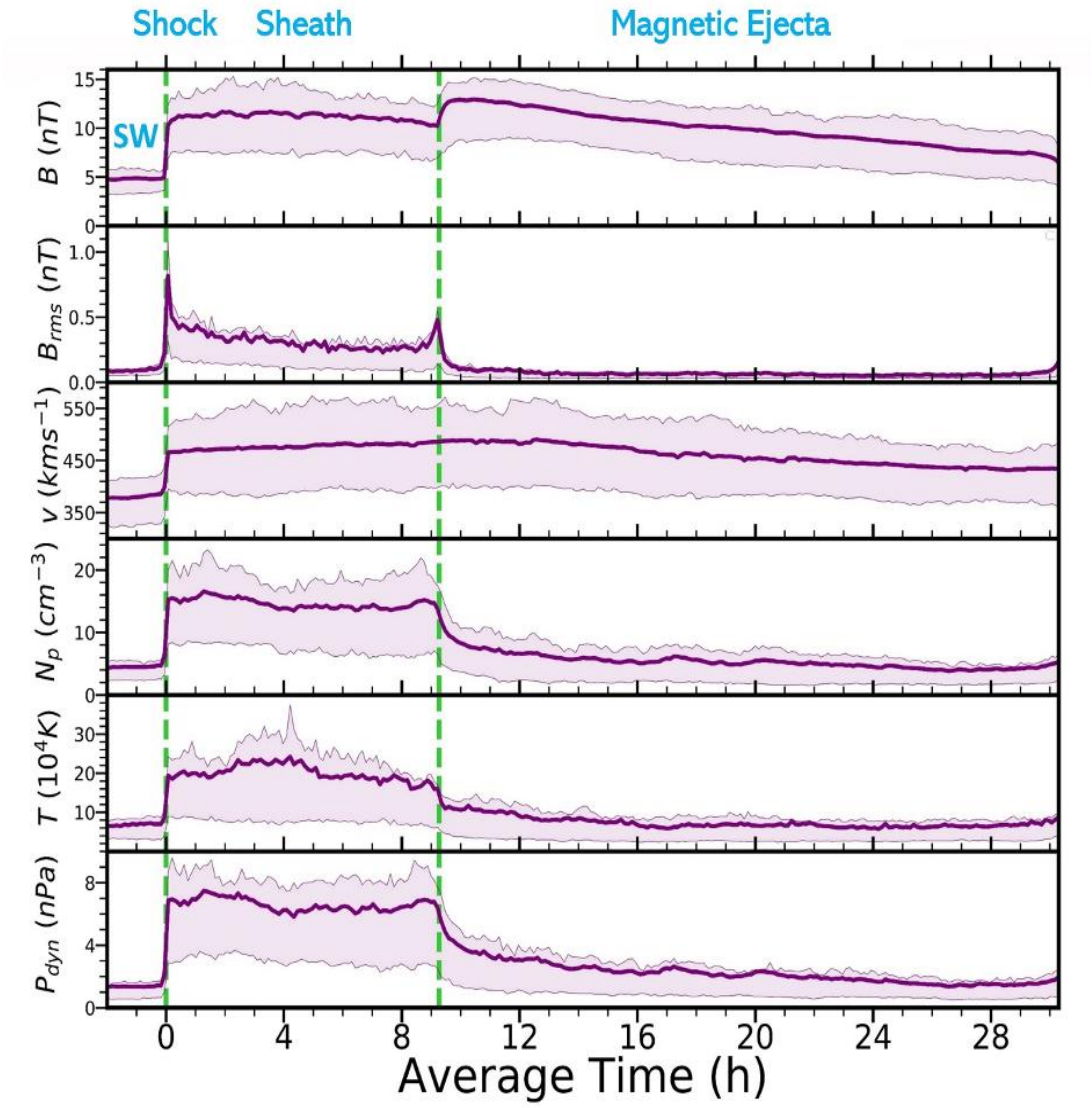

Figure 2.7: The typical marks of an ICME through in-situ measurements and superposed epoch analysis applied on multiple cases, where the shock is marked with a vertical dotted green line at t=0, followed by the sheath, and a magnetic obstacle starting with the second vertical green dotted line (The University of New Hampshire Coronal Mass Ejection Group, n.d.).

The measurements of ICMEs generally rely on the detection of changes and disturbances in the background solar wind plasma and magnetic field parameters

during the passage of the phenomena. One of the methods used is to track the phenomena from the spacecrafts at L1 - Lagrangian point between the Sun and the Earth, a few hours prior to the arrival of the particles to Earth. Solar and Heliospheric Observatory (SOHO), The Global Geospace Science (GGS) Wind and Advanced Composition Explorer (ACE) are positioned in L1 point for solar missions. Recently, Parker Solar Probe and Solar Orbiter missions were launched to observe the Sun closer than other missions.

2.2.4 Effects of coronal mass ejections on space weather and Earth

Consequences of the ICMEs on Earth can be different compared to other solar events. Earth-based electrical systems are affected mostly by geomagnetic storms caused by coronal mass ejections (Borovsky & Denton, 2006). Interplanetary coronal mass ejections are the major solar phenomena that can drive geomagnetic storms on Earth. The changes in the corona eventuate in a short time within a few minutes or hours, whereas the disturbances on Earth arise in three to four days resulting from coronal mass ejections (Hundhausen et. al., 1994). The faster coronal mass ejections directed to Earth can arrive around 15 to 18 hours, whereas slow ones can arrive in a few days (NOAA, n.d.). The warnings up to the 1 hour prior to the arrival of the ICME forward shock and sudden storm commencements are provided by L1 orbit spacecrafts as it is mentioned in previous sections. Velocity, magnetic field properties and mass, with less contribution, are the determining properties of coronal mass ejections for the strength of their driven geomagnetic storm (Hosteaux et. al., 2019). ICMEs drive geomagnetic storms on Earth depending on their southward magnetic fields, if they originated near the Sun's disk center as halo CMEs (Gopalswamy, 2007). During the solar maximum years, coronal mass ejections with increased speeds are the main source of strong geomagnetic storms (Gosling et. al. , 1990). Halo CMEs are the type of coronal mass ejections that cause the strongest geomagnetic storms on Earth with Dst values lower than -200 nT (Mishra & Tripati, 2006). Partial halo type CMEs are less geoefficient and make no or little impact on Earth according to their decreased speed (Gopalswamy, 2009). The width of partial halos vary between 120◦ to 360◦ where the full halo has 360◦ width (Gopalswamy, 2009). Depending on the central meridian distance (CMD) of the halos, there are two classes; (1) disk halos with ±45◦ CMD, where it is more likely to hit the Earth and cause geomagnetic storms (2) limb halos with ±45◦ to ±90◦

CMD, where it is likely to hit the Earth by its sides with less geoeffectiveness (Gopalswamy et. al., 2007; Gopalswamy, 2009). Zhang et. al. (2002), also put out that the CMEs occurring within the ±30° latitude interval are found to be the most geoeffective ones, whereas the geoeffective ones are detected as full-halo CMEs by 67% or partial halo CMEs by 30%. Thus, the width and central meridian distance of the coronal mass ejections have been an important classification. So, in addition to the plasma properties within the ICME, also the origin of the CME is playing a significant role on the strength of a geomagnetic storm as well as the structure of it.

2.3 High Speed Streams (HSSs)

2.3.1 Definition and characteristics of high speed streams

Another major solar phenomena causing great disturbances is high speed streams due to their long durations. High speed solar wind streams are the fast outflow (up to 750-800 km/s) of plasma from the open magnetic field lines located in the Sun's coronal holes into the interplanetary medium that can last from days to weeks. Since the high speed solar wind streams carry energetic particles that have disturbed magnetic field paths, where the technological systems are highly affected by the induced radiation with the loss of function (Xystouris et. al., 2013). It is known that high proton fluxes are observed in the interplanetary medium, where it marks to the high plasma velocity with the low density from in the Sun's corona (Zirker, 1977). It explains that HSS are the streams where the energetic particles with high speed are carried into space. Low density and temperature regions of the Sun's corona are defined as coronal holes, where the high-speed solar wind streams that lead to the recurrent geomagnetic disturbances (Zirker, 1977). Coronal holes (CHs) are dark areas that can be seen from EUV imagers on the spacecrafts. Figure 2.8 shows one of the first images of coronal holes taken in 1973 by ASE/ATM Telescope in EUV wavelengths. There is also a pattern about the occurrence of the high speed solar wind streams through the coronal holes. When the solar cycle is in the declining phase, the divergence of the magnetic field lines in the both coronal hemispheres is found to produce a high-speed wind originating near the pole latitudes and the polar coronal holes near solar maximum is found to be waned (Zirker, 1977). Cranmer (2002) also explained that HSSs are dominant at solar minimum and exist over ±20–30◦ latitudes, whereas at lower latitudes the solar wind with lower speed is existent.

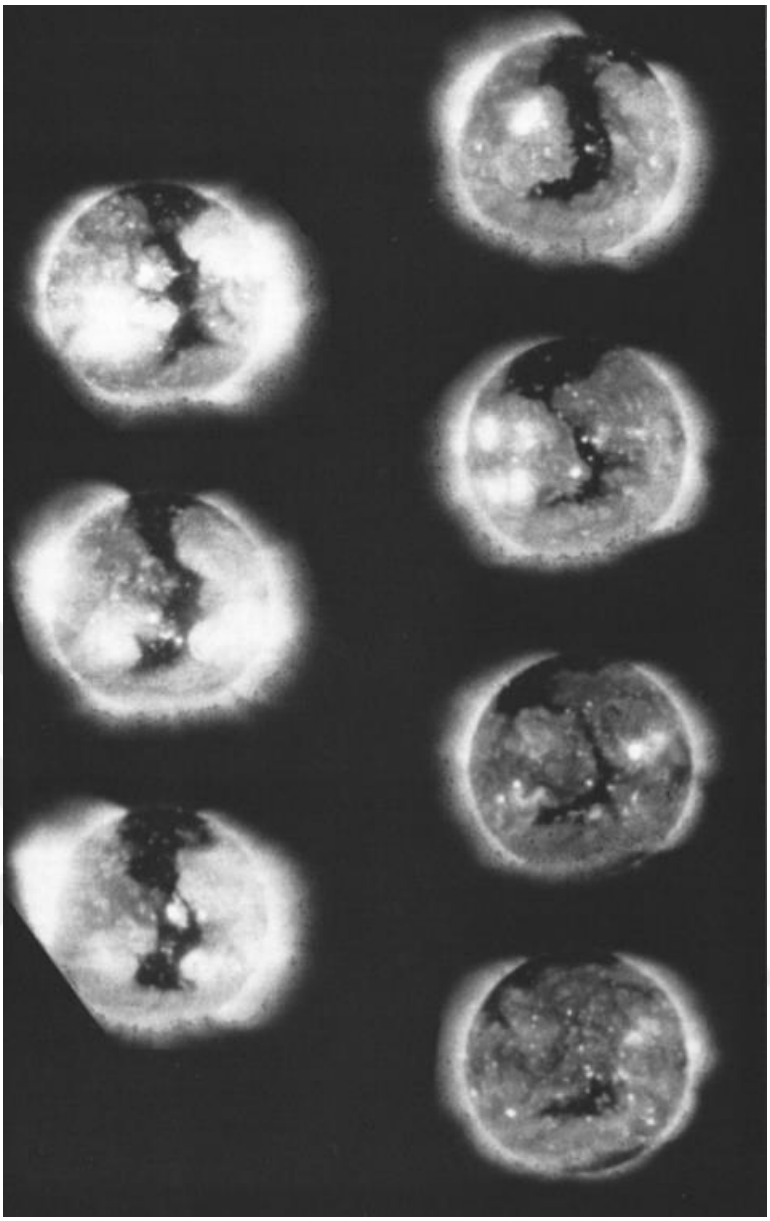

Figure 2.8: Coronal hole images obtained within the Sun's rotation for June 1, June 28, July 25, August 21, September 17, October 14 and November 11 of 1973 by American Science and Engineering, Inc. (ASE)'s Apollo Telescope Mount (ATM) X-ray telescope at 3-32 Å and 44-54 Å wavelengths (Zirker, 1977).

High speed stream of the solar wind is defined as the interval that lasts more than two days, where the maximum daily average speed and the mean value of the speeds immediately preceding and following the stream is greater or equal to 100 km/s (Mavromichalaki et. al., 1988). In Figure 2.9, a high speed solar wind stream near the end of 2008 which lasted more than two days with maximum and leading/ending edge speed differences of more than 100 km/s is shown.

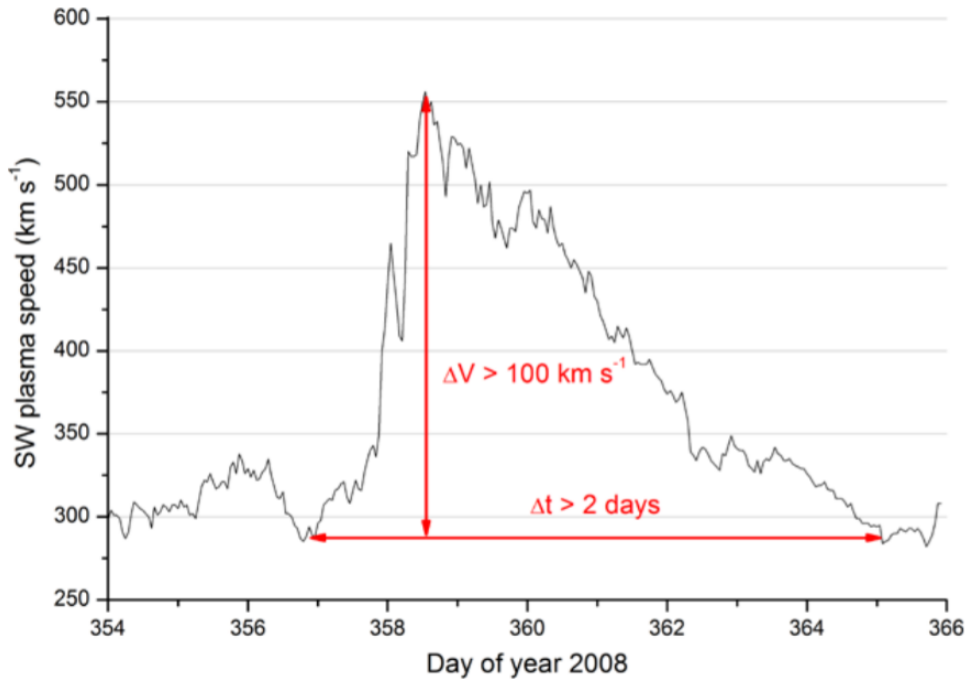

Figure 2.9: A typical coronal hole high speed solar wind stream CH/HSS, where the maximum speed has more than 100 km/s difference with the leading and ending edges of the background solar wind that lasts more than 2 days (Xystouris et. al., 2013).

2.3.2 Structure of high speed streams

The properties of high speed solar wind streams depend on their origin. The origin of high speed solar winds can be corotating coronal holes or solar flare activity (Xystouris et. al., 2013). Depending on the magnetic field magnitude, latitude and longitude of magnetic field, bulk speed and proton density properties, the high speed solar wind streams are separated into two classes: corotating high speed solar wind streams and flare generated high speed solar wind streams (Mavromichalaki et.al., 1988). In Figure 2.10, the measurements for corotating (left) and flare (right) generated high speed solar wind stream types are shown. Xystouris et. al. (2013) also showed in their work that the coronal hole high speed solar wind streams are formed during the descending phase by 72% of the 239 HSSWSs and also during the minimum by 85 % of 104 HSSWSs. In this study, since the origin of the high speed streams are proven to be mostly coronal holes, CH HSS (or CIR/HSS) will be the main focus. The low density and temperature regions, corotating coronal holes, lead the high speed solar wind to catch and compress the previous solar wind flow resulting in a corotating interaction region (CIR). Coronal hole high speed streams (CH HSSs) are also named as corotating interaction region

high speed streams (CIR/HSS). In the high speed solar streams originating from coronal holes, the corotating interaction region (CIR) with strong magnetic field and fluctuations is expected to be the most geoeffective region due to the compressed magnetic field (Verbanac et. al., 2011). Within 27 days of rotation of the Sun, high speed solar streams originating from stable coronal holes can appear again (Kavanagh & Denton, 2007). That is the reason behind the coronal holes to be defined as repetitive, and then the streams are labeled as corotating.

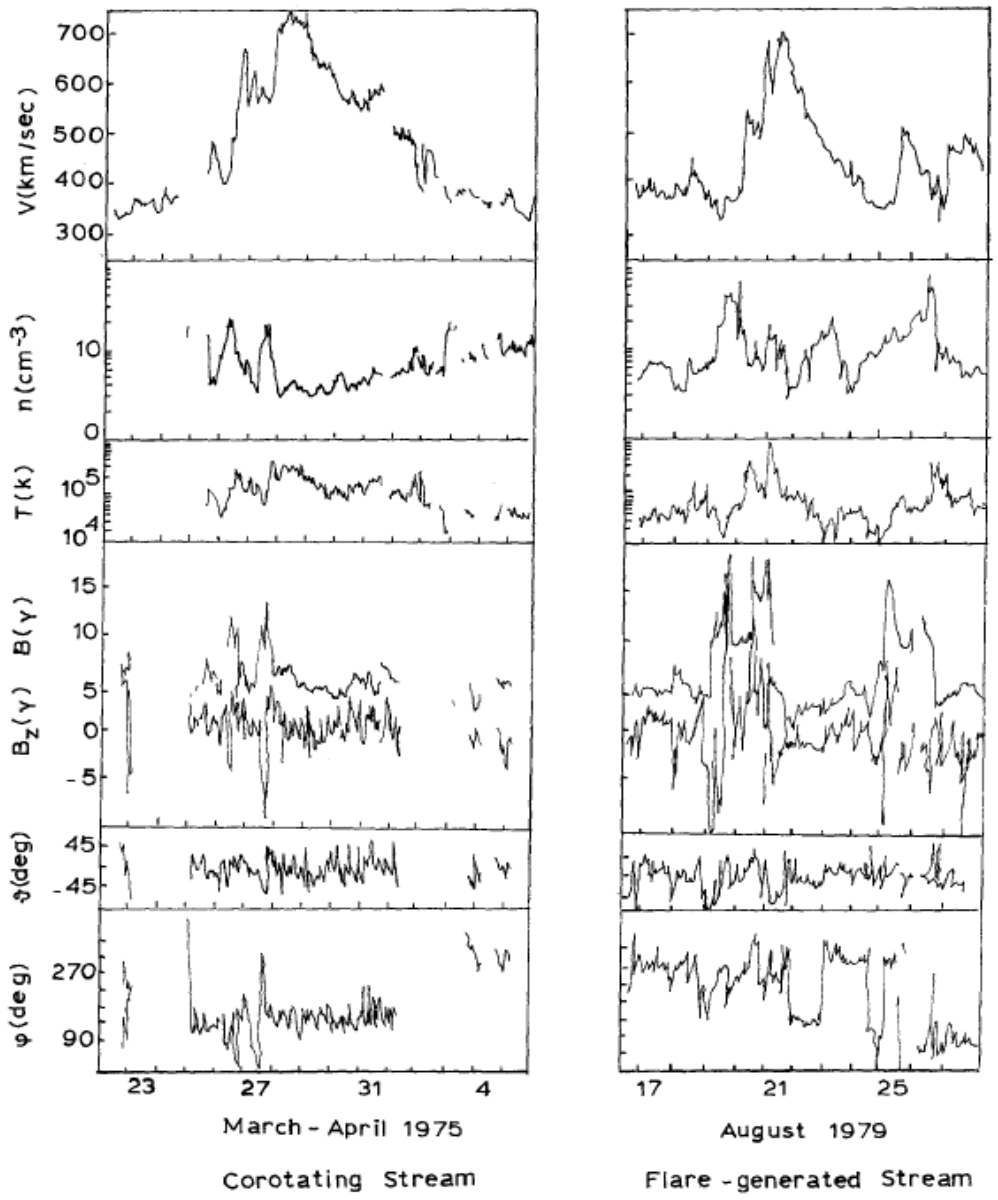

Figure 2.10: Two types of high speed solar wind streams; corotating stream (left) and flare generated stream (right) (Mavromichalaki et. al., 1988).

The typical features of the corotating CH HSSs are explained as; (1) rapid increase of proton density in the leading edge (2) proportionality in the interplanetary magnetic field and bulk speed (3) similarity in the proton temperature variation with flow speed (Mavromichalaki & Vassilaki, 1998). Also there can be seen fluctuations in the density and speed of the flow. CIR/HSS features are also explained by Cavanagh and Denton (2007) as increased solar wind speed staying steady for a few days, interaction region where the solar wind direction is switching from east to west, first an increase of the density followed by a decrease to minimum, and maximum in the magnetic field where the density and magnetic field strength reach the maximum at the same time due to the frozen in flux condition. The maximum values of the density and magnetic field are seen before the speed is increased, later the density decreases even below the previous level due to the rarefaction of the fast speed flow (Cavanagh and Denton, 2007).

2.3.3 Measurements and observations of high speed streams

High speed streams are not directly observable structures with the images. Since they mostly originate from the coronal holes, more dark and less hot areas on the solar corona, the observations of coronal holes might help the researchers to get clues. To observe coronal holes, extreme ultraviolet (EUV) or soft X-ray imagers or telescopes on board are used. Another method to observe coronal holes is the wavelength of Helium absorption at 1083 nm (SWS, n.d.). SOHO's Large Angle and Spectrometric Coronagraph (LASCO) and EUV Imaging Telescope (EIT) imagery are also a source for coronal images. However, EUV imagery taken from the Atmospheric Imaging Assembly of the Solar Dynamics Observatory (SDO/AIA), which is a four-telescope array, is the most prefered source. Coronal Hole Identification via Multi-thermal Emission Recognition Algorithm (CHIMERA) is detecting coronal hole boundaries by the analyses of multi-thermal images of (SDO/AIA) 171Å, 193 Å and 211 Å passbands (Garton et. al., 2017). Coronal holes are mostly visible in the 193 Å wavelength, due to their low temperature and density caused by escaped energetic particles from open magnetic field lines. In Figure 2.11, coronal holes at a polar and a low latitude at 195 Å wavelength are observed from Extreme ultraviolet Imaging Telescope (EIT) of SOHO. With the detection of the coronal hole high speed solar streams (CIR/HSSs) through remote sensing observations, the structure of them is

determined with in-situ measurements from on board spacecrafts. In Figure 2.12, the average parameters through in-situ measurements of CIR/HSSs are shown.

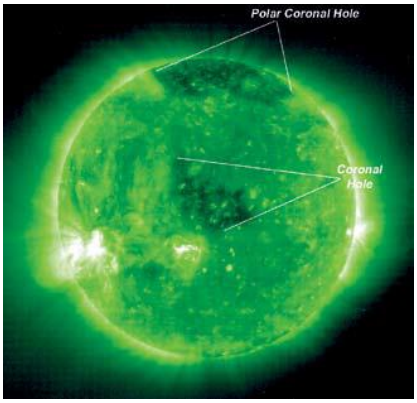

Figure 2.11: Coronal hole observation at 195 Å bandpass by SOHO on 6 October 2005. (SOHO/EIC consortium, taken from Kavanagh & Denton, 2007).

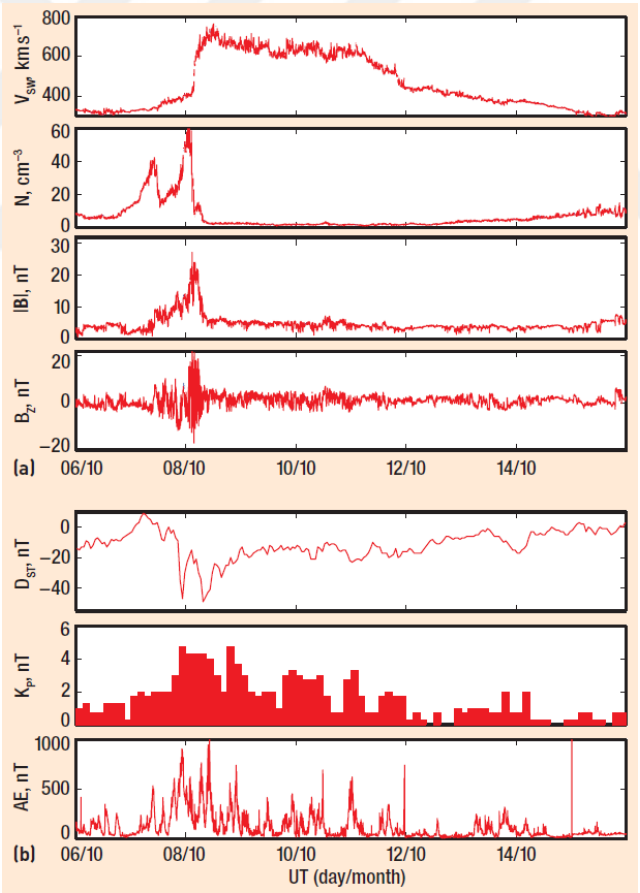

Figure 2.12: Typical marks of an CIR/HSS (or CH HSS) through in-situ measurements where the rapid increase in density is followed by magnetic field, and latter the increase in solar wind speed is started by the drop in density levels (Kavanagh & Denton, 2007).

CIR/HSSs are generally detected from the changes in the background solar wind conditions measured from on board spacecrafts at L1 orbits during its passage. A few hours or days prior to the arrival of the energetic particles to Earth, it can be forecasted easily. SOHO, Wind and ACE spacecrafts in L1 point are providing solar wind plasma and magnetic field data that can be used for the analyses of HSSs. Also, CIR/HSS catalogues are present (HELIO4CAST/SIRCAT, GS-HSS Catalogue of Institute for Space Sciences and Institute of Geodynamics of the Romanian Academy etc.) that classify the event intervals, durations and some important parameters.

2.3.4 Effects of high speed streams on space weather and Earth

High speed solar wind streams (HSSs) also can affect the Earth in different levels when other solar events are considered. CIR-driven storms last longer, have higher electron fluxes, hotter and denser plasma which leads to stronger spacecraft charging and likely to be a problem mostly for space-based systems (Borovsky & Denton, 2006). Solar wind flow is a major driving phenomena on Earth for geomagnetic storms, solar radiation storms, and radio blackouts (Xystouris et. al., 2013). The passage of a high speed solar wind near Earth is likely to create disturbances. Geomagnetic storms can be also driven by coronal hole (or corotating) high speed solar wind streams, apart from coronal mass ejections. During the descending phase of solar activity the coronal holes tend to repeat, resulting with the disturbances in the magnetosphere for a few days while their input can be energy input of the driven storm of high speed solar wind stream can be as high as the ones driven by coronal mass ejections (Kavanagh & Denton, 2007). Verbanac et. al. (2011) performed an analysis showing that CIR/HSS events drive mostly weak (-50 nT $<$ Dst $<$ -30 nT) to moderate (-90 nT $<$ Dst $<$ -70 nT) geomagnetic storms. Major geomagnetic storms driven by CIR/HSSs with the Dst $<$ -100 nT rarely occur (Tsurutani et. al., 2006). Mavromichalaki et.al. (1988) put out that the Ap index, daily geomagnetic activity, showed a correlation of 0.43 with the maximum speed during the corotating high speed solar streams originated in coronal holes. Which explains that the speed of the solar wind flow is one of the factors controlling the geoactivity on Earth.

2.4 Differences Between Coronal Mass Ejections and High Speed Streams

There are differences between CMEs and HSSs for their origin, occurrence and driven storms that tend to play a great role in the geomagnetic activity which was explained in the previous sections. Figure 2.13 briefly explains the basic structural differences between two phenomena mentioned in the previous sections.

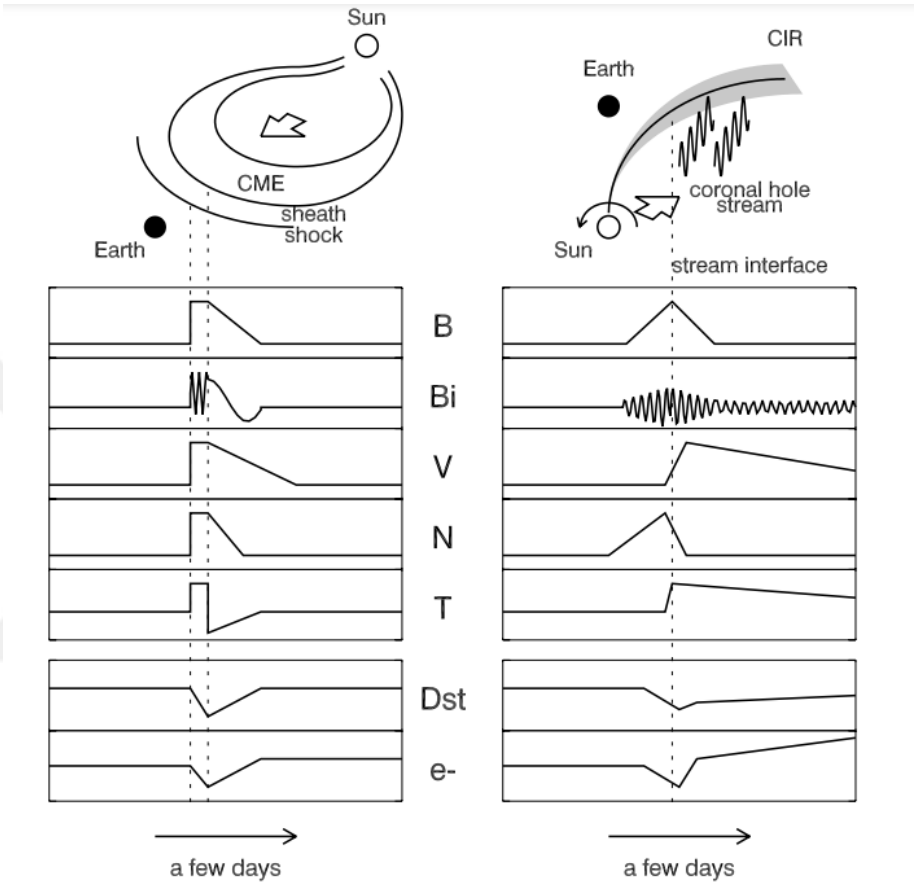

Figure 2.13: Schema of typical solar wind properties of coronal mass ejections (left) and corotating interaction region high speed streams (right). The parameters from top to bottom respectively: Magnetic field strength, southward magnetic field, solar wind speed, density, temperature, Dst index and electron flux (Kataoka & Miyoshi, 2006).

Interplanetary coronal mass ejections formed in the closed magnetic field areas and corotating interaction regions due to the high speed streams flowing through open magnetic field lines are two of the large-scale structures in the interplanetary medium depending on the different magnetic field orientations of the Sun (Gopalswamy, 2007). HSSs originate from the open magnetic field lines, where the particles escape into space. On the other hand, CMEs originate from closed magnetic field lines. Their occurrences also change depending on the solar cycle phases. High speed solar wind streams that dominate during the solar minimum years and lead to the more significant

processes for long durations, compared with less durable geomagnetic storms driven by coronal mass ejections (Kavanagh & Denton, 2007). Differently, coronal mass ejections dominate the solar maximum years. Another difference is their generated storms. Interplanetary magnetic field is one of the main parameter causing the difference of CIR/HSS and CME driven geomagnetic storms because the long duration and persistent pattern for southward component during CME passage is increasing the energy exchange to the system by enhanced reconnection of the dayside magnetosphere, while the shorter and less persistent intervals of it cause smaller dayside reconnection for CIR/HSS (Kavanagh & Denton 2007). Due to this, CME-generated storms are found to be more intense than CIR/HSS generated storms. More details about the geomagnetic storms will be discussed in the next sections.

2.5 Geomagnetic Storms

2.5.1 Definition, characteristics and generation of geomagnetic storms

A geomagnetic storm is one of the consequences of the solar activity on Earth. It is a major disturbance caused by the interaction of the solar wind with the Earth's magnetosphere. Geomagnetic storm effects on Earth can be disruptive. Intense geomagnetic storms can cause disruption in the signals of GPS/GNSS that affect navigation systems. They can also lead to radio communication blackouts, disruption in the power grids and pipelines or increased radiation risks for the airline passengers. The enhanced currents and increased ionospheric density from precipitated energetic particles into the ionosphere, and thus increased Joule heating, can exert an extra drag on LEO orbit satellites and might even lead to loss. Different drivers can lead to geomagnetic storms with different intensity. Major solar phenomena such as coronal mass ejections or corotating high speed streams can be the driver. Gonzalez et. al. (1994) defines the geomagnetic storm as the interval where the convection electric fields increase the ring current to overreach the storm identifying Dst index value in the highly energized magnetosphere-ionosphere system. It generally originates when there is an efficient exchange of energy from solar wind to the magnetosphere driving the currents and enhancing electric fields. Three current systems are found to be responsible from geomagnetic storm generation; Chapman-ferraro current that also initiates the storm, ring current around the Earth leading the main phase; auroral electrojets, which are enhanced currents in the ionosphere (Akasofu, 2018).

2.5.2 Phases of geomagnetic storms

As it is explained in the previous section, there are three phases of a geomagnetic storm: initial phase, main phase and recovery phase. Each phase has a different contribution in solar wind-magnetosphere dynamo. Thus it is important to consider the storm phases separately for magnetospheric studies. The geomagnetic storm phases are generally detected from the Dst (Disturbance storm time) index. In Figure 2.14, the corresponding geomagnetic storm phases are marked with green, pink and blue respectively for initial, main and recovery phases of the storm.

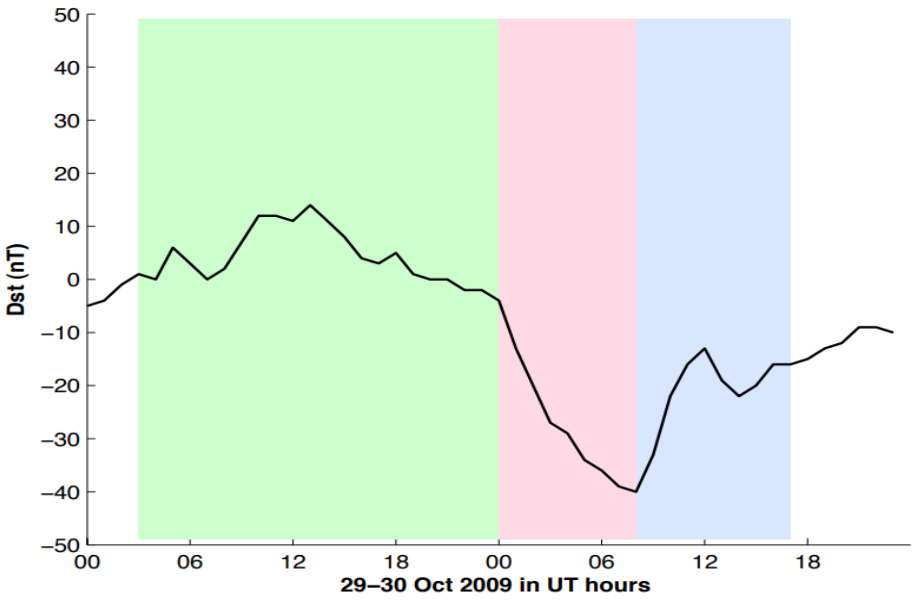

Figure 2.14: Dst index over time during a typical geomagnetic storm observed on 29-30 October 2009, showing initial phase (green), main phase (pink) and recovery phase (light blue). (Partamies et. al.., 2013).

2.5.2.1 Initial phase

The increase in the intensity of the low latitude horizontal magnetic field on Earth is the geomagnetic storm initial phase that can last hours to days (Tsurutani et. al., 2006). It is observed with the positive increase of the Dst index. Therefore the criteria for storm initial phase is Dst > 0 nT until the main phase starts (Partamies et. al., 2013). SSC is the disturbance in the magnetic north component measured by the geomagnetic activity observatories showing the signs of a shock wave arrival to the magnetosphere (Kumar & Singh, 2013). Initial phases in ICME driven storms generally have Storm

Sudden Commencement (SSC) that initiates the storm, differently from the CIR/HSS driven ones due to the fast forward shocks.

2.5.2.2 Main phase

Main phase of a geomagnetic storm is the phase just after the initial phase ends. It starts with storm onset (SO). The main phase of a geomagnetic storm is mainly due to the enhanced ring current of the magnetosphere, where the measured horizontal magnetic field intensity is decreasing at low latitudes (Tsurutani et. al., 2006). The storm main phase generally starts with a rapid decrease of Dst index where the decrease is dDst/dt <−2 nT/h with at least -15 nT Dst (Partamies et. al., 2013).It generally lasts until the local minimum Dst value is reached. Dst decreases in ICME driven storms for the main phase are generally smooth and rapid than the CIR/HSS driven storms and they reach a smaller minimum value.

2.5.2.3 Recovery phase

The recovery phase is the third and the most long lasting interval of a geomagnetic storm. The recovery phase is the last phase of a geomagnetic storm where the horizontal component of disturbed geomagnetic fields reach to the background levels (Tsurutani et. al., 2006). It starts from the local minimum of the Dst index until it reaches values more than -15 nT (Partamies et. al., 2013). Recovery phases in ICME driven storms generally last shorter (from hours to 1-2 days) with a full recovery than the CIR/HSS driven storms. In case of CIR/HSS driven storms, the recovery phase can last more days, and the full recovery can not be clear as in ICME driven storm cases.

2.5.3 Measurements and observations of geomagnetic storms

Geomagnetic storms are detected by magnetic activity indices derived by near-equatorial magnetometers. There are two main indices used to determine the intensity of a geomagnetic storm; Dst (disturbance storm time) and Kp (planetary-K). Dst index is the magnetic activity index derived from low latitude geomagnetic observatories

which measures the hourly ring current intensity (NOAA, n.d.). Figure 2.15 represents the Dst network on Earth consisting of four observatories.

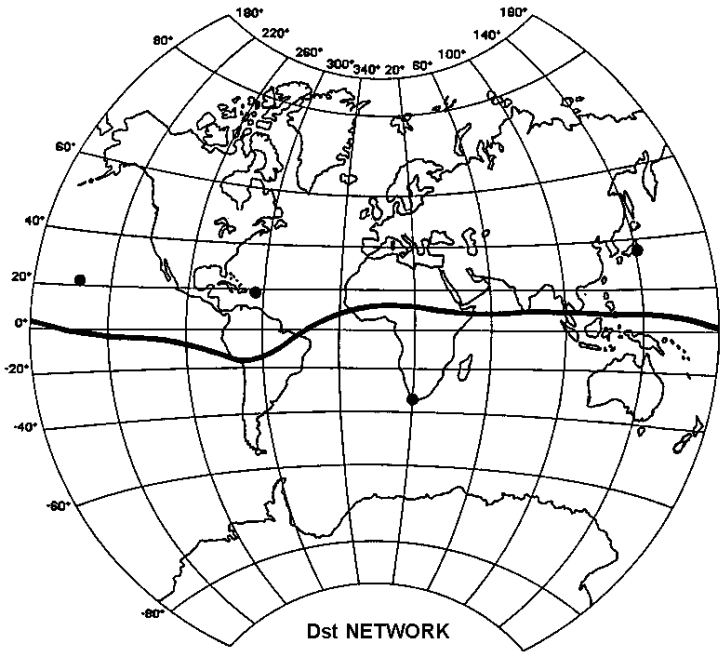

Figure 2.15: The Dst network consisting of four observatories near the equator (Hermanus, Kakioka, Honolulu, and San Juan) . (World Data Center for Geomagnetism, n.d.).

Geomagnetic storms are classified regarding their intensities; weak, moderate, strong, severe and great (Loewe & Prölss, 1997). Weak storms have -30 nT<Dst<-50 nT values and maximum Kp value as 4, moderate storms have -50 nT<Dst<-100 nT values and maximum Kp value as 5, strong storms have -100 nT<Dst<-200 nT values and maximum Kp value as 6.67, severe storms have -200 nT<Dst<-350 nT values and maximum Kp 8.33 and finally great storms have -350 nT<Dst values and maximum Kp value as 8.67 (Loewe & Prölss, 1997). The planetary K (Kp) index is used to determine the magnitude of the geomagnetic storm from the level of measured disturbances of the horizontal magnetic field of Earth by magnetometers during a three hour interval (NOAA, n.d.). Kp index varies from 0 to 9, where a minor geomagnetic storm is defined with Kp 5, a moderate geomagnetic storm is defined with Kp 6, a strong geomagnetic storm is defined with Kp 7, a severe geomagnetic storm is defined with Kp 8 and finally, an extreme geomagnetic storm is defined with Kp 9 (NOAA, n.d.).

2.5.4 CME and HSS driven geomagnetic storms

Coronal mass ejections and high speed solar wind streams are responsible from the geomagnetic activity on Earth, such as geomagnetic storms. Regarding their differences in the origin and evolution, their storm phase drivers and intensity are different. Tsurutani et. al. (2006) clarified that coronal mass ejection (ICME) driven and high speed solar wind stream (CIR/HSS) driven geomagnetic storms both consist of three phases; initial, main and recovery while their generation reason differ from each other. ICME driven geomagnetic storm initial phase has clearly different from CIRs due to the fast forward shock causing storm sudden commencement and sudden impulse; where the main phase has two features such as; a smooth dst decrease with time and also storms occurring with Dst < - 100 nT, different than CIR driven ones; and the recovery phase takes 7 to 10 hours with the ring current particle loss with some processes (Tsurutani et. al. 2006). Initial phases of geomagnetic storms driven by high speed streams are explained by the initiation resulted from increase of the ram pressure; the main phase is explained to initiate from the magnetic reconnection of fluctuating southward magnetic field where the particle injection to the ring current is relatively low, thus causing weak storm intensity; long duration recovery phases that last also long are mostly explained by southward Alfven wave reconnection where the recovery phases are not considered as pure (Tsurutani et. al., 2006). The typical pattern for a geomagnetic storm generated by an ICME (solar maximum) shows signatures of storm sudden commencement followed by the storm onset which refers to the initial phase interval with positive Dst, then main phase is followed by a sharp decrease and recovery phases are followed as it is seen from Figure 2.16. During solar minimum CIR/HSSs, the geomagnetic storm does not have storm sudden commencement as ICMEs have, then the initial phase starts with storm onset followed by the main phase with a slight and fluctuating decrease in Dst index until the long recovery phase starts (see Figure 2.16). The end of the recovery phase for CIR/HSS driven storms is not as clear as it is in ICME driven ones and it takes from hours to days for a full recovery.

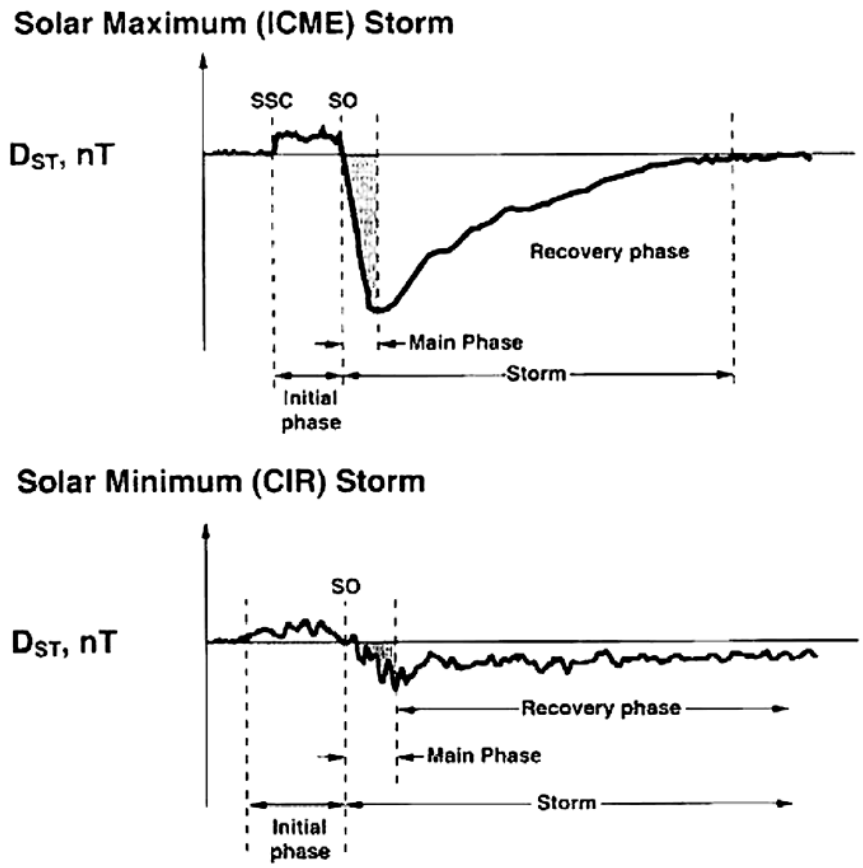

Figure 2.16: Typical patterns of Dst index over time during geomagnetic storms driven by ICMEs (top) and CIR/HSSs (bottom) with intervals of SSC, SO, initial phase, main phase and following recovery phase. (Tsurutani et. al., 2006).

The intensity of a geomagnetic storm also differs by their driver type. Coronal mass ejections tend to produce higher intensity storms than high speed solar wind streams as drivers, since they occur generally around solar maximum rather than solar minimum years. Corotating high speed streams are not the drivers of major storms with Dst values lower than -100 nT, they are only responsible for moderate or weak storms where the Dst varies between -25 nT and -100 nT (Tsurutani et.al., 1995). The geomagnetic storms with Dst values lower than -100 nT generally occur around the maximum of the solar cycle with the following increase in coronal mass ejections (Tsurutani et. al., 2006). Finally there are some studies about CME and CIR/HSS driven storms to compare their intensity and different features. Figure 2.17 gives a brief list of the features of CME and CIR/HSS driven storms. Coronal mass ejection driven storms in general are more intense geomagnetic events with higher plasma sheet density and temperature, stronger ring current and geomagnetically induced currents (see Figure 2.17).

Phenomenon	CME-Driven Storms	CIR-Driven Storms
Phase of the solar cycle when dominant	solar maximum	declining phase
Occurrence pattern	irregular	27-day repeating
Calm before the storm	sometimes	usually
Solar energetic particles (SEP)	sometimes	none
Storm sudden commencement (SSC)	common	infrequent
Mach number of the bow shock	moderate	high
β of magnetosheath flow	low	high
Plasma-sheet density	very superdense	superdense
Plasma-sheet temperature	hot	hotter
Plasma-sheet O^+/H^+ ratio	extremely high	elevated
Spacecraft surface charging	less severe	more severe
Ring current (Dst)	stronger	weaker
Global sawtooth oscillations	sometimes	no
ULF pulsations	shorter duration	longer duration
Dipole distortion	very strong	strong
Saturation of polar-cap potential	sometimes	no
Fluxes of relativistic electrons	less severe	more severe
Formation of new radiation belts	sometimes	no
Convection interval	shorter	longer
Great aurora	sometimes	rare
Geomagnetically induced current (GIC)	sometimes	no

Figure 2.17: Typical features of geomagnetic storms driven by ICMEs and CIR/HSSs. (Borovsky & Denton, 2006).

Chen et. al. (2014) summarized the geomagnetic storm differences as; CME driven storms last less than two days and they are stronger and have stronger ring currents and great aurorae, where the CIR/HSS driven storms last longer than a few days and they are weaker with less great aurorae. On the other hand, weaker storm intensity does not mean that it has to affect everything in a weaker way. CIR/HSS driven storms can also have remarkable effects on the Earth's atmosphere. Also, it is stated that CIR/HSS driven geomagnetic storms can affect the thermospheric density, which is the most important factor for satellite drag, as similar as in ICME driven ones or more since their duration are longer, even though that their maximum Joule heating values are very small compared with ICME driven storms for the whole interval (Chen et. al., 2014). This study leads to the idea of comparison of produced Joule heating during storm intervals of ICME and CIR/HSS as drivers.

2.6 Energy Exchange Processes During Geomagnetic Storms

During geomagnetic storms, there is an ongoing exchange process in the solar wind-magnetosphere system. Energy input to the magnetosphere is in significant amounts during storms, thus it is important to determine the total energy dissipated into the Earth's atmosphere. Epsilon parameter is the generated power of solar wind-

magnetosphere coupling explaining how much energy is exchanged. Solar wind-magnetosphere energy coupling function (Akasofu, 1981) is shown in equation 2.1.

$$\varepsilon = \nu B^2 \sin^4(\frac{\theta}{2})\, l_0^2 \ [\text{ergs}^{-1}] \tag{2.1}$$

The Epsilon parameter is later converted in SI units (ergs^{-1} to W) by Koskinen & Tanskanen (2002) as it is shown in equation 2.2.

$$\varepsilon = \frac{4\pi}{\mu_0}\nu B^2 \sin^4(\frac{\theta}{2})\, l_0^2 \ [\text{W}] \tag{2.2}$$

In equation 2.1, V represents the solar wind speed, where B is the magnitude of interplanetary magnetic field, θ is the polar angle of magnetic field line on the Y-Z plane and l_0 is the constant approximately 7 R_E. Energy input is estimated with the integration of Epsilon (ε) parameter over time, where the solar wind speed and the magnetic field are the two variables in addition to theta. From the orders of variables, it is seen that the most input comes from theta, then magnetic field and the least from the solar wind speed. The energy source of the magnetosphere is mainly the interplanetary magnetic field and the solar wind (Pulkkinen et. al., 2002). Theta varies between 0 (northward) and 180 (southward), where we can estimate that the southward clock angle makes the highest contribution to the energy dissipation. Also the $(4\pi/\pi_0)\nu B^2$ terms as a whole represents the Poynting flux per unit area multiplied by 4π (Koskinen & Tanskanen, 2002). Energy dissipation from solar wind to magnetosphere is mainly in the form of with ring current, ionospheric Joule heating and auroral particle precipitation (Baker et. al., 2000). For the energy exchange in the solar wind- magnetosphere system, source is the solar wind kinetic energy and the sink is the total dissipation. Since the energy transfer to the magnetosphere can not be measured directly, the dissipation rates are used to estimate by the help of ionospheric and magnetospheric indices (Tenfjord & Østgaard, 2013). To compare the energy generated and dissipated, the total energy consumption in the magnetosphere (U_T) is used. It is the sum of the energy dissipation by Joule heating (U_J), auroral particle

precipitation (U_A) and ring current particle injection (U_R) as it is seen in equation 2.3 (Tenfjord & Østgaard, 2013).

$$U_T = U_J + U_A + U_R [GW] \quad (2.3)$$

Tenfjord & Østgaard (2013) explains the total energy dissipation (U_T) by Joule heating (U_J), auroral particle precipitation (U_A) and ring current particle injection (U_R) respectively by equations 2.4, 2.5 and 2.6. First contribution to the total energy dissipation is from ionospheric Joule heating. Joule heating is generated due to the Pedersen currents that are related to the closing field aligned-currents through the resistive ionosphere (Koskinen & Taskanen, 2002). Joule dissipation U_J power during solstice for both hemispheres within the total energy dissipation is estimated by the equation 2.4 (Tenfjord & Østgaard, 2013).

$$U_J = 0.54AE + 1.8 [GW] \quad (2.4)$$

AE variable in the U_J formula is Auroral Electrojet Index, which shows the global electrojet activity obtained from the variations in the horizontal component of magnetic field that is measured from the observatories within the auroral zone in the higher latitudes of northern hemisphere (World Data Center for Geomagnetism, n.d.). The second process contributing to the total energy dissipation is auroral particle precipitation. The energetic particles (ions and electrons) in the magnetosphere precipitating into the atmosphere and lead to the formation of an aurora is called auroral particle precipitation (Ni et. al., 2016). Auroral particle precipitation U_A power within the total energy dissipation is estimated by the equation 2.5 (Tenfjord & Østgaard, 2013).

$$U_A = 4.4AL_{QL}^{1/2} - 7.6 [GW] \quad (2.5)$$

The quick look AL variable in the U_A formula is the lower envelope of the Auroral Electrojet Index, where AE is defined by (AU - AL) (World Data Center for

Geomagnetism, n.d.). Another energy dissipation process is explained with ring current injection. Ring current is the westward current occuring due to the westward drifting ions and eastward drifting electrons circulating around Earth is called ring current (Fitzpatrick, 2011). Ring current particle injection power U_R power within the total energy dissipation is estimated by the equation 2.6 (Tenfjord & Østgaard, 2013).

$$U_R = -4 \times 10^4 \left(\frac{\partial Dst^*}{\partial t} + \frac{\partial Dst^*}{\tau}\right) [GW] \quad (2.6)$$

In the formula, τ is given as the ring current decay rate that is 4 hours when the Dst^* is less than −50 nT, 8 hours when the Dst^* is less than −30 nT and finally 20 hours when the Dst^* is higher than −30 nT, respectively. In the literature, it is revealed that energy dissipation factors $U_J, U_A \; and \; U_R$ have different contributions to the total energy dissipation power U_T. Baker et. al. (2000) put out that the Joule heating and auroral particle precipitation are the most dominant dissipation types and also Akasofu's epsilon parameter is sufficient to calculate the energy coupling from the solar wind during geomagnetic storms. The linear regression analysis performed by Lu et. al. (1998) showed that Joule heating (U_J) is highly correlated with AE parameter with the Pearson coefficients of 0.91 for the northern and 0.76 for the southern hemispheres among other dissipation processes. Thus, in this work, it is decided to analyze the ionospheric Joule heating during the geomagnetic storms driven by ICMEs and CIR/HSSs.

3. UPPER ATMOSPHERIC JOULE HEATING

3.1 Definition and Estimations of Joule Heating

It is known that Joule heating of the ionosphere is the most contributing dissipation type as an energy sink for solar wind-magnetosphere-ionosphere energy exchange processes during geomagnetic storms. It was investigated and defined in the 1960s by K. D. Cole for the first time. Joule heating is resulted from the ionospheric currents driving the geomagnetic disturbances (Cole, 1962). Palmroth et. al. (2005) defines Joule heating as the term describing the Ohmic heat production that can be obtained from the scalar product of the current and electric field, which occurs due to the collision of charged particles drifting parallel to the electric field and neutral particles in the medium. Joule heating arises due to the conversion of the drift velocities into thermal energy by charged particles under an existing electric field causing ion upwelling and winds (Russian Geomagnetic Database, n.d.). Later, electric current density and field vectors are found to be the main parameters to calculate Joule heating rate (Pradhan & Singh, 1979). Total Joule heating dissipation is given in equation 3.1, where the Hall current is given in equation 3.2 and the net Pedersen current is given in equation 3.3 (Pradhan & Singh, 1979). E_i refers to the original induction field, J_p represents the net Pedersen current and finally Cowling conductivity (σ_3) is present as a combination of Hall (σ_2) and Pedersen (σ_1) conductivities.

$$Q = J_p E_i = \frac{J_p^2}{\sigma_3} \tag{3.1}$$

$$J_p = (\sigma_2^2/\sigma_1)E_i \tag{3.2}$$

$$J_p = \sigma_1 E_i + (\sigma_2^2/\sigma_1)E_i = \sigma_3 E_i \tag{3.3}$$

From the equation 3.1, it is revealed that the polarization field contribution is more, and the Hall current is the major current (Pradhan & Singh, 1979). Another estimation

equation derived with neutral wind contribution by Vickrey et. al. (1982) shown in equation 3.4, where the $E_{\perp}$is the perpendicular electric field to the magnetic field (B), Σ_P is the height dependent Pedersen conductivity and U is the neutral wind velocity which is dependent on the height. Thus the height-integrated Joule heating (Q_J) is as follows.

$$Q_J = \Sigma_P[E_{\perp} + \text{U x B}]^2 \tag{3.4}$$

The relationship between Joule heating and Poynting's vector (E x ΔB / μ_0) was revealed by Sugiura (1986); dissipation of Joule heating is equal to the vertical Poynting vector representing the vertical downward energy flow with the assumption of zero divergence of horizontal energy flux. The Poynting flux represents the electromagnetic energy amount transmitted to the ionosphere; energy inflows when it is negative and flows out when it is positive (Rastaetter et. al., 2016). In this equation, the neutral wind is assumed as U=0. Since the neutral wind (U) is mostly smaller than the ionospheric plasma drift (E x B), it is generally neglected but it can enhance the local Joule heating calculations by the factor of 2 or 4 (Beaujardiere et. al., 1988). Empirical linear relations of Joule heating obtained from coherent radars with Kp and AE geomagnetic activity indices are obtained by Kosch & Nielsen (1995) as it is shown in equation 3.5 and equation 3.6.

$$Q_J = 3.85 \text{ x } 10^{-4} \text{ x } K_p^{1.98} \text{ [W/}m^2\text{]} \tag{3.5}$$

$$Q_J = -6.85 \text{ x } 10^{-4} + 1.80 \text{ x } 10^{-5} \text{ x } AE \text{ [W/}m^2\text{]} \tag{3.6}$$

When the magnetic field strength is negative, the ionospheric electric field is remarkably enhanced by about an hour of delay from the change of field direction (Kosch & Nielsen, 1995). Later, with the satellite measurements the global Joule heating dissipation estimation is performed. In equation 3.7, hemispheric global Joule heating rate is given (Macmahon & Gonzalez, 1997); $\theta_c, \lambda, h, \Sigma_P, E$ represents

respectively the geomagnetic colatitude, geomagnetic longitude, ionospheric altitude (110 km), Pedersen conductance and electric field.

$$U_j = \int_0^{\theta_c} \int_0^{2\pi} \Sigma_P \, E^2 (R_E + h)^2 \sin\theta d\theta d\lambda \tag{3.7}$$

Another method is discussed by Vasyliunas & Song (2005) to estimate Joule heating, which is described as frictional heating arising from the plasma and neutral motion, by taking the electric field in the reference of plasma, instead of neutrals. But the study of Strangeway (2012) showed that, the reference frame of neutrals frame the Joule dissipation have all the heatings from different fluid collision terms, thus Joule dissipation term is suggested to use. Poynting flux is also used as another way of estimating Joule heating. Since the Poynting flux is referring both to the energy from Joule heating dissipation and the mechanical energy consumed by the neutral winds, it can be used to estimate Joule heating (Palmroth et. al., 2005).

3.2 Measurements and Observations of Joule Heating

Joule heating results with changes in ionosphere and thermosphere globally such as neutral temperature change, mean molecular mass change and the decrease of concentration of electrons in the F-region peak (Rodger et. al., 2001). The expansion caused by this heating is posing a great risk of atmospheric drag for LEO satellites. Thus, it is important to estimate the heating rate. Since it is not a directly observable quantity, it is measured through combined methods such as ground measurement with radars, sounding rockets, remote sensing with satellites and their imagers, also with global MHD models. Rocket measurements were one of the first measurement source options to obtain electric field and magnetic field data to estimate heating covering a small area. For the electric and magnetic field measurements, satellites are in use. The data resolution of conductivity and electric field measurements is important to estimate accurate Joule heating rate. For the conductivity measurement, auroral images obtained from satellites are also used. Radars are also in use to obtain data. Incoherent scatter radars back in time were used for the ground based measurements, as only option, of electron density, electric field and neutral wind vectors; all parameters in

the height-integrated Joule heating (equation 2.2) estimations (Beaujardiere et. al., 1988). Chatanika and European Incoherent Scatter are some examples. Another method to measure Joule heating is coherent radars. The high resolution Scandinavian Twin Auroral Radar Experiment (STARE) and Britain Radar Experiment (SABRE) bistatic coherent radars were in use around the 1980s as well (Kosch & Nielsen, 1995). Assimilative Mapping of the Ionospheric Electrodynamics (AMIE) is also another method developed by Richmond (1992), about combining direct and indirect observations. Figure 3.1 explains the AMIE procedure by its components. It aims to observe the electromagnetic quantities by radar, satellite and ground measurements and electrostatic potential by statistical model, then obtain the conductances. Super Dual Auroral Radar Network (SuperDARN) is one of the most used coherent scatter radar systems, which is a high-frequency (HF) radar network containing more than 35 radars covering southern and northern hemispheres providing a large variety of data.

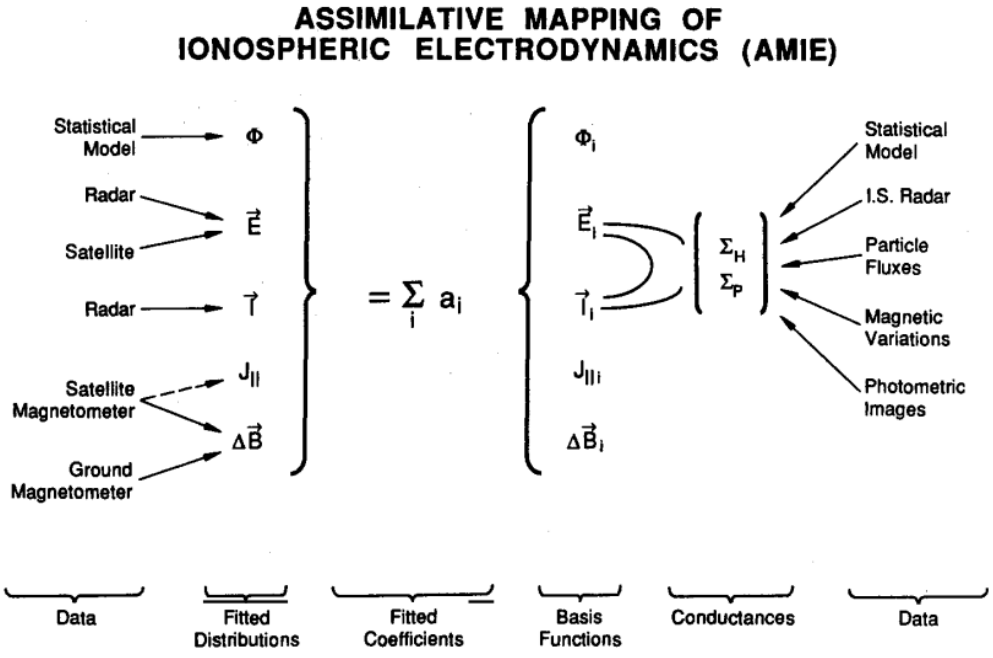

Figure 3.1: Schematic diagram of AMIE procedure (Richmond, 1992).

Combined methods are used in the literature for global integrated Joule heating estimations. Palmroth et. al. (2005) estimated Joule heating in four ways; (1) observed from the SuperDARN radar by taking the global electric field and from UV and X-ray channels of Polar global imagers, (2) used AE and Kp indices as proxies to calculate from empirical relations, (3) computed by using Assimilative Mapping of the

Ionospheric Electrodynamics (AMIE) method and (4) GUMICS-4 MHD Model coupling the magnetosphere with the high-resolution electrostatic ionosphere. Figure 3.2 shows the total integrated Joule heating estimated on 28–29 March 1998 by three methods. It is found that the AE-proxy is giving the most probable temporal variation compared with AMIE or Kp-proxy methods, in addition to the GUMICS-4 estimation of the Joule heating, which gives the results 10 times lower than the actual values even though the temporal evolution was consistent with actual Joule heating because the model does not include neutral wind effects (Palmroth et. al., 2005) . In Figure 3.3, Joule heating comparison of calculations from SuperDARN and Polar satellites with GUMICS-4 MHD model simulations are shown, with the difference by a factor of 10.

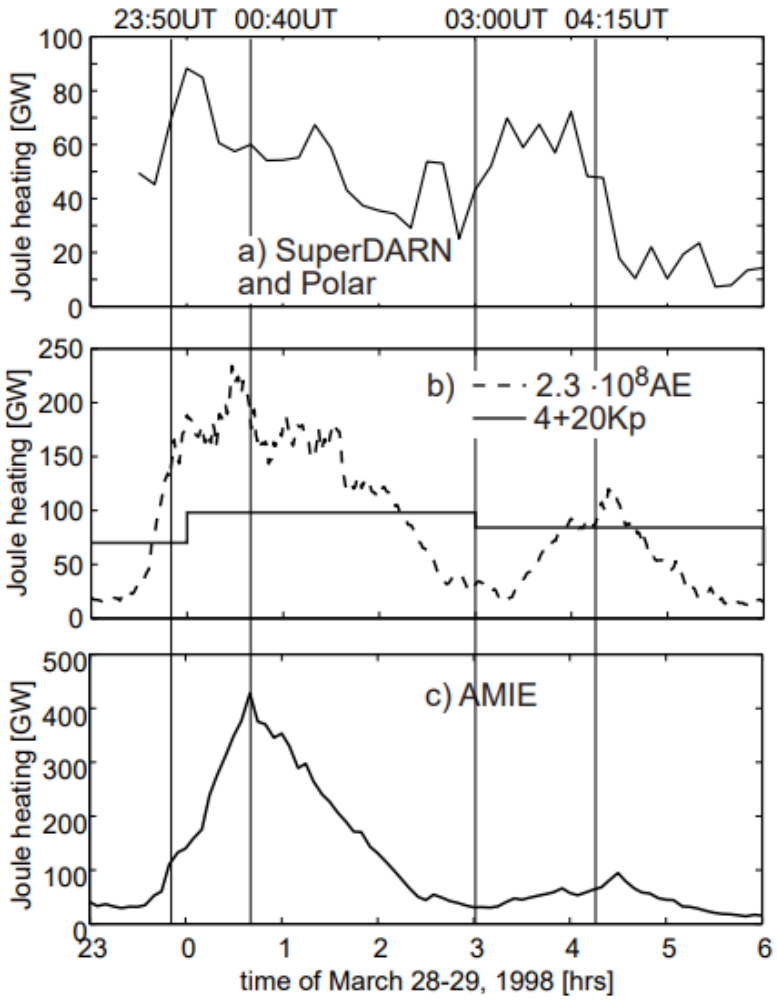

Figure 3.2: Joule heating estimated by SuperDARN and Polar measurements (top), AE- and Kp proxies (middle) and AMIE procedure (bottom). (Palmroth et al. 2005)

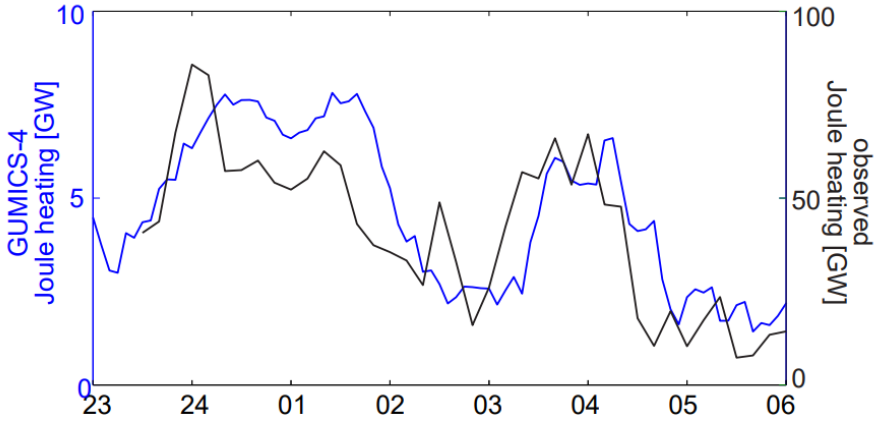

Figure 3.3: Joule heating simulated with GUMICS-4 (blue) and computed from electric fields measured by SuperDARN and of Pedersen conductance measured by Polar satellites (black). (Palmroth et al. 2005)

Palmroth et al. (2004) also revealed that the Joule heating simulations with the GUMICS-4 MHD model show less heating than the AMIE procedure. Another Joule heating simulation study is performed by Zhang et. al. (2005), where they put out with CEJH model, that is consistent with AMIE procedure, that the magnitude of interplanetary magnetic field and its direction, solar wind speed, geomagnetic activity indices such as AL, Kp and F10.7 are controlling the Joule heating, where the parameters such as solar wind density and Earth's dipole tilt does not have a remarkable effect. Kalafatoglu Oner & Kaymaz (2011) also compared three Joule heating calculation methods; AE proxy, SuperDARN radar observations, SWMF/BATS-R-US MHD model and revealed that the model results based on magnetosphere-ionosphere coupling gave good results of large scale global phenomena compared to observations. Another method developed is obtaining the Joule heating from Poynting flux ($S = E \times \delta B / \mu_0$), which the electric and magnetic field components are measured by the The Defense Meteorological Satellite Program (DMSP-15), since energy is dissipated where the Poynting flux is deposited (Rastaetter et. al., 2016). Rastaetter et. al. (2016) compared the Poynting flux in high latitudes and Joule heating from models (Physics-based and empirical) and found that SWMF/BATS-R-US (The Space Weather Modeling Framework/Block-Adaptive Tree-Solarwind Roe-type Upwind Scheme) magnetospheric MHD model has the lowest yield value (ratio of the modeled maximum to the observed maximum) and observes realistic electric potentials and physics-based models gave the similar patterns on a large scale. In a recent Joule heating analysis study performed by Younas

et. al. (2021) using the BATS-R-US model reveals that the CME, HSS and CME/HSS events show different ionospheric Joule heating patterns. The CME events show sharp and short duration of model Joule heating due to the large energy exchange related with long southward IMF turn, where the HSS and CME/HSS driven storms show long duration and less generation of model Joule heating; due to the short southward IMF turn (Younas et. al., 2021). Overall, in the light of this literature work with models, it is decided to use a physics-based model, SWMF/ BATS-R-US MHD model to obtain Joule heating in this study.

3.3 SWMF/BATS-R-US (with RCM) 3D Magnetohydrodynamics Model

The Space Weather Modeling Framework (SWMF) is a high-performance tool designed to couple models from different domains and to simulate space weather conditions and to make forecasts easier (Toth et. al. 2005). SWMF uses coupled models with MHD solvers. The physics-based domains from the Sun's surface to the surface of a planet are classified as: Solar Corona (SC), Eruptive Event Generator (EE), Inner Heliosphere (IH), Solar Energetic Particles (SP), Global Magnetosphere (GM), Inner Magnetosphere (IM), Radiation Belt (RB), Ionosphere Electrodynamics (IE) and Upper At-mosphere (UA) as it is shown in Figure 3.4. In this study, SWMF is used with the Global Magnetosphere (GM) module (version 20180525) which uses high-performance Block Adaptive Tree Solar-Wind Roe Upwind Scheme (BATS-R-US) code (Powell et al., 1999; Gombosi et al., 2003) to solve 3D magnetohydrodynamics (MHD) equations. Also the Inner Magnetosphere (IM) domain which is using Rice Convection Model (RCM) and Ionospheric Electrodynamics (IE) domain using Ridley Ionosphere Model (RIM) are coupled to the model in order to compute electric potentials and conductances from FACs. Inputs of BATS-R-US are solar wind density, temperature, 3D velocity and 3D magnetic field in GSM coordinates; where the outputs of GM are atomic mass unit density, pressure, velocity, magnetic field, electric currents and the outputs of IM are electric potential, Hall and Pedersen conductances (NASA, n.d.). In this study, Wind spacecraft data input was decided to be used within the model, since it was the only spacecraft in use with the least data gaps among the other options. The events in this study were simulated with 1,007,616 grid cells with simulation box size of -224 R_E downstream

and 32 R_E upstream boundaries and with the highest magnetospheric resolution as 0.25 R_E near Earth as it is seen from Figure 3.5.

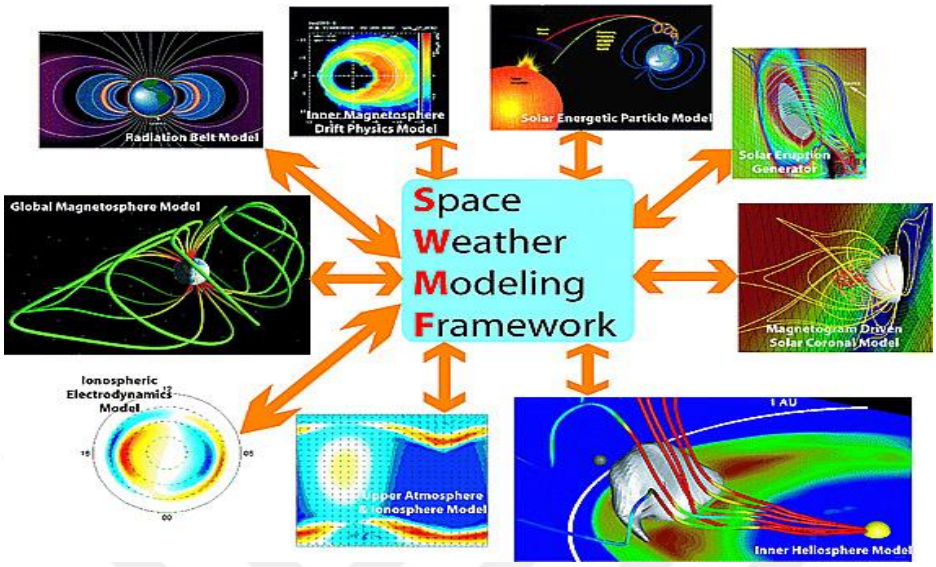

Figure 3.4: Nine domains of Space Weather Modeling Framework (SWMF). (Toth et. al. 2005)

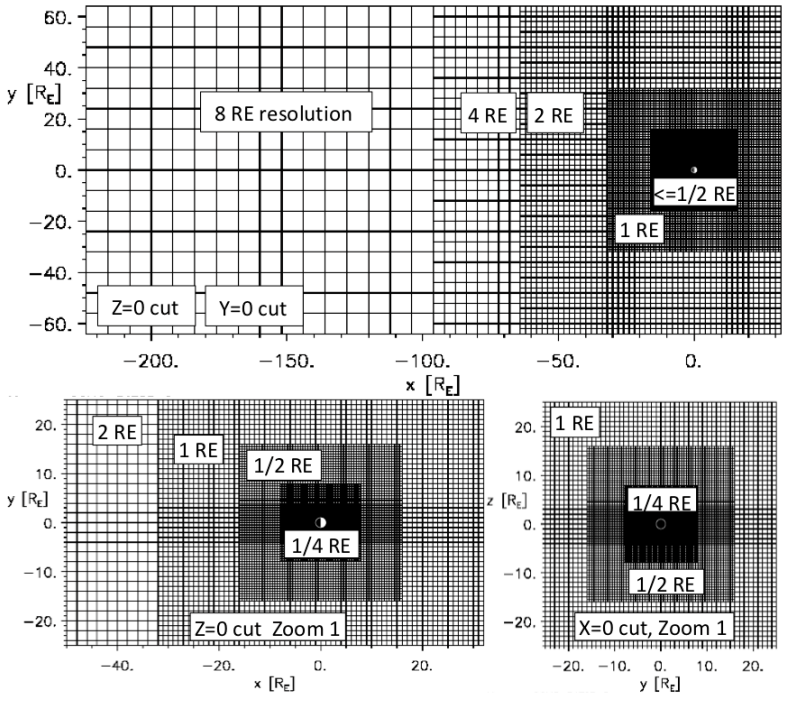

Figure 3.5: Simulation grids of BATS-R-US magnetospheric MHD model runs (NASA/CCMC, n.d.).

The constant value of interplanetary magnetic field in x direction (B_x) was set to zero. The ionospheric conductance model is set to auroral conductances generated by F10.7

solar irradiance and FACs. Dipole was not set to start time of the run. The model Model output frequency is also set to 240 seconds (4 min). The Joule dissipation of the model is derived from the height integrated total ionospheric current (J), Hall and Pedersen conductances (σ_H and σ_p) as it is shown in equation 3.8 (Kalafatoglu-Eyiguler et. al., 2018).

$$\int_{90\ \mathrm{km}}^{Z_{upper}} \frac{J(z)_{\perp}^{2}\sigma_P(z)}{(\sigma_P(z)+\sigma_H(z))^2}\,dz \ \ [\mathrm{GW}] \tag{3.8}$$

$$\int_{90\ \mathrm{km}}^{Z_{upper}} \frac{J(z)_{\perp}^{2}}{\sigma_c(z)}\,dz \ \ [\mathrm{GW}] \tag{3.9}$$

Here, $(\sigma_P + \sigma_H)^2/\sigma_p$ term represents the Cowling conductivity (σ_c), as it is explained in the previous section, which simplifies the equation 3.8 to equation 3.9. The runs for this study are requested remotely from Community Coordinated Modeling Center (CCMC) to obtain results and results are shown in the next chapters.

4. DATA, METHODOLOGY AND RESULTS

4.1 CME and HSS Case Selections

In order to perform this Joule heating analysis caused by coronal mass ejection (CME) and high speed solar wind stream (HSS) events, three CME and three HSS cases were identified as case studies using several methods in the light of the informations from sections 2.2, 2.3 and 2.4. From here and on, the three CME events will be referred as CME 1, CME 2 and CME 3 while the three HSS events will be referred as HSS 1, HSS 2 and HSS 3. To select the events, the most recently completed sunspot cycle "Solar Cycle 24" was decided as the interval to search for phenomena. The 24^{th} solar cycle started in December 2008 and it ended in December 2019. It is known that near solar minimum CIR/HSS events are dominating, while CME events are more frequent during the solar maximum years. Near the minimum of 24^{th} solar cycle, years from 2009 to 2011 was chosen as the interval to search for CIR/HSS events. On the other hand, time interval from 2012 to 2014 years were selected for CME events corresponding to the maximum years of the cycle. To select the case studies for CMEs and HSSs, the events were detected by using remote sensing methods such as imagers on board of spacecraft, then their motion towards the Earth was tracked through instruments on board of spacecraft between the Sun and Earth. Later, the detected events are justified by using published catalogues.

4.1.1 Remote sensing observations

The first and the fastest observation method of solar phenomena is remote sensing. This method works with monitoring the Sun non-stop to detect the abrupt changes. Remote sensing instruments on board of the satellites are coronagraphs and telescopes of imagers. In this study, SOHO/LASCO C2 coronagraph images were used to capture coronal mass ejection events. The C2 coronagraph captures images of the Sun from 1.5 to 6 R_{SUN} (Brueckner et. al., 1995). Figure 4.1, shows the images that were captured just after the eruption of CME 1, CME 2 and CME 3 events respectively on

the dates 14/06/2012 14:36 UT, 12/07/2012 17:12 UT and 15/03/2013 07:24 UT. On the images, the bright areas represent the erupted material from the Sun's corona.

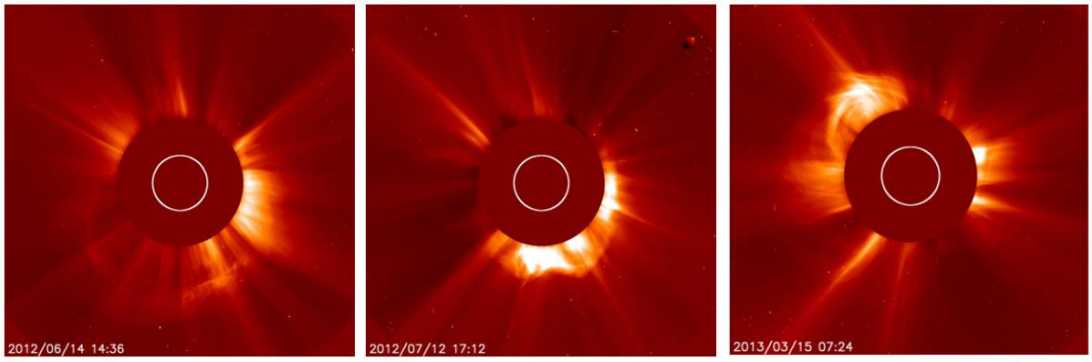

Figure 4.1: Three different Earth- directed coronal mass ejections observed by SOHO/LASCO C2 coronagraph. From left to right it represents CME 1, CME 2, CME 3 events.

Besides this, EUV images taken from SDO/AIA were used to detect coronal holes, which are the origin of high speed solar wind streams. Since coronal holes are easily tracked in the 193 Å wavelength, it was decided to use this channel for this study. Figure 4.2 represents the coronal hole images taken from SDO/AIA's 193 Å channel for HSS 1, HSS 2 and HSS 3 respectively on 02/05/2010 23:45 UT, 06/01/2011 00:19 UT and 10/04/2011 09:28 UT.

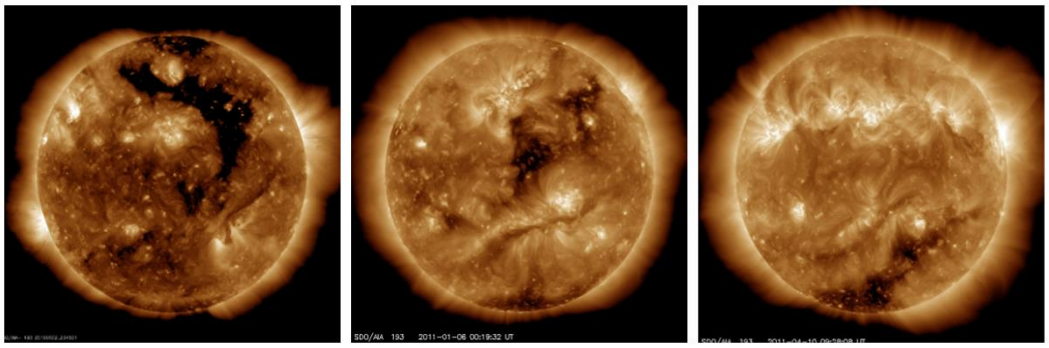

Figure 4.2: Three different coronal hole images observed by SDO/AIA 193 Å channel telescope. From left to right it represents HSS 1, HSS 2, HSS 3 events.

All of the images of the coronal holes, the dark regions with various shapes, shown in Figure 4.2 are Earth-directed and they represent the origins of high speed solar wind streams. They originated around the poles, which means it is long lasting compared to other regions on the Sun's surface and more intense.

4.1.2 In situ measurements

As the solar activity is detected by using on board imagers that are observing the Sun, the next step is to detect the changes and disturbances of the background solar wind using L1 point spacecrafts located between the Sun and Earth. The L1 spacecraft instruments measure the solar wind plasma quantities such as speed, magnetic field and density. In this study, for all the CME and HSS cases WIND spacecraft at L1 Lagrange point was selected as the solar wind observing spacecraft that measures the energetic particles before they arrive to Earth's magnetosphere. Magnetic Field Investigation (MFI) and the Solar Wind Experiment (SWE) instruments on board WIND are used to measure magnetic field directions and magnitudes, and solar wind density, temperature, and speed. For all vector quantities GSM (Geocentric Solar Magnetospheric) coordinate system were used. Dynamic pressure is a derived quantity using solar wind speed and density and provided together with the WIND data. MFI and SWE data were extracted from NASA/GSFC's CDAWeb service. Plasma beta was extracted from NASA/GSFC's OMNI data set through OMNIWeb. The data resolutions for the MFI instrument and OMNI are 1-min, while for SWE it is around 1-3 min. Figures 4.3, 4.5 and 4.7 show the solar wind plasma and magnetic field parameters measured by WIND instruments respectively corresponding to CME 1, CME 2 and CME 3 cases. All the data are plotted using MATLAB. CME presence from in-situ measurements are generally detected by the sudden jump in all solar wind plasma and magnetic field parameters at the same time. All the CME related figures show similar pattern; abrupt increases of the solar wind velocity, proton density, dynamic pressure, temperature and magnetic field at the same time (the jump was marked with a solid dark red line). Another way to detect solar activity is to measure its effects on Earth by observing the geomagnetic disturbances on the ground level, in other words by using geomagnetic activity indices. In this study, AE, Dst and Kp indices were used as the geomagnetic activity indicators and were obtained from World Data Center for Geomagnetism, Kyoto. The data resolution for AE is 1-min, for Dst it is 1-hr and for Kp it is 3-hr. Figures 4.4, 4.6 and 4.8 represent the Dst index corresponding to CME 1, CME 2 and CME 3 cases respectively. Again the CME related Dst figures show the same pattern; Dst minimum value less than -100 nT, indicating major geomagnetic storms according to the geomagnetic storm classification performed by Loewe & Prölss (1997). Then, the same set of plots were

created also for HSS 1, HSS 2 and HSS 3 cases respectively and shown in Figures 4.9, 4.10, 4.11, 4.12, 4.13 and 4.14.

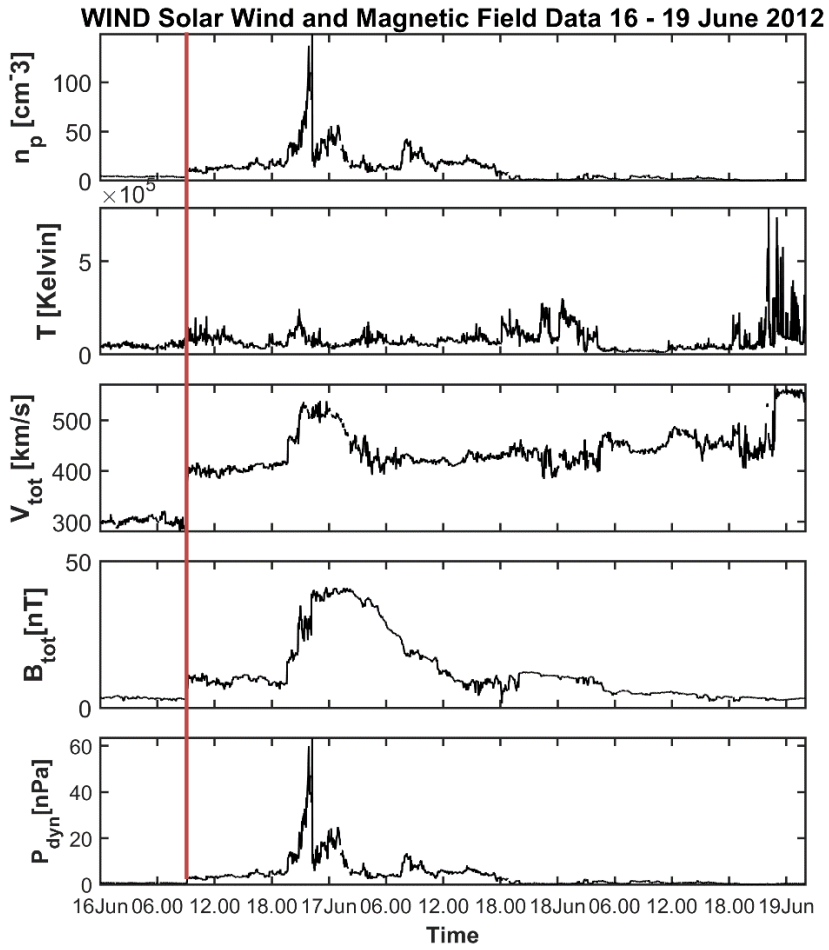

Figure 4.3: WIND solar wind plasma and magnetic field data for 16-19 June 2012, corresponding to CME 1 event. The parameters from top to bottom are proton density, temperature, solar wind speed, interplanetary magnetic field strength and dynamic pressure.

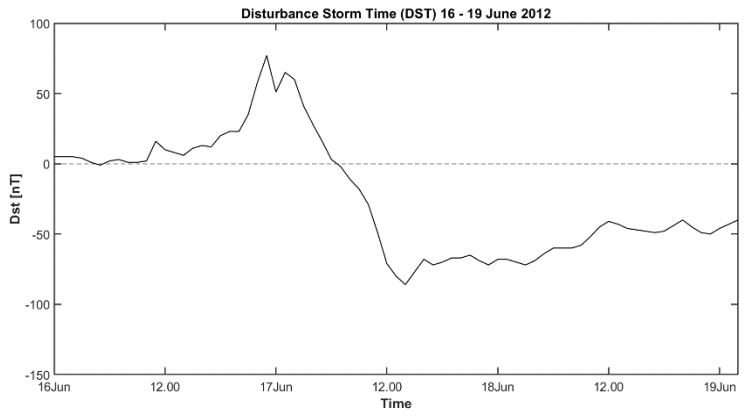

Figure 4.4: Kyoto disturbance storm time (Dst) index data for 16-19 June 2012, corresponding to CME 1 event.

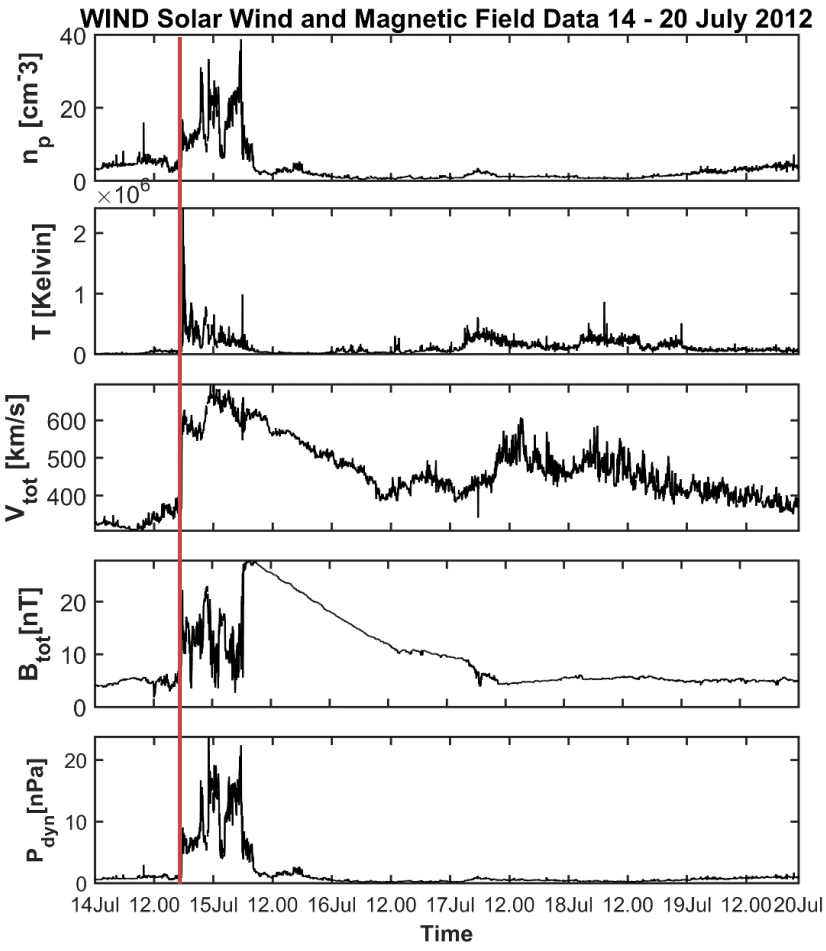

Figure 4.5: WIND solar wind plasma and magnetic field data for 14-20 July 2012, corresponding to CME 2 event. The parameters from top to bottom are proton density, temperature, solar wind speed, interplanetary magnetic field strength and dynamic pressure.

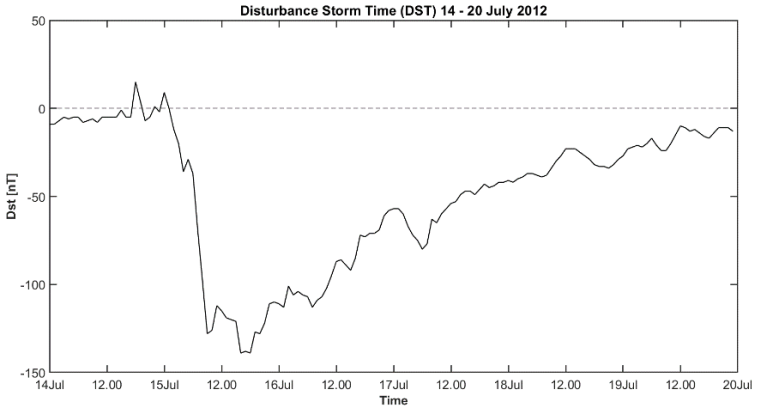

Figure 4.6: Kyoto disturbance storm time (Dst) index data for 14-20 July 2012, corresponding to CME 2 event.

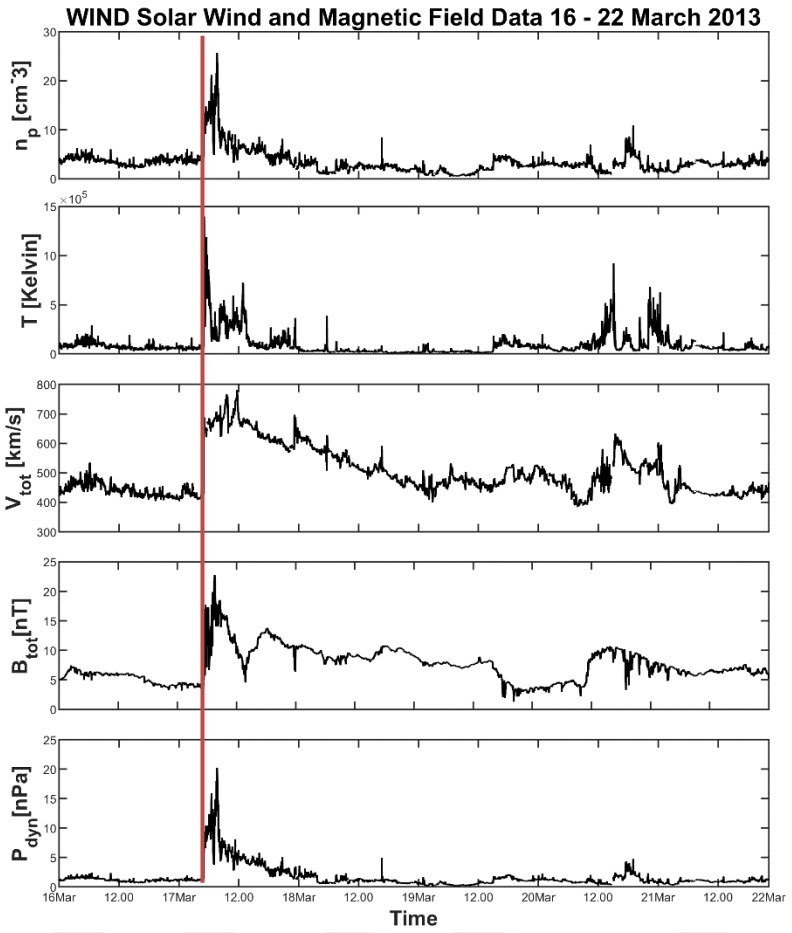

Figure 4.7: WIND solar wind plasma and magnetic field data for 16-22 March 2013, corresponding to CME 3 event. The parameters from top to bottom are proton density, temperature, solar wind speed, interplanetary magnetic field strength and dynamic pressure.

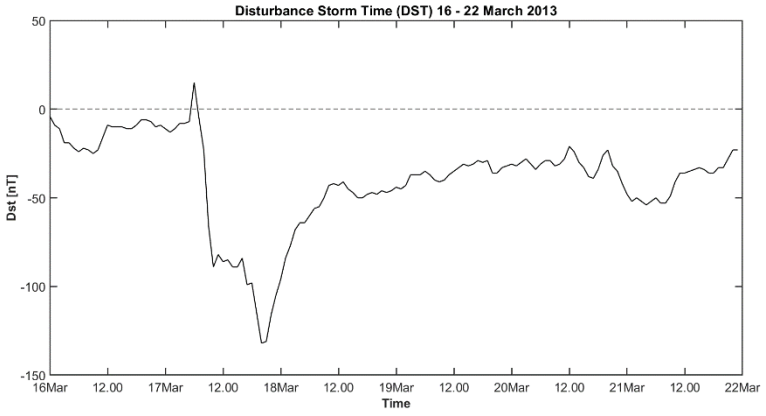

Figure 4.8: Kyoto disturbance storm time (Dst) index data for 16-22 March 2013, corresponding to CME 3 event.

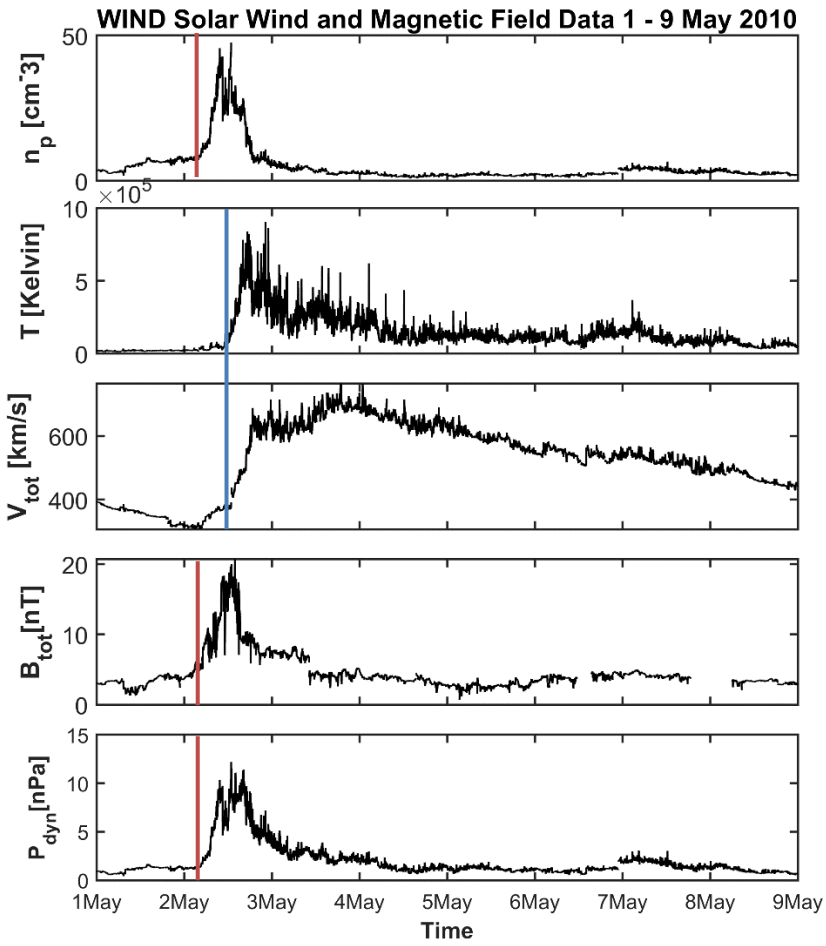

Figure 4.9: WIND solar wind plasma and magnetic field data for 1-9 May 2010, corresponding to HSS 1 event. The parameters from top to bottom are proton density, temperature, solar wind speed, interplanetary magnetic field strength and dynamic pressure.

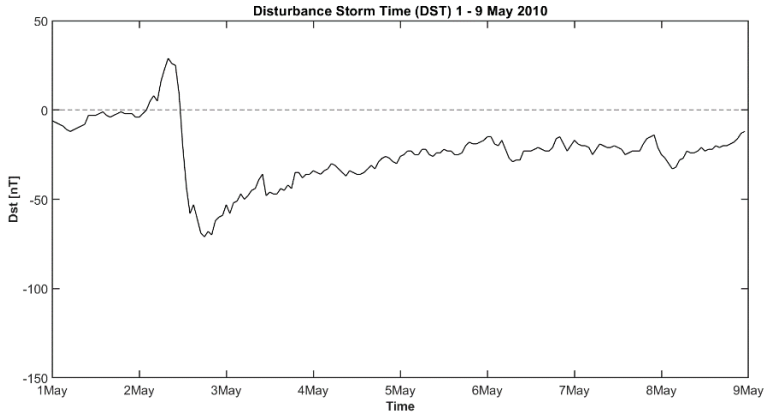

Figure 4.10: Kyoto disturbance storm time (Dst) index data for 1-9 May 2010, corresponding to HSS 1 event.

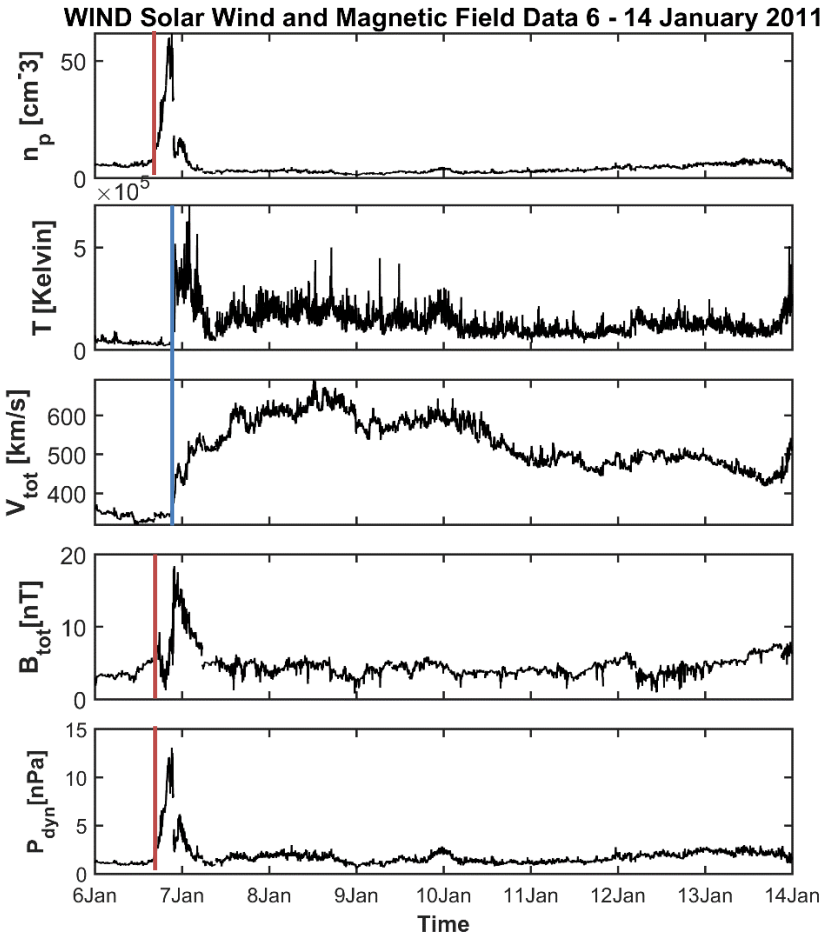

Figure 4.11: WIND solar wind plasma and magnetic field data for 6-14 January 2011, corresponding to HSS 2 event. The parameters from top to bottom are proton density, temperature, solar wind speed, interplanetary magnetic field strength and dynamic pressure.

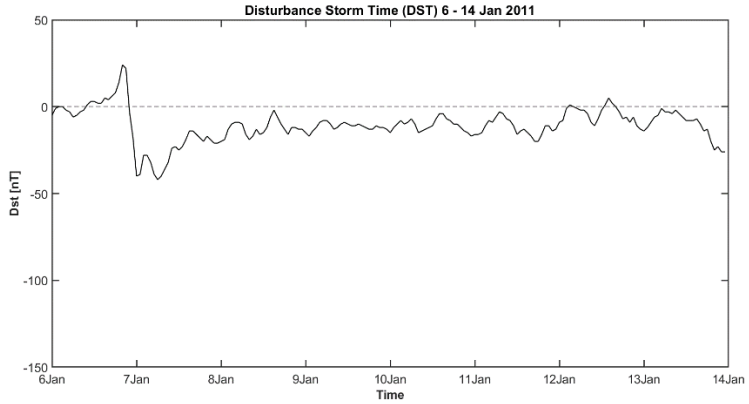

Figure 4.12: Kyoto disturbance storm time (Dst) index data for 6-14 January 2011, corresponding to HSS 2 event.

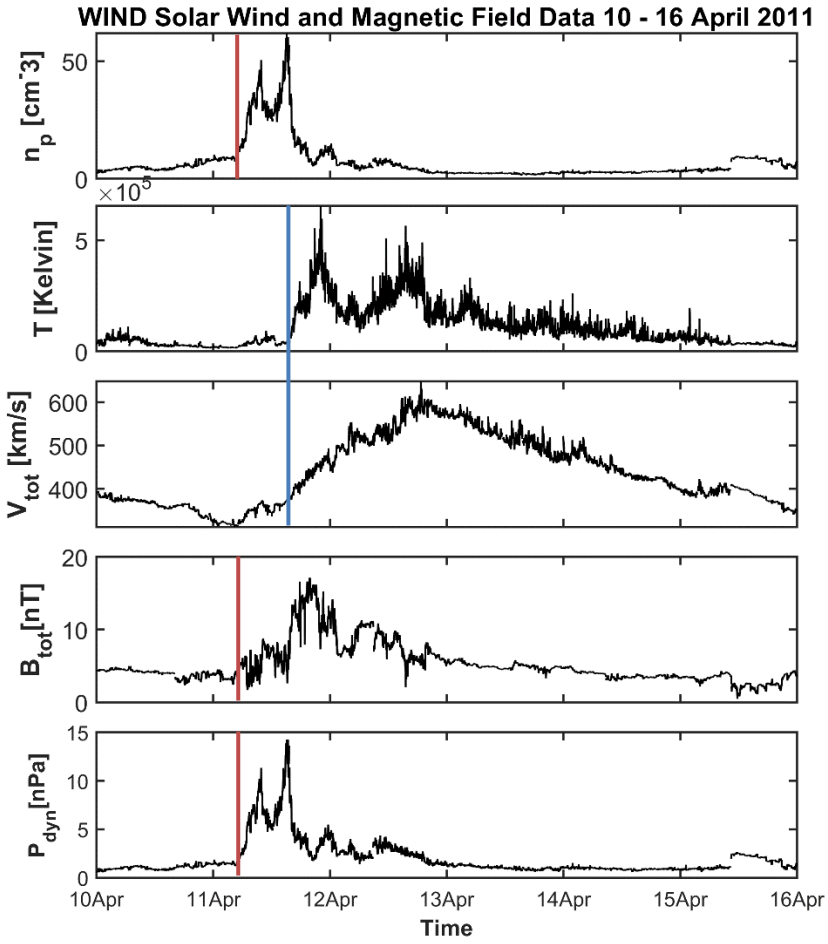

Figure 4.13: WIND solar wind plasma and magnetic field data for 10-16 April 2011, corresponding to HSS 3 event. The parameters from top to bottom are proton density, temperature, solar wind speed, interplanetary magnetic field strength and dynamic pressure.

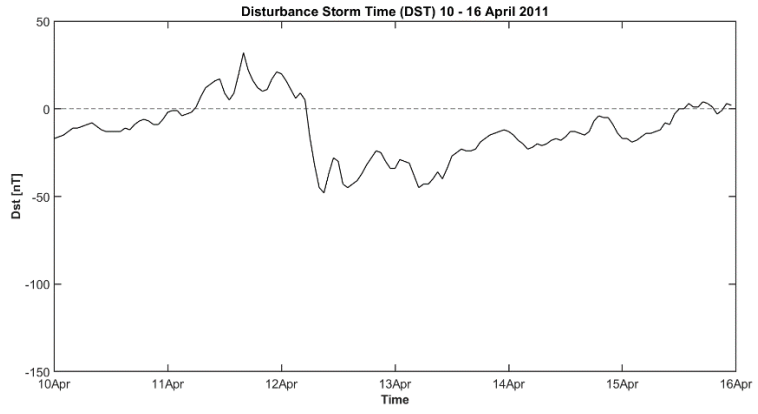

Figure 4.14: Kyoto disturbance storm time (Dst) index data for 10-16 April 2011, corresponding to HSS 3 event.

From Figures 4.9, 4.11 and 4.13, it can be clearly seen that the solar wind plasma and magnetic field data showed a similar pattern; the increase in magnetic field strength, density and dynamic pressure is seen earlier (marked with dark red solid line) than speed and temperature parameters (marked with blue solid line). Also, the decrease after the local speed and temperature maxima was observed steady and slow, rather than an abrupt drop as in CME cases. Another important difference is that the density and solar wind speed observations were relatively higher in all HSS cases compared to CME cases. Again, the HSS related Dst figures show a similar pattern; Dst minimum values less than -100 nT were not observed, meaning the HSS events did not cause any major geomagnetic storms, differently from CME cases. In addition to these in-situ measurements from WIND spacecraft, also catalogues were used to justify the events.

4.1.3 Catalogues

SOHO/LASCO CME Catalogue (Gopalswamy et. al., 2009) was used to justify CME events. This CME catalog is generated and maintained at the CDAW Data Center by NASA and The Catholic University of America in cooperation with the Naval Research Laboratory. SOHO is a project of international cooperation between ESA and NASA. SOHO/LASCO CME Catalogue had specified the eruption time of the three CME events for CME 1, CME 2 and CME 3 respectively as 14/06/2012 14:12 UT, 12/07/2012 16:48 UT and 15/03/2013 07:12 UT. All of the CME events were marked as Halo CMEs with 360° angular width. The CME linear speeds were detected as 987 km/s, 885 km/s and 1063 km/s respectively. For the model runs, the intervals of CMEs are determined, approximately covering the time interval when the disturbances start from the quiet solar wind background until the disturbances return to background levels. 16/06/2012 00:00 UT to 19/06/2012 02:00 UT for CME 1, 14/07/2012 00:00 to 20/07/2012 00:00 UT for CME 2 and 16/03/2013 00:00 UT to 22/03/2013 UT for CME 3 cases were selected as the intervals covering the phenomena. The catalogue that was used to justify HSS events is HELIO4CAST SIR CATALOGUE v1.0, where the HSS 1 interval is specified as 05/02/2010 02:00 UT to 05/08/2010 19:00 UT, HSS 2 interval from 01/06/2011 15:00 UT to 01/13/2011 13:00 UT and HSS 3 interval from 04/11/2011 04:00 UT to 04/14/2011 to 11:00 UT by using the in-situ measurements of WIND spacecraft. In this study, it was decided to use these intervals to run the magnetospheric MHD model provided by SWMF.

4.2 Joule Heating from Magnetospheric MHD Model

As it was explained in the previous sections, SWMF is decided to use with the GM module that is using BATS-R-US code to solve 3D MHD equations. The model was run with version 20180525 including RCM as the IM module and also IE module coupled to the model to obtain ionospheric dissipation rates. For the model input, the intervals specified in Section 4.2 were used with WIND data input. Also, solar wind magnetic field in x-direction is specified as zero and all the events (CME 1, CME 2, CME 3 and HSS 1, HSS 2, HSS 3) were simulated with 1,007,616 grid cells resolution of the magnetosphere. The conductances used to obtain the Joule dissipation were set as Auroral conductances driven by solar irradiance and FACs. Also, the dipole was updated throughout the model run interval. Model output frequency was also set to 240 s (4 min). It should be noted that the model runs are not applicable for the event intervals covering more than 168 hours. Also, the input data gaps affect the model runs. For the HSS 1 and HSS 2 runs, there is data gaps and the durations are longer than 168 hours and the ionospheric dissipation output resulted with unphysical values after these gaps or interval limit exceedings. Where the bow shock expands and crosses the sunward boundary (at x=32 R_E) it coincides with the times of the unphysical values. So, these unphysical values are extracted from the data interval for performing more accurate statistical analysis. Figures 4.15, 4.16, 4.17, 4.18, 4.19 and 4.20 show the Joule heating obtained from SWMF/BATS-R-US model for CME 1, CME 2, CME 3, HSS 1, HSS 2 and HSS 3 cases respectively.

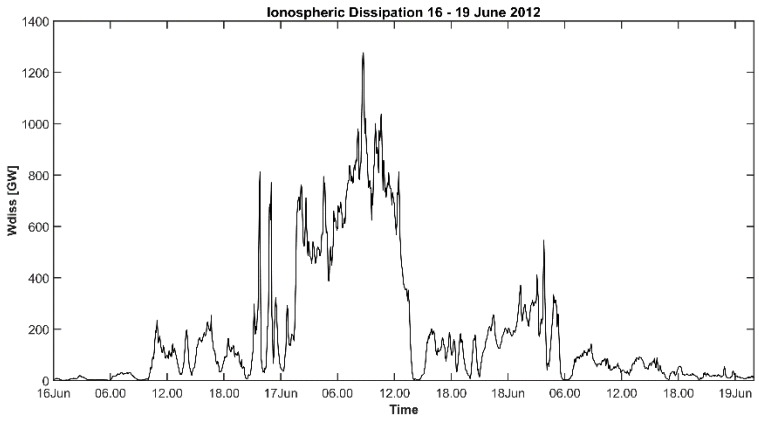

Figure 4.15: SWMF/BATS-R-US with RCM model output for ionospheric dissipation for 16-19 June 2012, corresponding to CME 1 event.

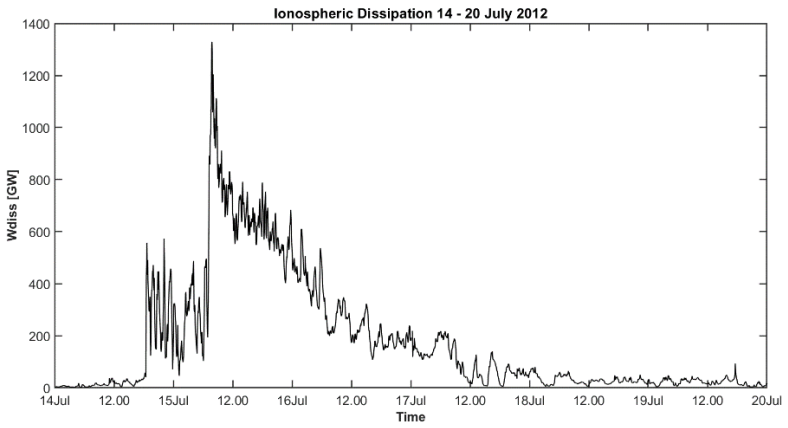

Figure 4.16: SWMF/BATS-R-US with RCM model output for ionospheric dissipation for 14-20 July 2012, corresponding to CME 2 event.

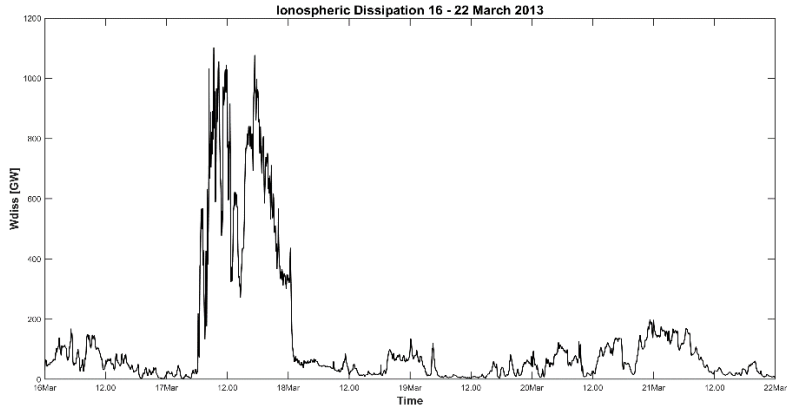

Figure 4.17: SWMF/BATS-R-US with RCM model output for ionospheric dissipation for 16-22 March 2013, corresponding to CME 3 event.

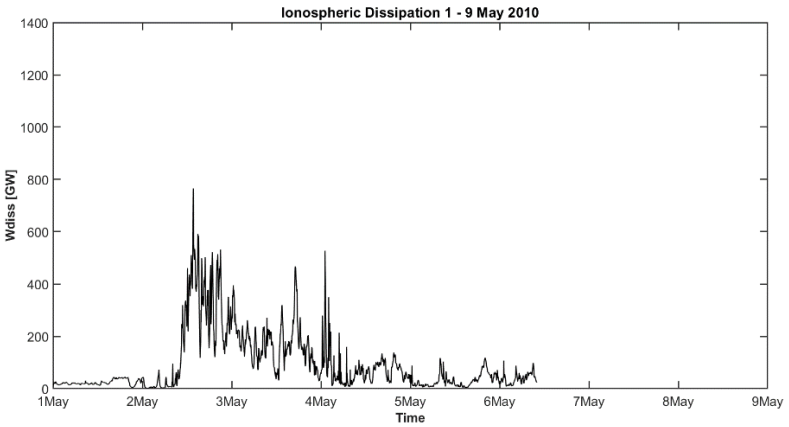

Figure 4.18: SWMF/BATS-R-US with RCM model output for ionospheric dissipation for 1-9 May 2010, corresponding to HSS 1 event.

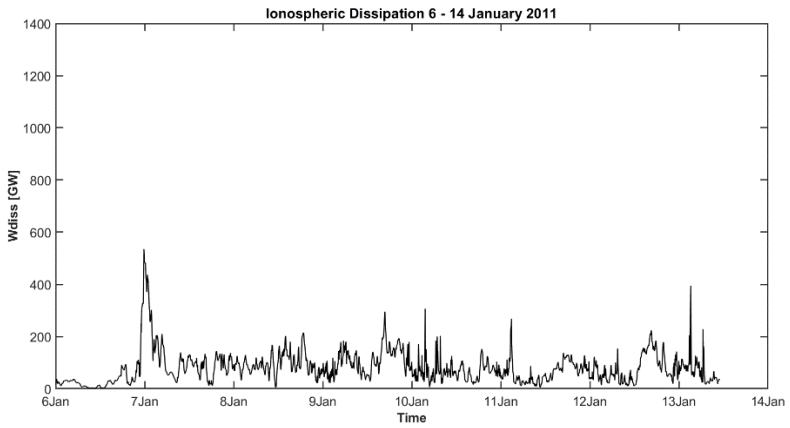

Figure 4.19: SWMF/BATS-R-US with RCM model output for ionospheric dissipation for 6-14 January 2011, corresponding to HSS 2 event.

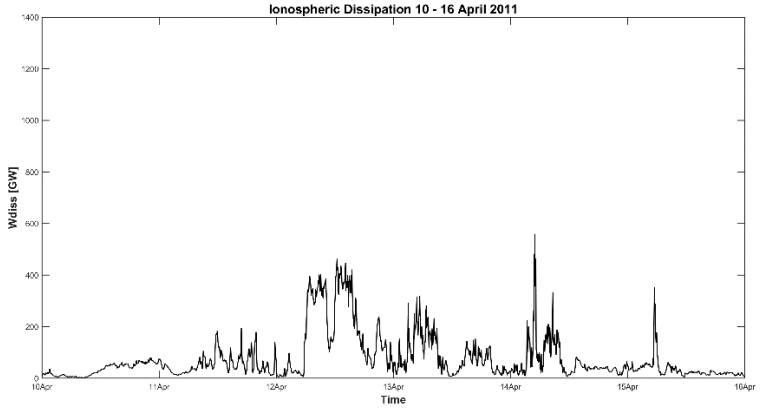

Figure 4.20: SWMF/BATS-R-US with RCM model output for ionospheric dissipation for 10-16 April 2011, corresponding to HSS 3 event.

The figures show a higher Joule heating (JH) rate for all of the CME cases reaching 1400 GW, whereas it shows only around 800 GW for HSS cases. Also, it is clear that the JH rate for CMEs for all cases end with an abrupt decrease, while for the HSS cases it fluctuates and continues for a few days longer before reaching the background levels. The reason behind these differences could refer to the controlling parameter of Joule heating of the ionosphere. This controlling parameter can be either the solar wind parameter (the structure of the phenomena) or the magnetospheric processes (the driven geomagnetic storms). Figures 4.21, 4.22, 4.23, 4.24, 4.25 and 4.26 show the solar wind plasma, geomagnetic activity and Joule heating parameters together.

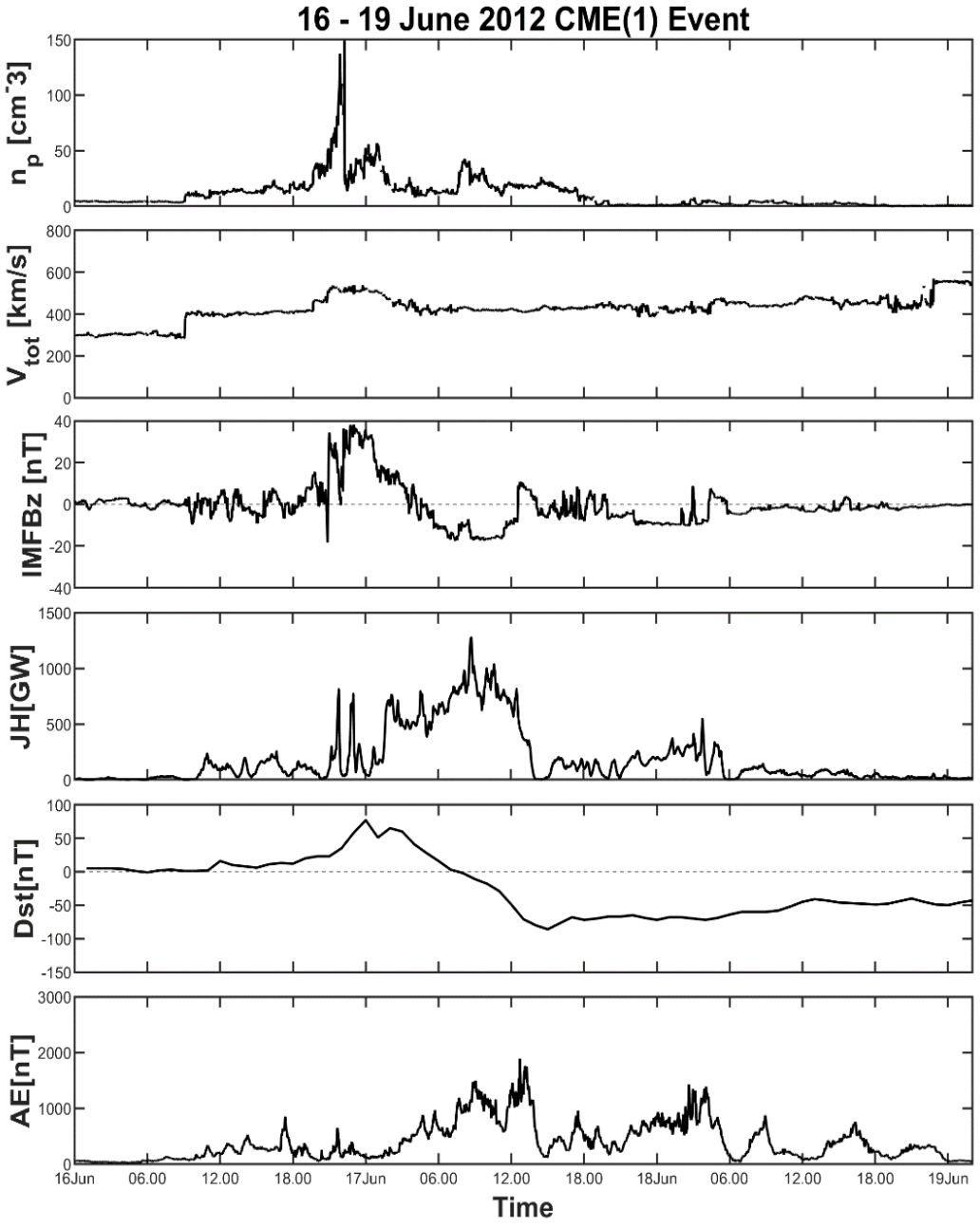

Figure 4.21: Solar wind, Joule heating and geomagnetic activity data plot for CME 1. The parameters from top to bottom are solar wind proton density, solar wind speed, z component of interplanetary magnetic field, Joule heating obtained from the model, disturbance storm time index (Dst) and AE index respectively.

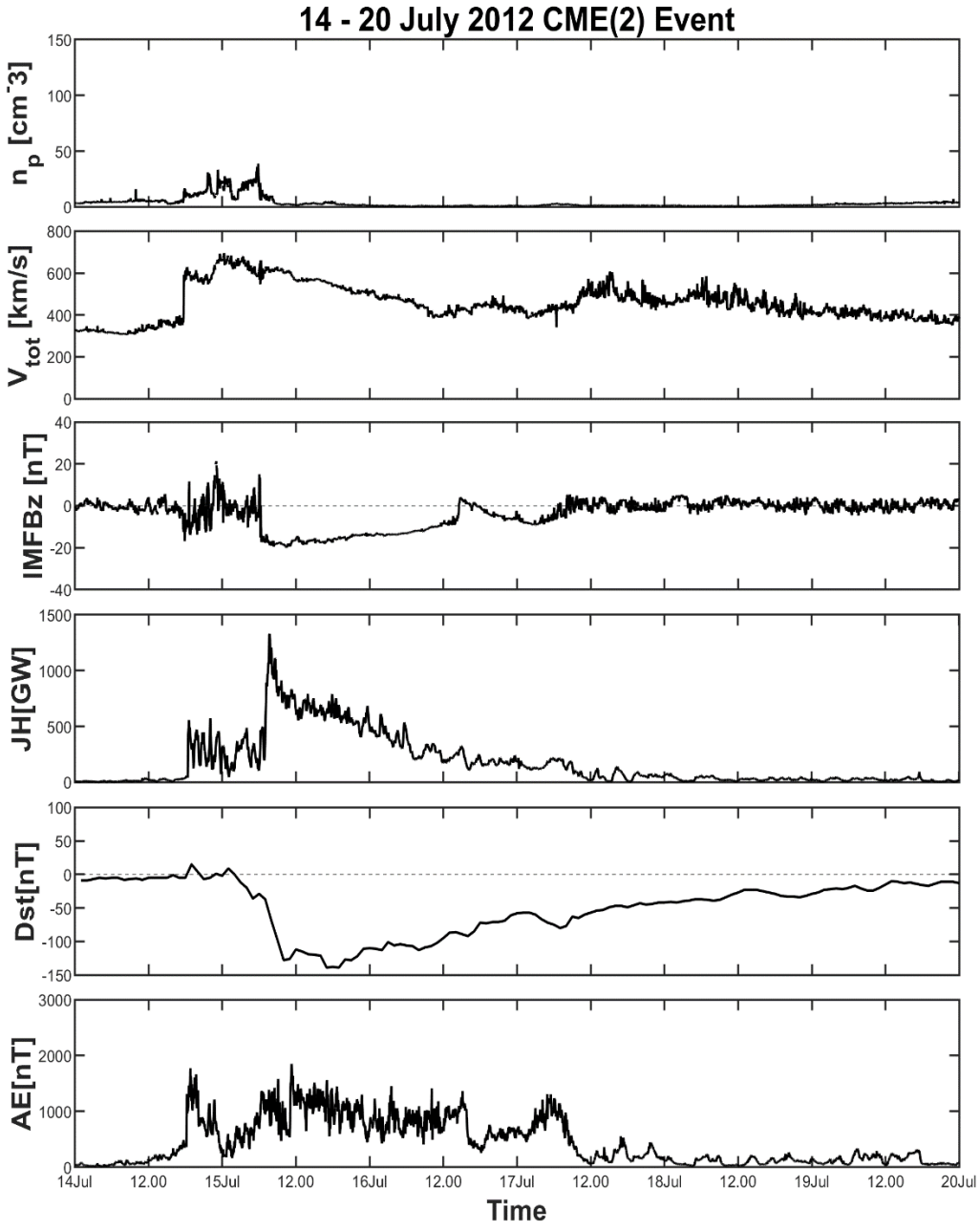

Figure 4.22: Solar wind, Joule heating and geomagnetic activity data plot for CME 2. The parameters from top to bottom are solar wind proton density, solar wind speed, z component of interplanetary magnetic field, Joule heating obtained from the model, disturbance storm time index (Dst) and AE index respectively.

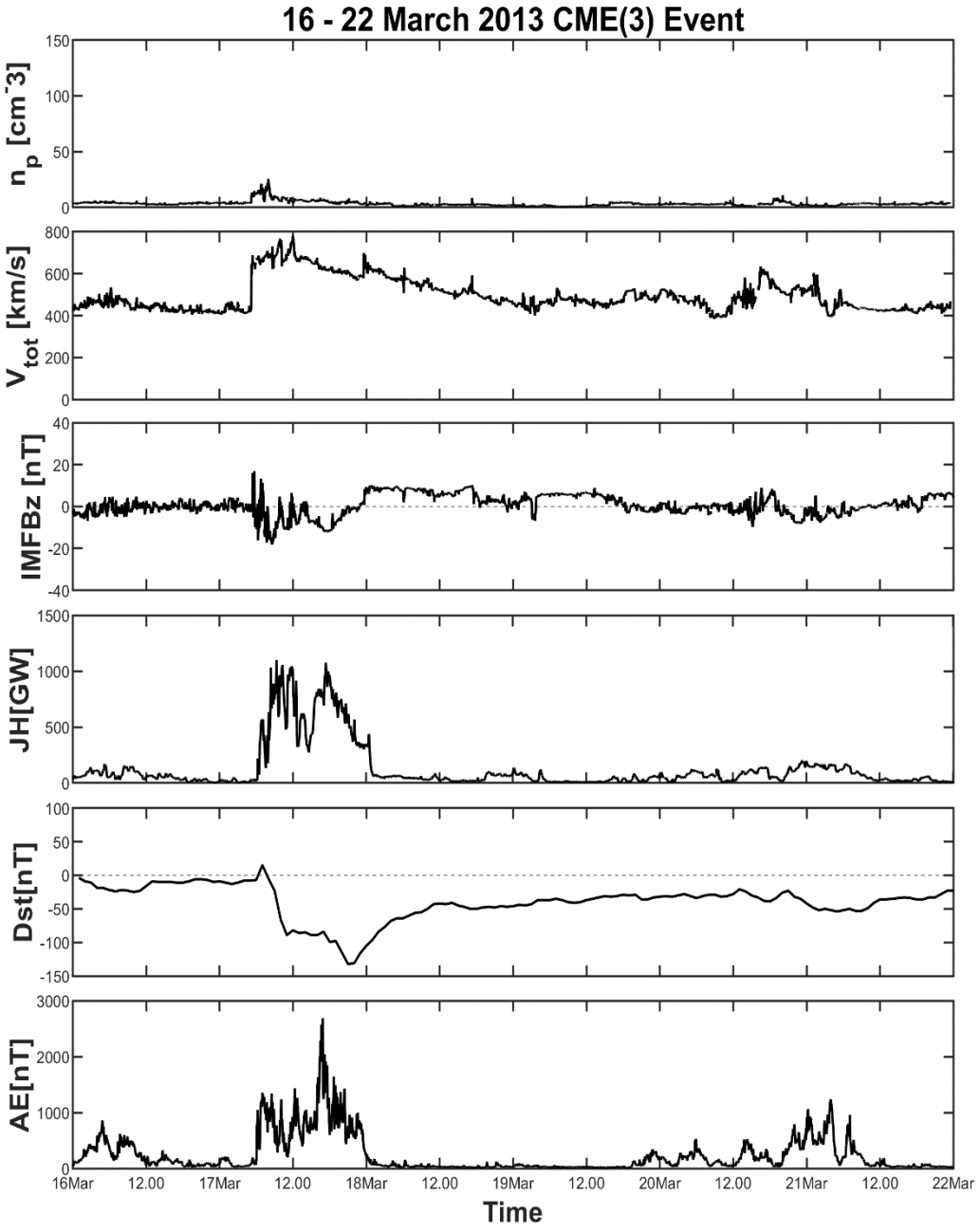

Figure 4.23: Solar wind, Joule heating and geomagnetic activity data plot for CME 3. The parameters from top to bottom are solar wind proton density, solar wind speed, z component of interplanetary magnetic field, Joule heating obtained from the model, disturbance storm time index (Dst) and AE index respectively.

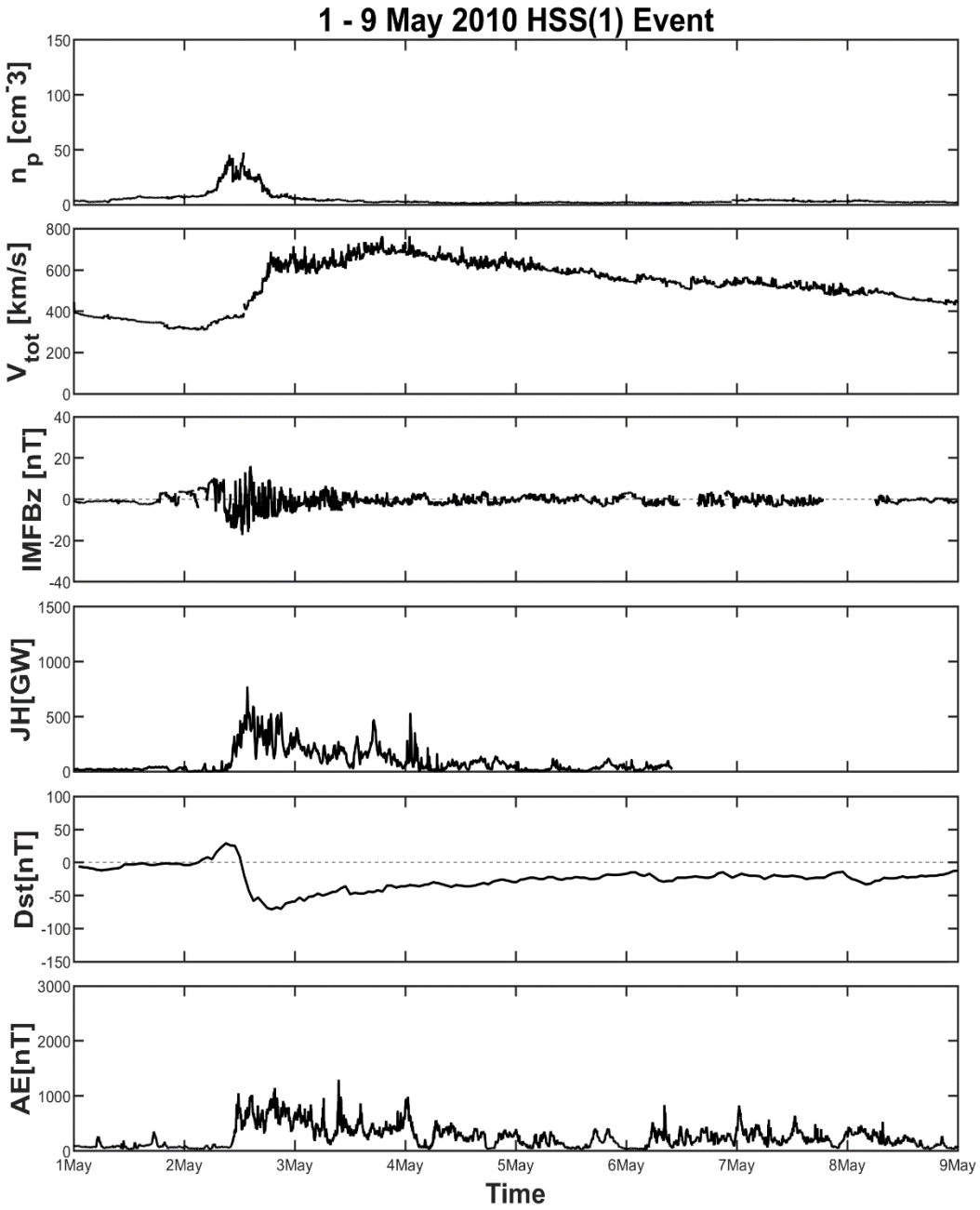

Figure 4.24: Solar wind, Joule heating and geomagnetic activity data plot for HSS 1. The parameters from top to bottom are solar wind proton density, solar wind speed, z component of interplanetary magnetic field, Joule heating obtained from the model, disturbance storm time index (Dst) and AE index respectively.

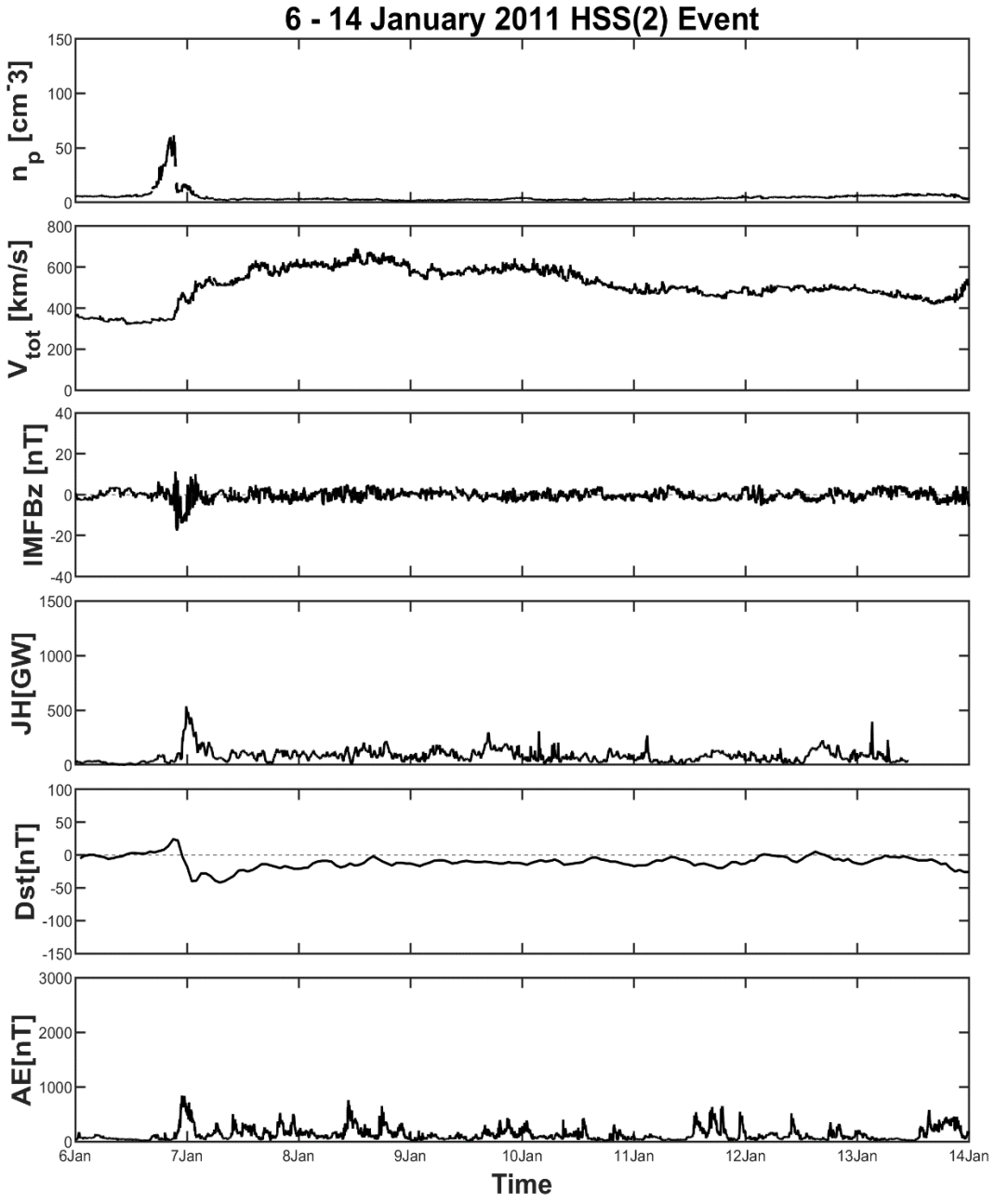

Figure 4.25: Solar wind, Joule heating and geomagnetic activity data plot for HSS 2. The parameters from top to bottom are solar wind proton density, solar wind speed, z component of interplanetary magnetic field, Joule heating obtained from the model, disturbance storm time index (Dst) and AE index respectively.

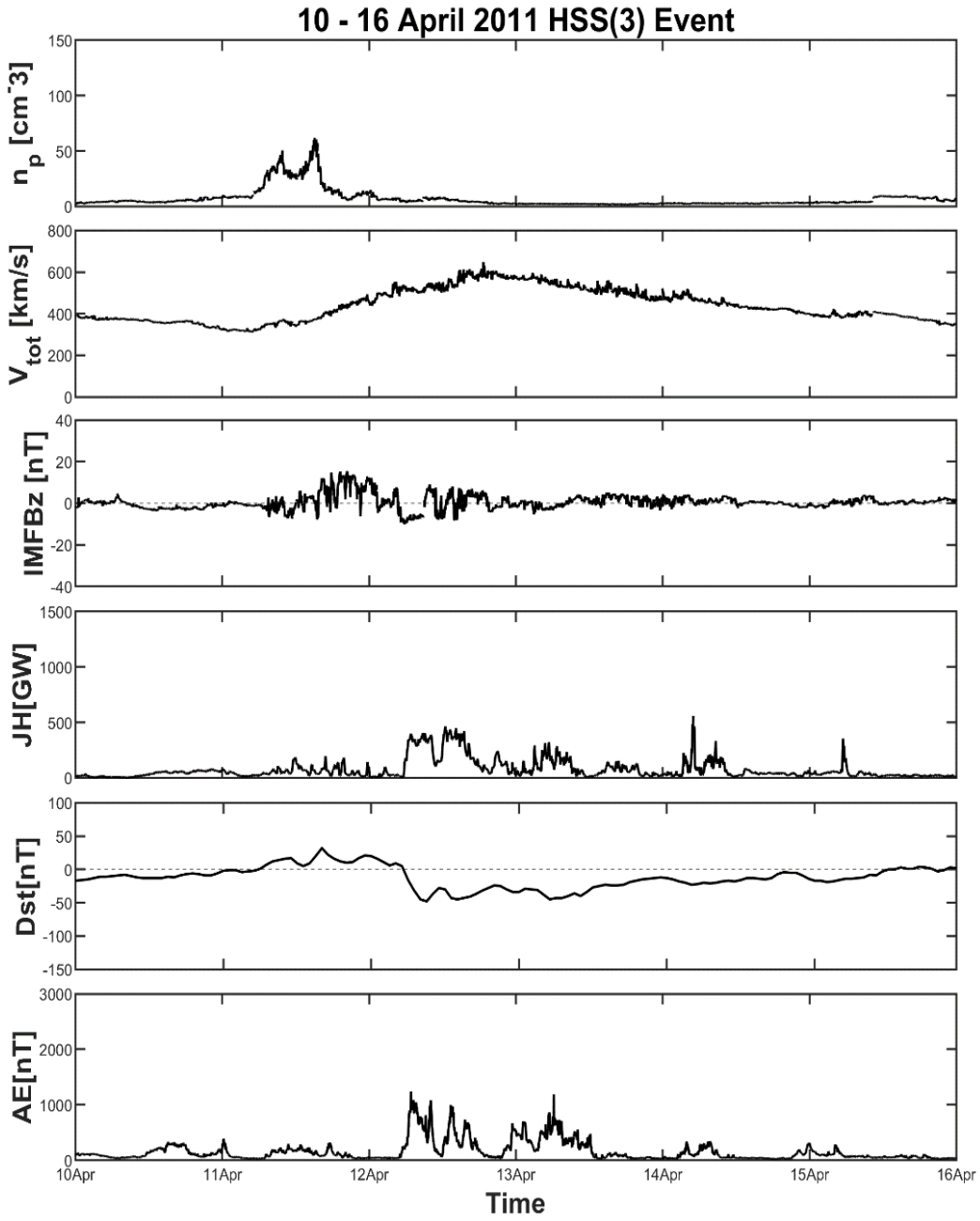

Figure 4.26: Solar wind, Joule heating and geomagnetic activity data plot for HSS 3. The parameters from top to bottom are solar wind proton density, solar wind speed, z component of interplanetary magnetic field, Joule heating obtained from the model, disturbance storm time index (Dst) and AE index respectively.

In general the figures show that the solar wind parameters have the disturbance just before the following increase in the Joule heating and with the disturbances in geomagnetic activity. That explains the solar wind-magnetosphere-ionosphere dynamo well. The solar wind kinetic energy is dissipated into the magnetosphere-ionosphere system in the form of Joule heating. To perform more detailed analysis and to explain the controlling parameters; firstly Joule heating for CME and HSS cases will be investigated structurally and secondly the heating will be investigated for the corresponding geomagnetic storms and phases of the phenomena. After the structural/driven geomagnetic storm comparisons are completed, simple and multi-linear regression analysis will be performed to obtain derived empirical relations with the solar wind/geomagnetic activity parameters that might be important for the further studies about prediction models.

4.3 ICME and CIR/HSS Structural Analysis with Joule Heating

The structures of both phenomena in the interplanetary space were already explained in detail in the previous sections. In this section, the structural intervals of both phenomena will be determined, and the corresponding Joule heating rates within the intervals will be calculated. As it is known, ICMEs generally have a structure consisting of three regions: a fast forward shock, sheath (SH) and also magnetic obstacle (MO-which is referring to the magnetic cloud for all cases in this study). Due to this different structure of the ICMEs, it is expected to observe different Joule heating rates corresponding to each region. And these differences are expected to be obtained due to the solar wind parameters as the drivers of Joule heating. The structural intervals from the interplanetary coronal mass ejection (ICME) consisting of sheath (SH) and magnetic obstacle (MO) regions were obtained from Wind ICME Catalogue **(**Nieves-Chinchilla et. al., 2018). The SH region of CME 1 is starting from 06/16/2012 09:03 UT to 06/16/2012 22:01 UT and the following MO region ends at 06/17/2012 11:23 UT. The SH region of CME 2 is starting from 07/14/2012 17:39 UT to 07/15/2012 06:14 UT and the following MO region ends at 2012 07/17 03:21 UT. The SH region of CME 3 is starting from 2013 03/17/2013 05:21 UT to 03/17/2013 14:09 UT and the following MO region ends at 03/19/2013 16:04 UT. The CIR/HSSs refer to just one

interval consisting of high speed solar wind with strong magnetic field. For the CIR/HSS interval, the corresponding Joule heating rate will be also calculated. The structural interval of HSSs were determined from the HELIO4CAST SIR CATALOGUE v1.0, where the HSS 1 interval had specified as 05/02/2010 02:00 UT to 05/08/2010 19:00 UT, HSS 2 interval from 01/06/2011 15:00 UT to 01/13/2011 13:00 UT and HSS 3 interval from 04/11/2011 04:00 UT to 04/14/2011 to 11:00 UT. Figures 4.27, 4.28 and 4.29 show the ICME intervals as it starts with a fast forward shock (marked with red dotted line) followed by the sheath region colored in light orange and magnetic obstacle region colored in lilac. Figures 4.30, 4.31 and 4.32 show the CIR/HSS intervals colored in light blue. The parameters from top to bottom are solar wind proton density, solar wind speed, z component of interplanetary magnetic field, Joule heating obtained from the model, disturbance storm time index (Dst) and AE index respectively.

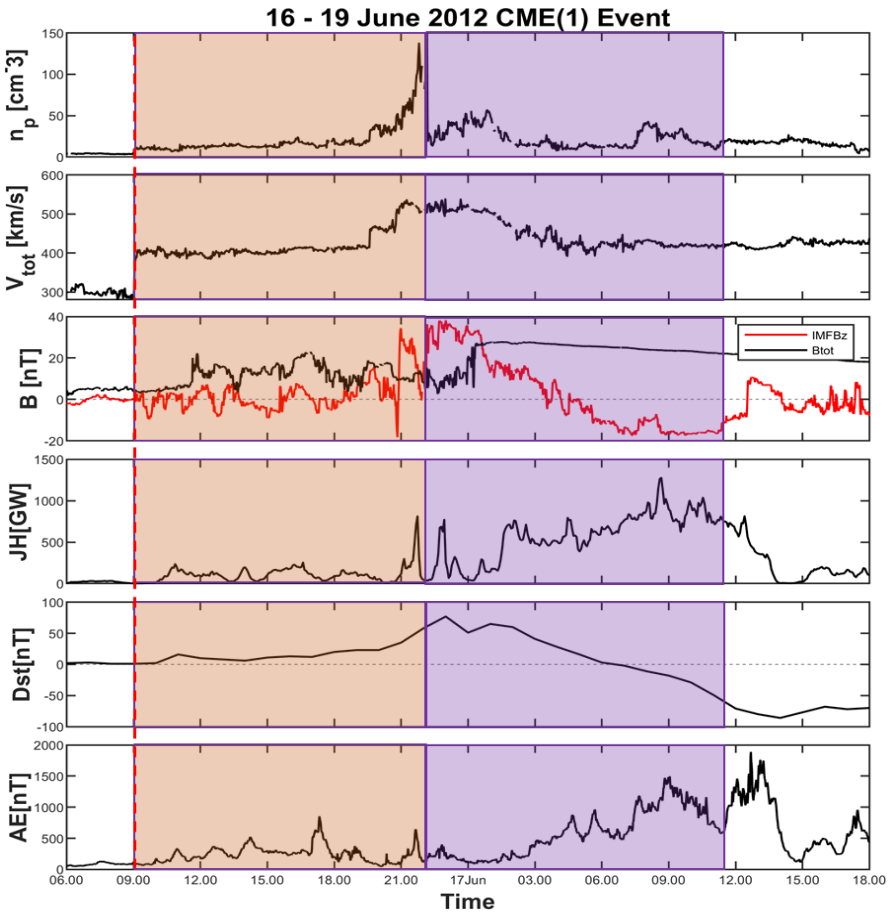

Figure 4.27: Solar wind, Joule heating and geomagnetic activity plots showing the shock (red dotted line), sheath (light orange) and magnetic obstacle (lilac) regions of CME 1.

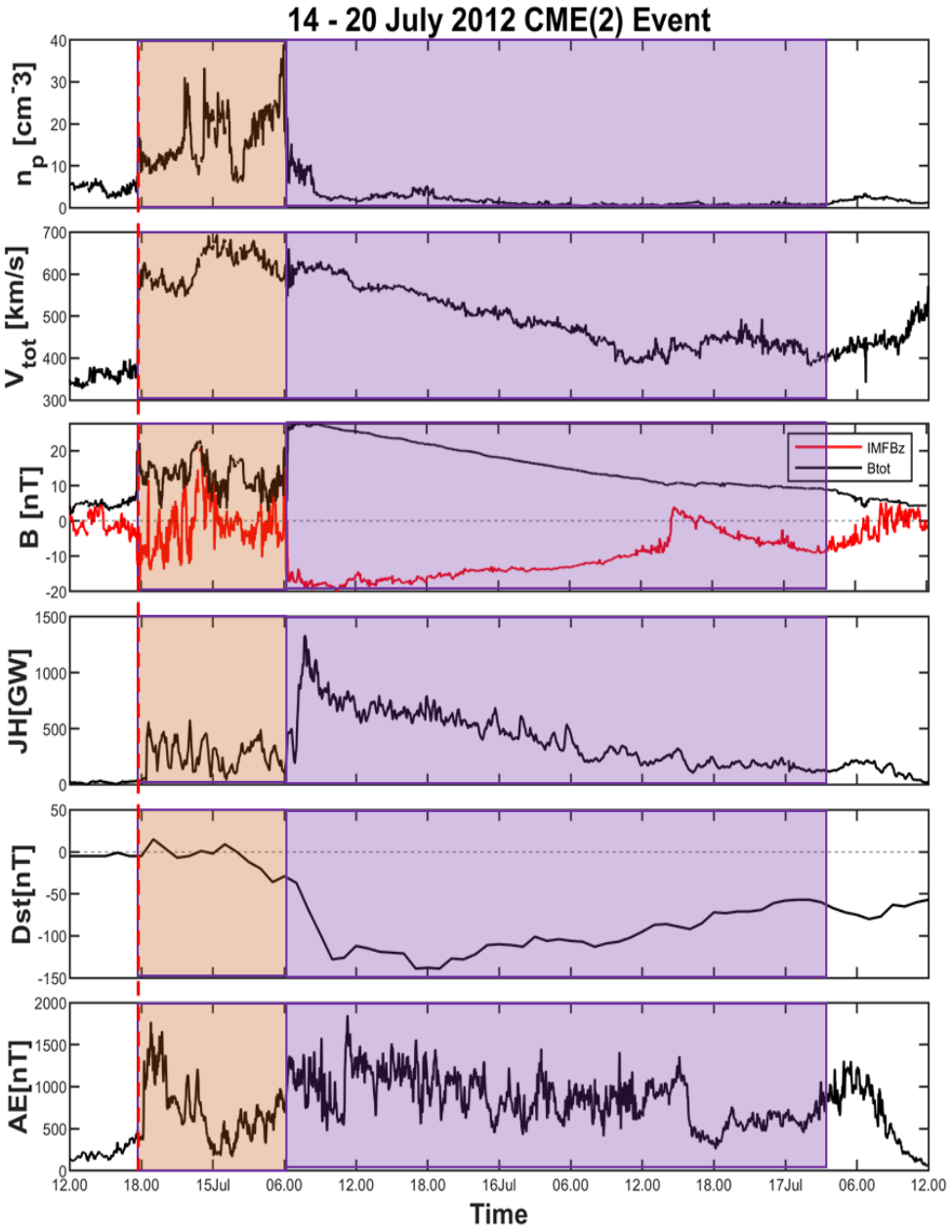

Figure 4.28: Solar wind, Joule heating and geomagnetic activity plots showing the shock (red dotted line), sheath (light orange) and magnetic obstacle (lilac) regions of CME 2.

From the figures 4.27, 4.28 and 4.29 it can be seen that fluctuations of the solar wind parameters are observed in the SH region of the ICMEs, starting just after the shock. Also, the steady decrease in proton density, solar wind speed and abrupt southward change of interplanetary magnetic field in z direction is observed within MO. Within the MO region, all parameters attain a steady and less fluctuating structure.

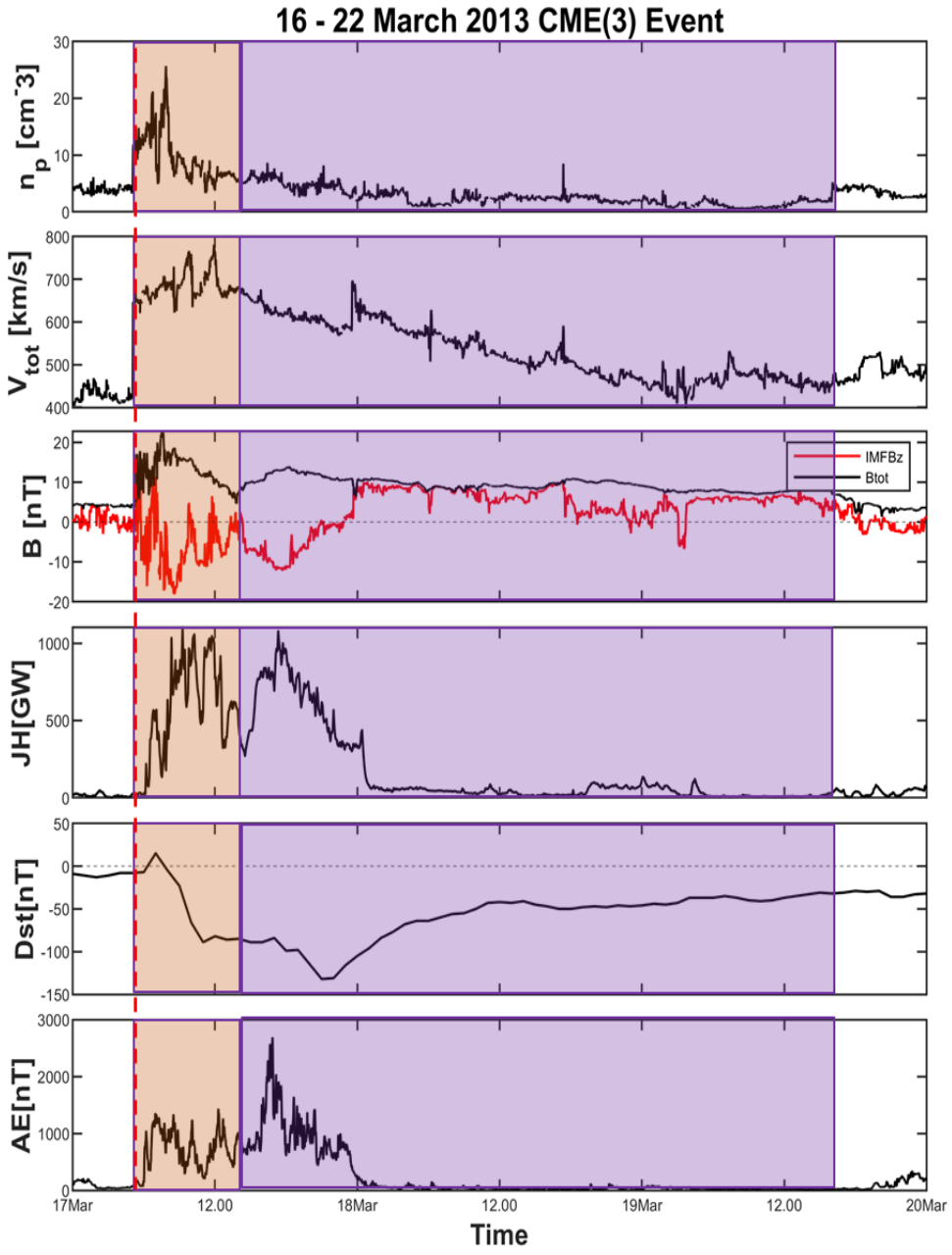

Figure 4.29: Solar wind, Joule heating and geomagnetic activity plots showing the shock (red dotted line), sheath (light orange) and magnetic obstacle (lilac) regions of CME 3.

Corresponding to these solar wind parameters, ionospheric Joule heating is low and less than 500 GW within the SH but it increases to 1000 and 1500 GW within the MO. Also it is seen that the geomagnetic disturbance enhances generally just after the shock and geomagnetic storm starts in the end of the SH region and enhances within the MO interval. Most of the heating for CME cases is due to the corresponding MO region. It

should be noted here that the time delay between the Earth based quantities such as geomagnetic indices and the arrival of solar wind from L1 point to Earth was taken into account in these plots as indicated by the use of UT for both quantities in the time axes.

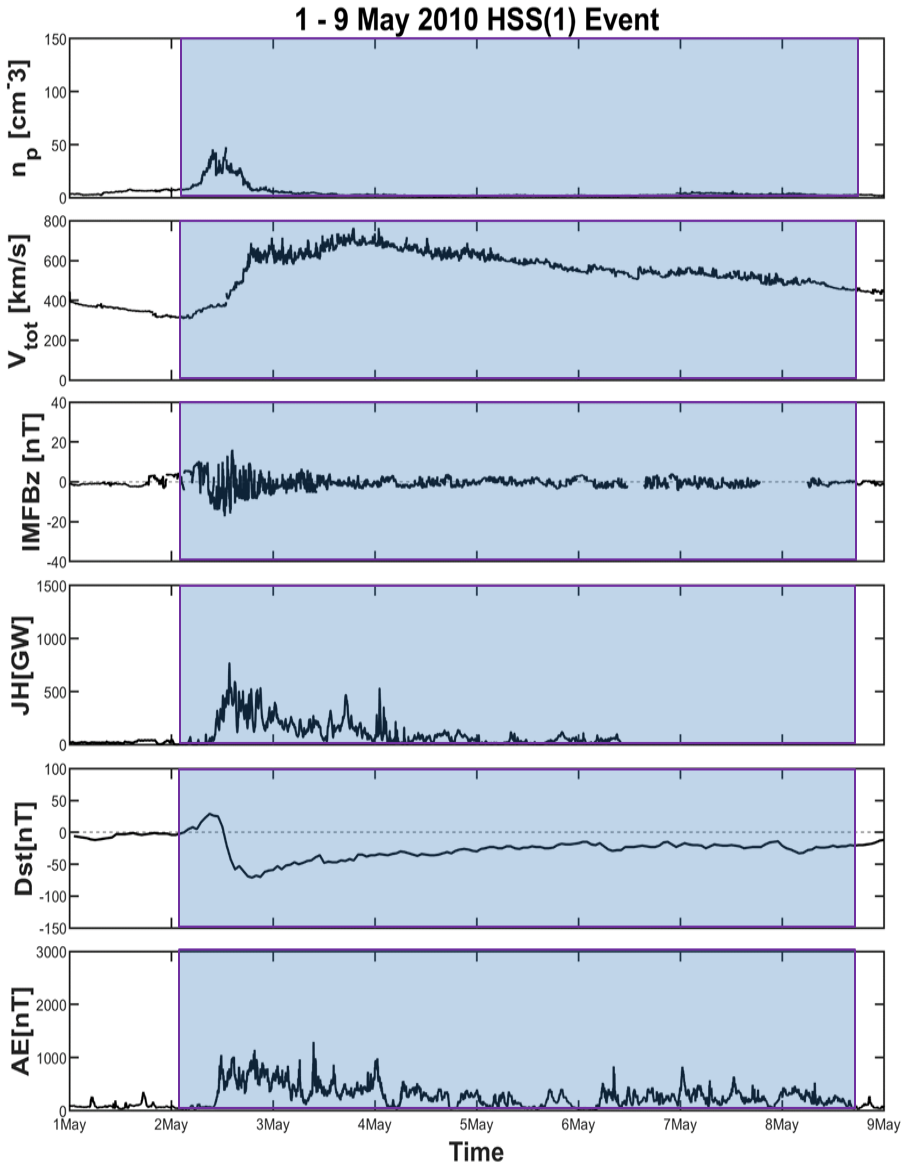

Figure 4.30: Solar wind, Joule heating and geomagnetic activity plots showing the HSS 1 interval (light blue).

From Figures 4.30, 4.31 and 4.32 it can be seen that the solar wind parameters of CIR/HSSs do not show high values as in ICME cases. And they are mostly fluctuating within the interval. Also it is seen that the Joule heating increase follows the increase

in the solar wind speed and the disturbances in the interplanetary magnetic field in z direction parameters. The maximum Joule heating is seen around 500 GW which is much less than that of CME. This value of Joule heating is seen within the SH region of a CME.

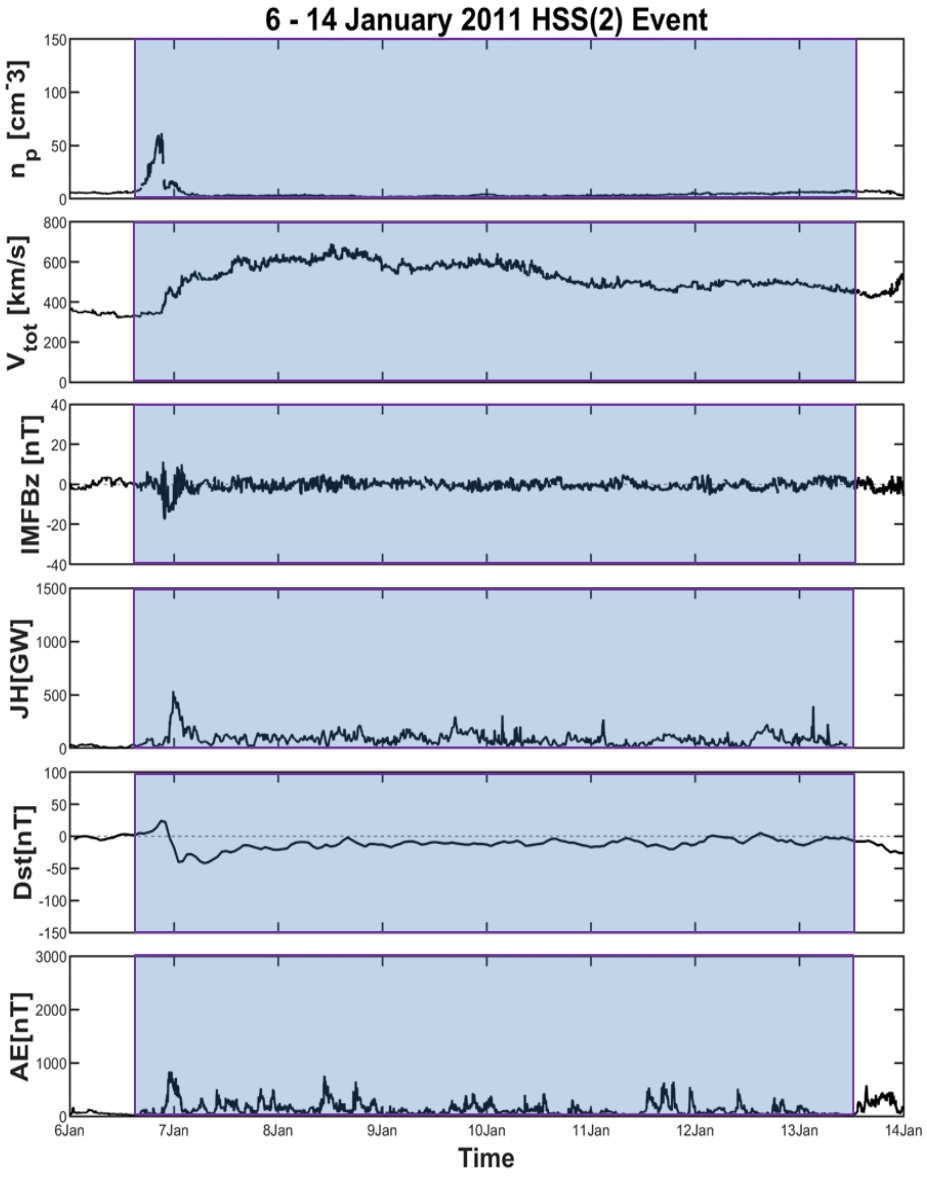

Figure 4.31: Solar wind, Joule heating and geomagnetic activity plots showing the HSS 2 interval (light blue).

Figures 4.30, 4.31 and 4.32 show a remarkable CIR/HSS pattern when it is compared to ICMEs, Joule heating does not reach the minimum values that fast and it continues fluctuating until the end of the high speed region is reached. There is a continuous

heating pattern. One thing which is clear is that as long as the HSS speed remain high, Joule heating always shows variations and does not totally goes back to zero as it is before the event. The reason of this could be the magnetospheric processes, rather than the structure of the CIR/HSS as the geomagnetic activity indices do not reach the background levels as quick as in ICME cases. And even though the CIR/HSS structure do not show high values in the geomagnetic activity parameters, heating is continuing.

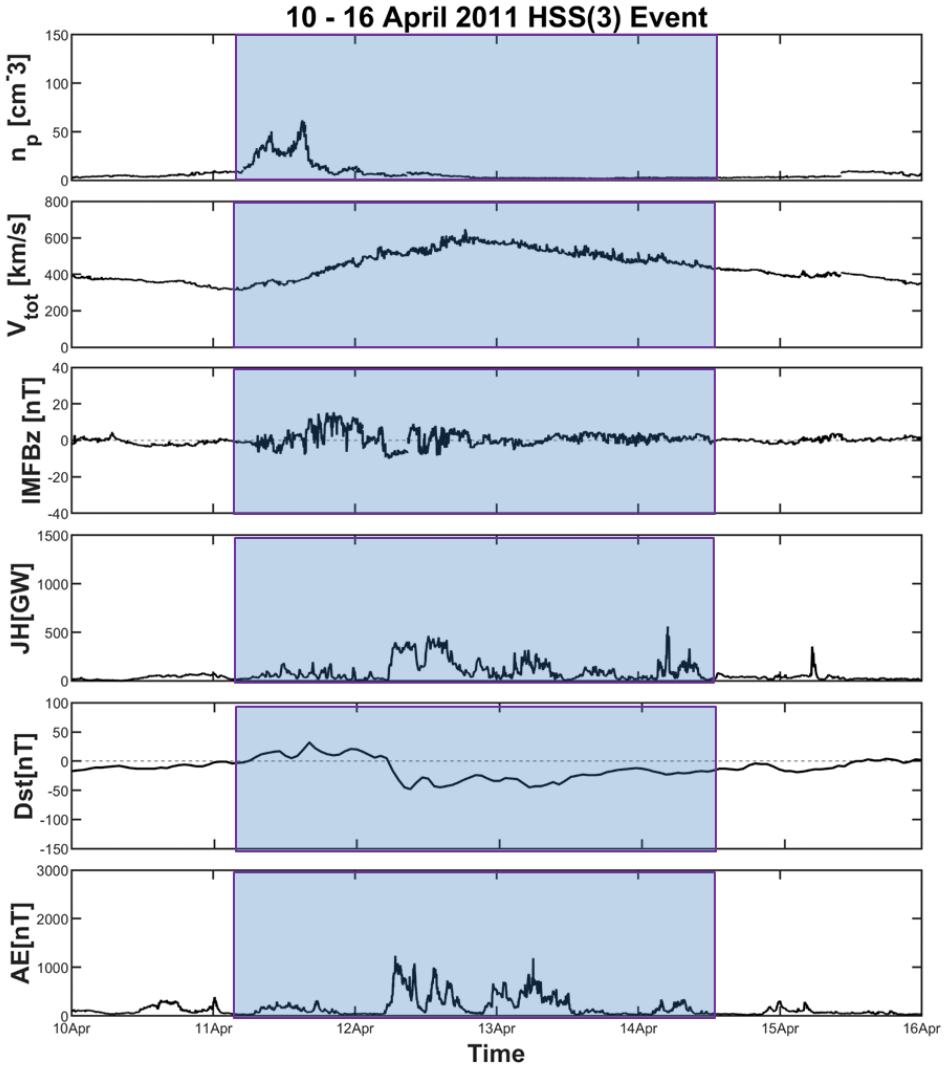

Figure 4.32: Solar wind, Joule heating and geomagnetic activity plots showing the HSS 3 interval (light blue).

To investigate the Joule heating rates within the structural intervals for CME and HSS cases, the total Joule heating (GW) corresponding to the region is unitized by dividing it into the interval duration (min). Normalization is needed because the sum of the

Joule heating rate is thought to be affected by the duration. In fact, the CMEs usually last shorter than HSS and they cause larger Joule heating. On the other hand, HSSs last longer and the magnitude of the Joule heating is much less than that of CMEs. It is thought that the normalizing the total Joule heating by the duration is one way to compare them. The unitized Joule heating is calculated for all CME cases and shown in Table 4.1. At the same time, the same procedure is applied for the HSS cases and shown in Table 4.2.

Table 4.1: Normalized Joule heating rates for each CME structure (SH, MO, ICME).

Number of Event	ICME			SH			MO		
	JH [GW]	t [min]	JH/t [GW/min]	JH [GW]	t [min]	JH/t [GW/min]	JH [GW]	t [min]	JH/t [GW/min]
CME 1	136361,9	1580	86,3	21302,6	778	27,4	115105,0	802	143,5
CME 2	332888,1	3462	96,2	49379,9	755	65,4	283972,8	2707	104,9
CME 3	191343,5	3523	54,3	76518,9	528	144,9	115212,8	2995	38,5
Average	220197,8	2855	77,1	49067,2	687	71,4	171430,2	2168	79,1

Table 4.2: Normalized Joule heating rates for each HSS structure.

Number of Event	HSS		
	JH [GW]	t [min]	JH/t [GW/min]
HSS 1	173000,6	6240	27,7
HSS 2	211800,0	9840	21,5
HSS 3	127965,6	4740	27,0
Average	169882,8	7290	23,3

Table 4.1 explains the unitized Joule heating rate of coronal mass ejection cases within the whole interval (ICME), sheath (SH) and magnetic obstacle (MO) regions. The highest Joule dissipation is observed in the MO region with 79.1 GW/min rate, but the Joule heating corresponding to the SH region is also very close to this value. From the tables 4.1 and 4.2, it is clearly seen that averagely, CMEs in the interplanetary space result with 77.1 GW/min unit heating, while the CIR/HSSs result with 23.3 GW/min unit heating. Overall, the energy from ICMEs dissipate in the form of Joule heating 3.3 times more than the energy from CIR/HSSs. This part of the study investigated the solar wind properties that the Joule heating amount depends upon. While the solar wind properties control the energy impinging on the whole magnetosphere, Earth's magnetotail modifies this energy and decides how it will be distributed in the

magnetosphere-ionosphere system. Therefore, it is important to find out how the Joule heating varies during each phase of a geomagnetic storm caused by a CME or HSS. In order to investigate this point, a similar analysis is performed for the different phases of a geomagnetic storm in the following section.

4.4 ICME and CIR/HSS Driven Geomagnetic Storm Analysis with Joule Heating

The geomagnetic storm intensity of both phenomena and the phases of the geomagnetic storms were explained and discussed in the previous sections. In this section, the geomagnetic storms driven by both phenomena will be investigated in relation to Joule heating for the full storm interval and also for the different storm phases for the corresponding Joule heating rates. It is known that geomagnetic storms have three main phases; initial, main and recovery. The storm phase intervals were determined by the criteria used in Partamies et. al. (2013). Table 4.3 shows the geomagnetic storm phase durations for each CME and HSS cases.

Table 4.3: Geomagnetic storm phase intervals for ICME and CIR/HSS cases.

Number of Event	Initial Phase		Main Phase		Recovery Phase	
	Start Time	End Time	Start Time	End Time	Start Time	End Time
CME 1	16/06/2012 10.00	17/06/2012 08.00	17/06/2012 08.00	17/06/2012 14.00	17/06/2012 14.00	19/06/2012 00.00
CME 2	14/07/2012 19.00	15/07/2012 04.00	15/07/2012 04.00	15/07/2012 19.00	15/07/2012 19.00	19/07/2012 12.00
CME 3	17/03/2013 06.00	17/03/2013 09.00	17/03/2013 09.00	17/03/2013 21.00	17/03/2013 21.00	21/03/2013 13.00
HSS 1	02/05/2010 03.00	02/05/2010 13.00	02/05/2010 13.00	02/05/2010 19.00	02/05/2010 19.00	06/05/2010 01.00
HSS 2	06/01/2011 11.00	06/01/2011 23.00	06/01/2011 23.00	07/01/2011 06.00	07/01/2011 06.00	08/01/2011 13.00
HSS 3	11/04/2011 07.00	12/04/2011 07.00	12/04/2011 07.00	12/04/2011 10.00	12/04/2011 10.00	13/04/2011 21.00

Figures 4.33, 4.34 and 4.35 show the ICME-driven geomagnetic storm phases colored in light green, light orange and light blue respectively for initial, main and recovery phases using the criteria by Partamies et. al. (2013). Figures 4.36, 4.37 and 4.38 show the same for CIR/HSS. The top panel gives the disturbance storm time index (Dst) and the bottom panel represents Kp indices respectively. The analyses were performed for the geomagnetic storm phases with the same procedure described in the previous

section. First, the sum of the Joule heating rate (GW) corresponding to each storm phase was summed and divided by the duration in minutes for easy comparisons. The Joule heating rate was unitized to make the comparison easier. The highest Joule heating rate is expected within the main phase intervals of the ICME and CIR/HSS-driven geomagnetic storms due to the enhanced disturbance.

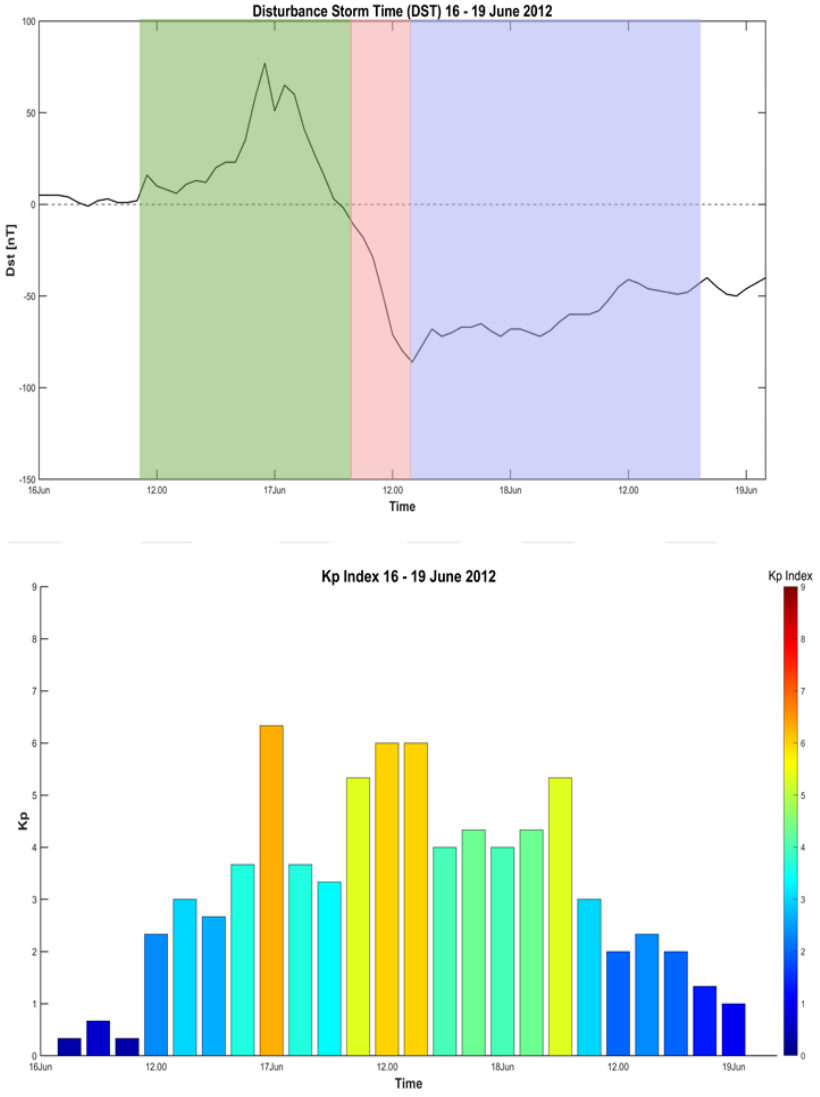

Figure 4.33: Geomagnetic storm phases corresponding to the ICME 1-driven storm. Initial, main and recovery phase intervals are shown in light green, light orange and light blue respectively.

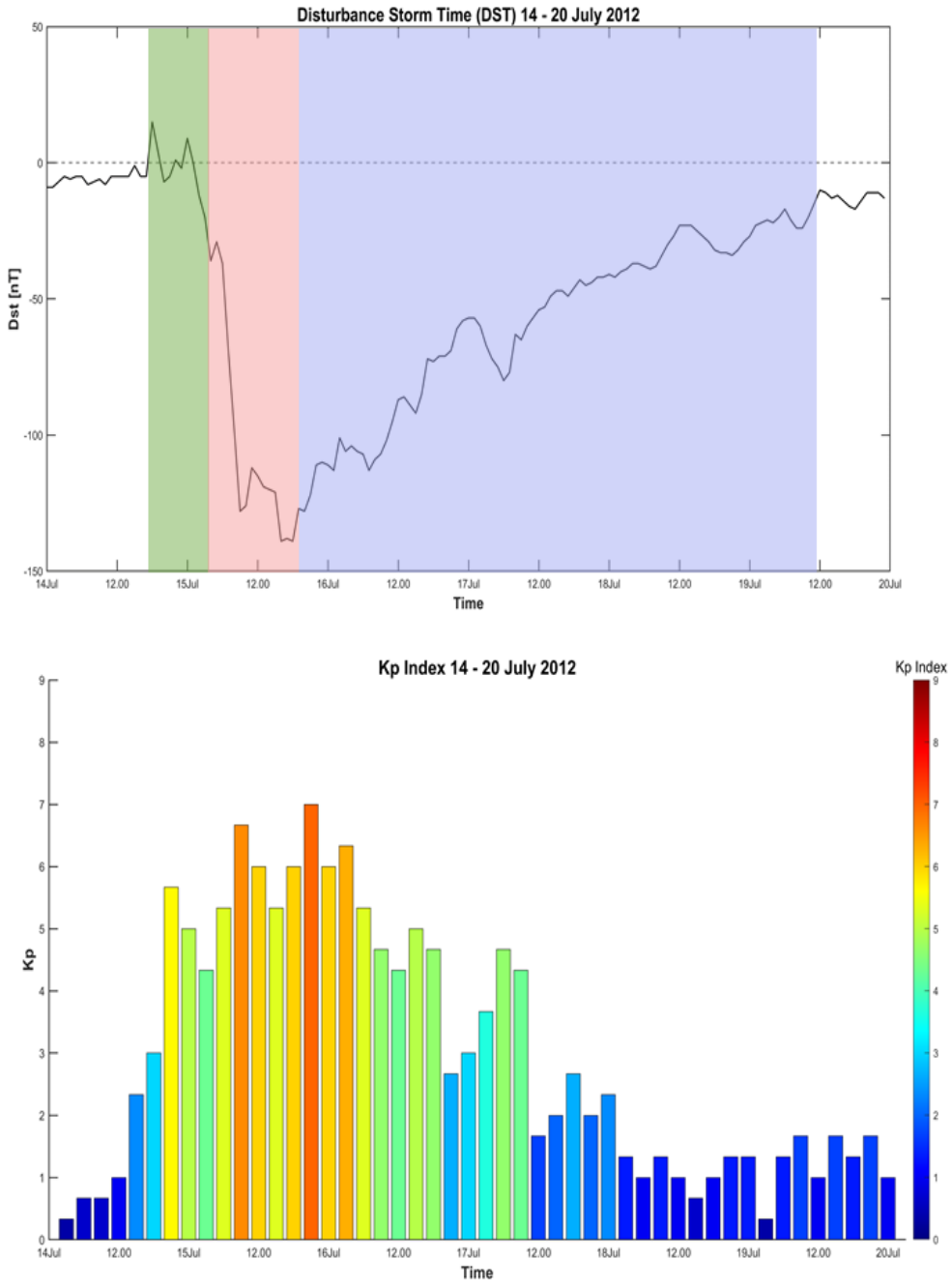

Figure 4.34: Geomagnetic storm phases corresponding to the ICME 2-driven storm. Initial, main and recovery phase intervals are shown in light green, light orange and light blue respectively.

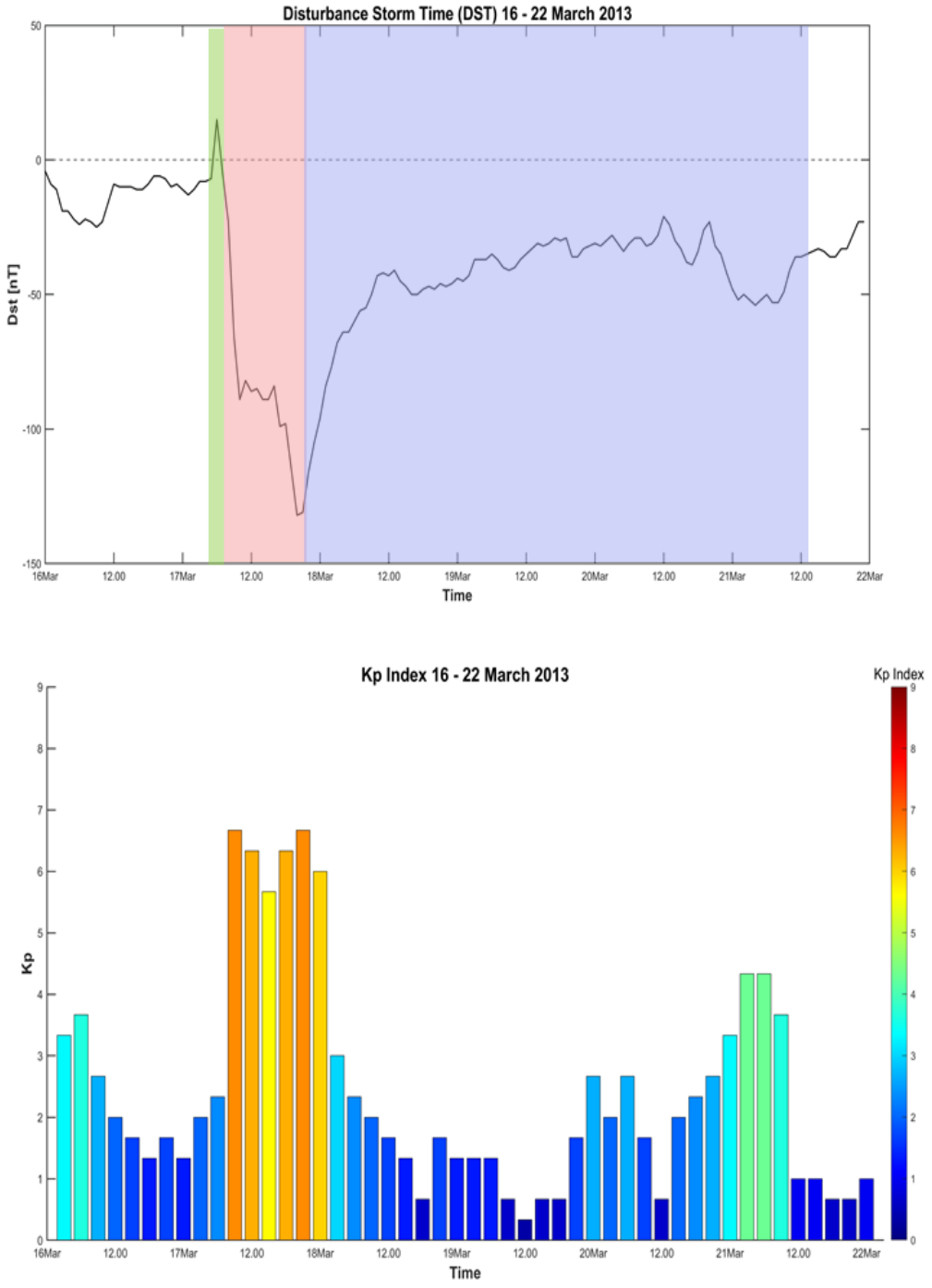

Figure 4.35: Geomagnetic storm phases corresponding to the ICME 3-driven storm. Initial, main and recovery phase intervals are shown in light green, light orange and light blue respectively.

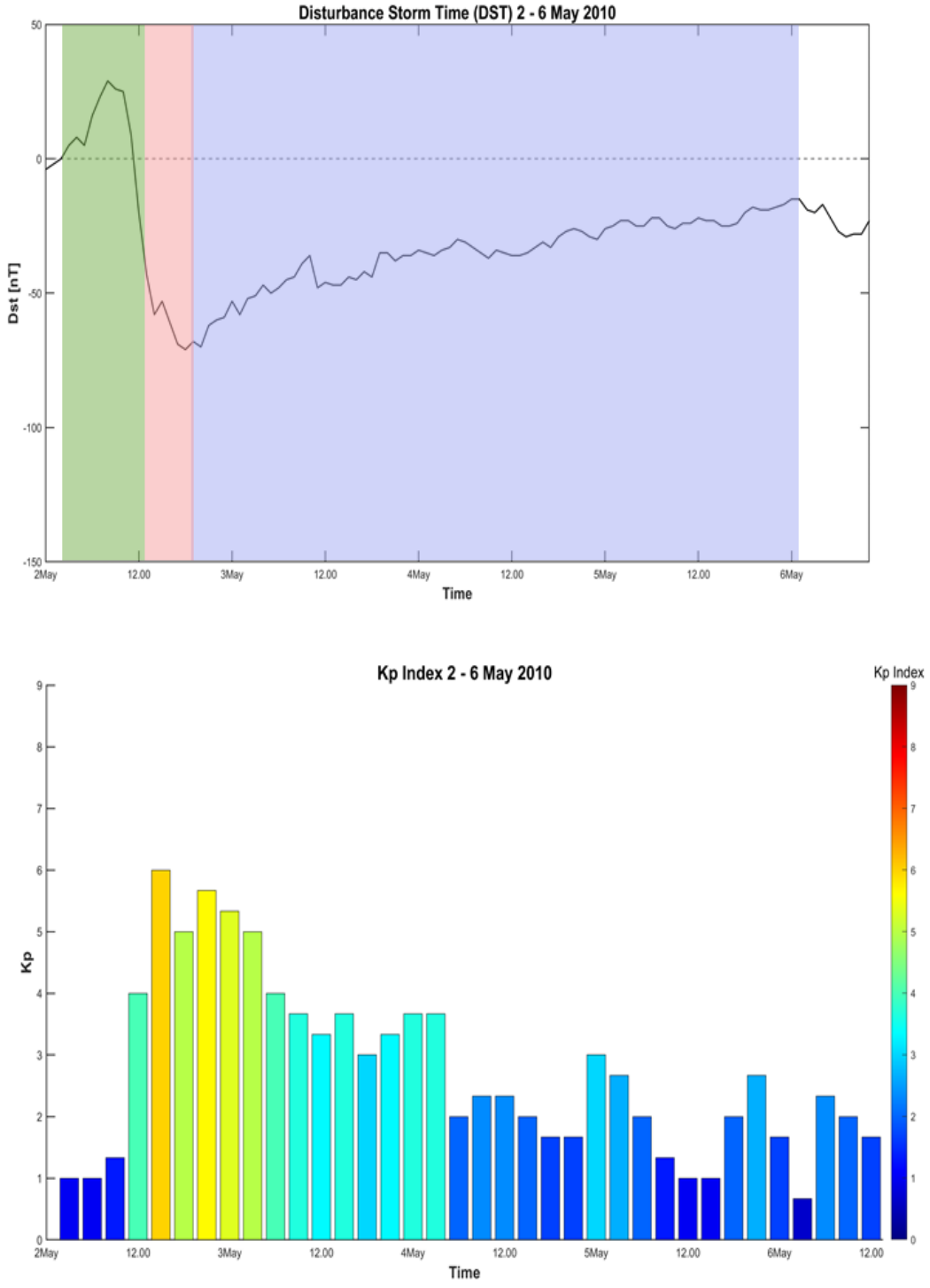

Figure 4.36: Geomagnetic storm phases corresponding to the CIR/HSS 1-driven storm. Initial, main and recovery phase intervals are shown in light green, light orange and light blue respectively.

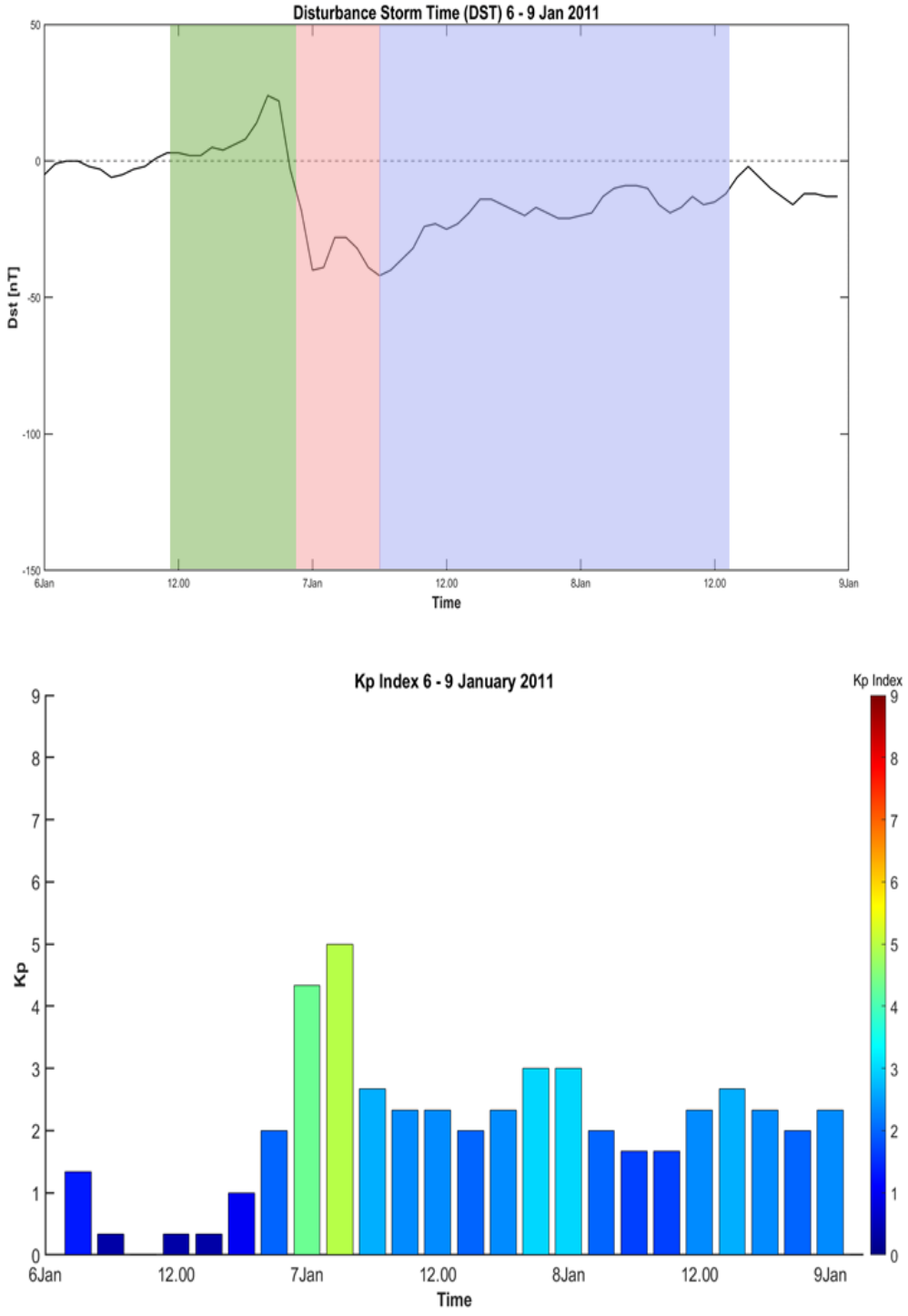

Figure 4.37: Geomagnetic storm phases corresponding to the CIR/HSS 2-driven storm. Initial, main and recovery phase intervals are shown in light green, light orange and light blue respectively.

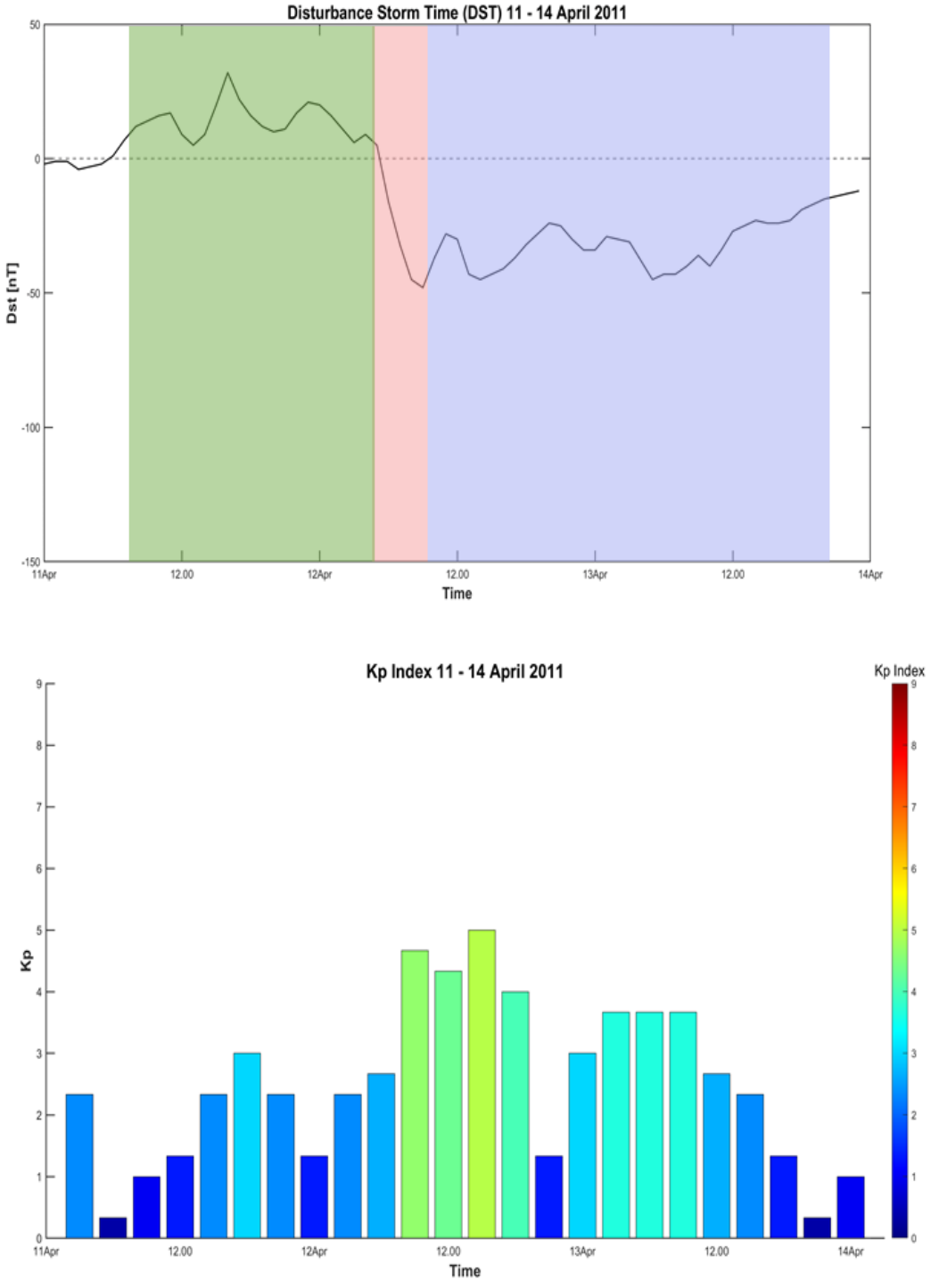

Figure 4.38: Geomagnetic storm phases corresponding to the CIR/HSS 3-driven storm. Initial, main and recovery phase intervals are shown in light green, light orange and light blue respectively.

Once the geomagnetic storm phases were determined for each case, the normalized Joule heating rate corresponding to these intervals were calculated and shown in Table 4.4. Table 4.5 also provides the Joule heating rates for the full storm interval.

Table 4.4: Corresponding Joule heating rates in unit time for each geomagnetic storm phase driven by ICME and CIR/HSS.

Number of Event	Initial Phase			Main Phase			Recovery Phase		
	JH [GW]	t [min]	JH/t [GW/min]	JH [GW]	t [min]	JH/t [GW/min]	JH [GW]	t [min]	JH/t [GW/min]
CME 1	90880,5	1320	68,8	63231,7	360	175,6	49801,4	360	138,3
CME 2	36704,4	540	68,0	145216,8	900	161,4	145216,8	5340	27,2
CME 3	19498,6	180	108,3	108492,5	720	150,7	114252,3	5280	21,6
Average CME	49027,8	680	72,1	105647,0	660	160,1	103090,2	3660	28,2
HSS 1	13953,8	600	23,3	35042,5	360	97,3	118745,9	4680	25,4
HSS 2	6911,7	720	9,6	24792,0	420	59,0	39023,7	1860	21,0
HSS 3	23857,2	1440	16,6	15309,7	180	85,1	69827,2	2100	33,3
Average HSS	14907,5	920	16,2	25048,1	320	78,3	75865,6	2880	26,3

Table 4.5: Corresponding Joule heating rates in unit time for full geomagnetic storm interval driven by ICME and CIR/HSS

Number of Event	Full Storm		
	JH [GW]	t [min]	JH/t [GW/min]
CME 1	203913,6	2040	100,0
CME 2	327137,9	6780	48,3
CME 3	242243,5	6180	39,2
Average CME	257765,0	5000	51,6
HSS 1	167742,2	5640	29,7
HSS 2	70727,4	3000	23,6
HSS 3	108994,1	3720	29,3
Average HSS	115821,2	4120	28,1

As it is seen from the tables, the highest normalized Joule heating rate per unit time is obtained during the main phase of a geomagnetic storm for both events even though its duration is the shortest phase compared to other two phases. The storm main phase Joule heating rate for CMEs on average is higher than HSSs by a factor of 2.04. Another important result that comes out of these comparisons is that ICME-driven geomagnetic storms dissipate 1.83 times more in the form of Joule heating in unit time when it is compared to CIR/HSS- driven storms on average. In the next sections, the

controlling parameters of Joule heating are investigated using the solar wind parameters and geomagnetic indices.

4.5 Linear Regression Analysis and Pearson Correlations of Joule Heating Controlling Parameters

In this section, the effect of ICME and CIR/HSS structures on Joule heating are investigated by using simple linear regression (SLR) and multi linear regression (MLR) methods by using MATLAB linear models. The 9 solar wind parameters and geomagnetic activity indices were decided to investigate with Joule heating rate. These are solar wind speed, proton density, temperature, dynamic pressure, plasma beta, interplanetary magnetic field in z direction for space-based measurements and AE, Dst and Kp for ground-based measurements. The time series of each parameter versus Joule heating for CME 1 (ICME, SH, MO regions), CME 2 (ICME, SH, MO regions), CME 3 (ICME, SH, MO regions) and HSS 1, HSS 2, HSS 3 were given in the Appendices A and B. As a simple linear regression fit model, Equation 4.1 is used on the data sets where b_0 is the intercept and b_1 is the slope (or regression coefficient).

$$y = b_0 + b_1 x \tag{4.1}$$

Also, the correlation coefficient is calculated for each performed regression. In this section, the pilot events CME 2 and HSS 2 are given in detail for SLR analysis, and CME 1, CME 3, HSS 1, HSS 3 events for SLR analysis are given in Appendices C, D and E. The SLR and MLR analyses were performed for each CME and each structural region of CME, as well as for each HSS case. Then the CME 2 and CME 3 data sets were combined. Also, HSS 2 and HSS 3 data sets were combined to perform a statistical analysis on a large data set. CME 1 was extracted from the combined data set due to its reverse correlations in some parameters, which could have arisen from the shape of the flux rope within the magnetic obstacle. While CME 2 and CME 3 was reported to present a normal flux rope as a magnetic obstacle type, CME 1 was reported that it had large rotation flux rope type. Shape of its flux rope within the magnetic obstacle is determined to be opposite to what mostly observed. This case needs further investigation in detail for our further studies. HSS 1 is also extracted from the dataset

due to the large interval of missing Joule heating data because of the exceeded limits of the model run. Figures 4.39 and 4.40 show respectively the ICME, SH and MO regions and Joule heating correlations with selected 9 parameters for the pilot CME event, CME 2. Figures 4.41 and 4.42 show respectively the ICME, SH and MO regions and Joule heating correlations with selected 9 parameters for the combined data set from CME cases. Figure 4.43 shows HSS interval and Joule heating correlations with selected 9 parameters for the pilot HSS event and for the combined data set from HSS cases.

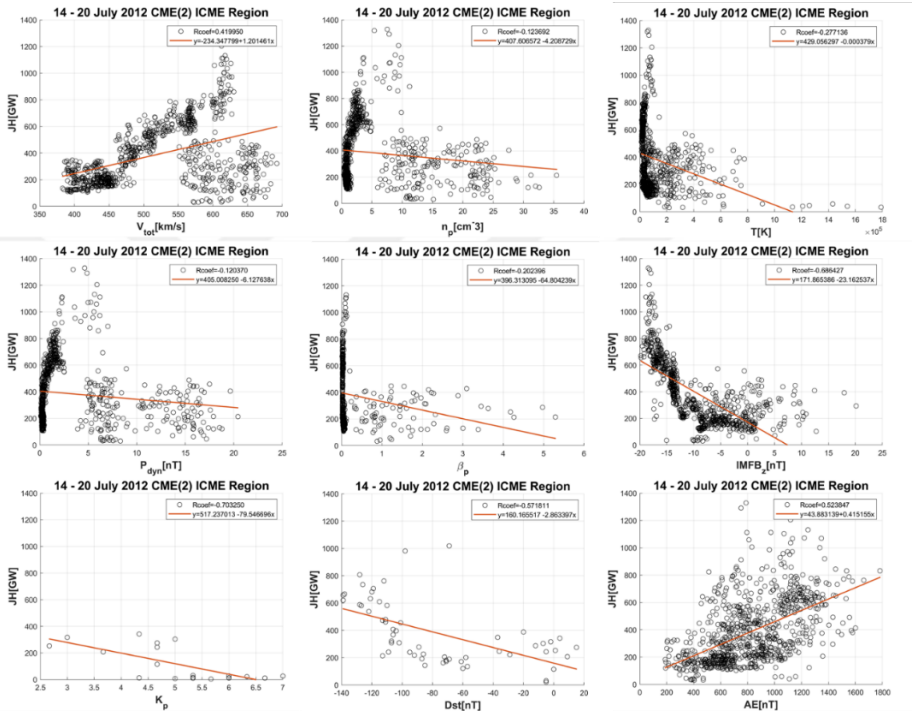

Figure 4.39: ICME regions and Joule heating correlations using selected 9 parameters for the pilot CME event (CME 2).

For the ICME region of the pilot event (CME 2), it is seen that the correlations are low with the solar wind parameters, except the interplanetary magnetic field in z direction. IMFB_Z shows the highest correlation with $r_{corr} = -0.68$ among all parameters, which means the more negative the IMFB_Z, the more energy dissipation in the form of Joule heating. As it will be seen clearly when the CME regions are separated, the high correlation of IMF Bz for the whole CME 2 is mostly due to the contribution of southward IMFs within the magnetic obstacle in the interval. When the ground based observed parameters are examined, the high correlations are seen as $r_{corr} = 0{,}52, -0.57, -0.70$ respectively for AE, Dst and K_p indices.

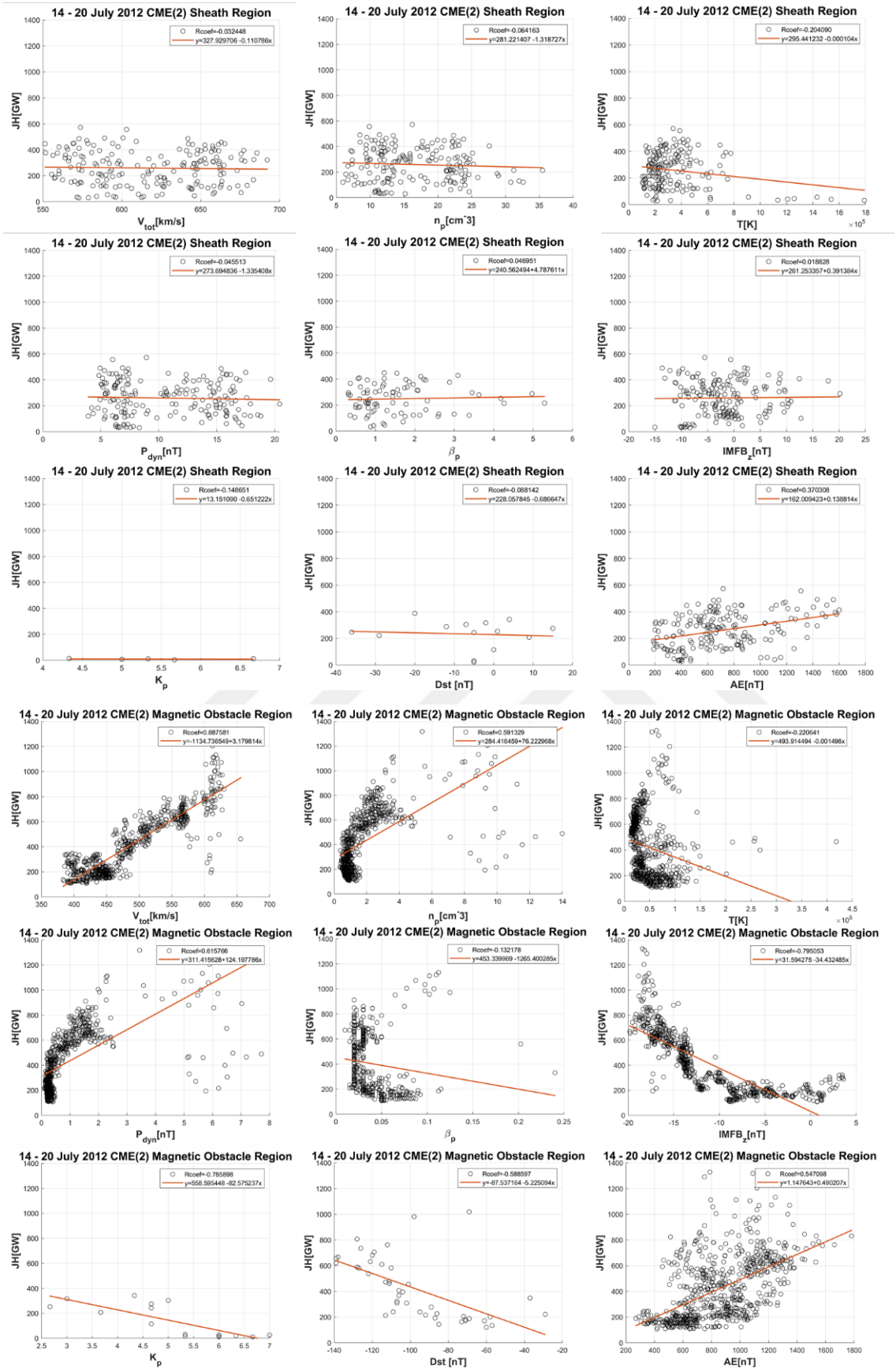

Figure 4.40: SH (top 9) and MO (bottom 9) regions and Joule heating correlations using selected 9 parameters for the pilot CME event (CME 2).

The structure of CME is revealed very nicely in these plots. Sheath region appears with high temperature, low speed, high density and high dynamic pressure and with lower IMF Bz. The clustered region of the figure corresponds to the magnetic obstacle part of the ICME, populated by the particles with high speed, low density, low temperature and low dynamic pressure with strong southward IMF Bz. Examining the correlations for the sheath region of CME 2, it can be seen that the correlations are extremely low. This is mostly due to the fluctuations in the sheath region. Turbulance within the sheath region of CME prevents any correlation with the Joule heating in the ionosphere. Also, the ground based observed parameters show extremely low correlations except AE index $r_{corr} = 0{,}37$. On the other hand, MO region of the pilot event (CME 2) provides better correlations with almost all the parameters. $r_{corr} = 0{,}88, 0.59, 0.61, -0.79$ are the correlations respectively for solar wind speed, proton density, dynamic pressure and IMFB_Z for the solar wind parameters. Also the geomagnetic activity indices AE, Dst and K_p show high correlations as $r_{corr} = 0{,}54, -0.58, -0.78$, respectively. As a result of this simple analysis, it can be seen that the magnetic obstacle is overall the most controlling structure of CME. Among the parameters on the other hand, it is again seen that it is the southward IMF that causes the largest correlation and thus the largest Joule heating. The same steps were performed for the combined data set too. For the ICME region of combined CME dataset, it is found that solar wind speed and IMFB_Z give the highest correlations respectively $r_{corr} = 0.50, -0.71$ among the solar wind parameters. As for the ground-based measurements, AE and Dst give the highest correlation as $r_{corr} = 0.74, -0.58$. The correlations in the sheath region for the combined CME dataset are also found to be very low compared to the combined magnetic obstacle region. The highest correlations again were observed in the solar wind velocity and IMFB_Z respectively $r_{corr} = 0.56, -0.60$ and also for Dst and K_p indices as $r_{corr} = -0.76, 0.54$.

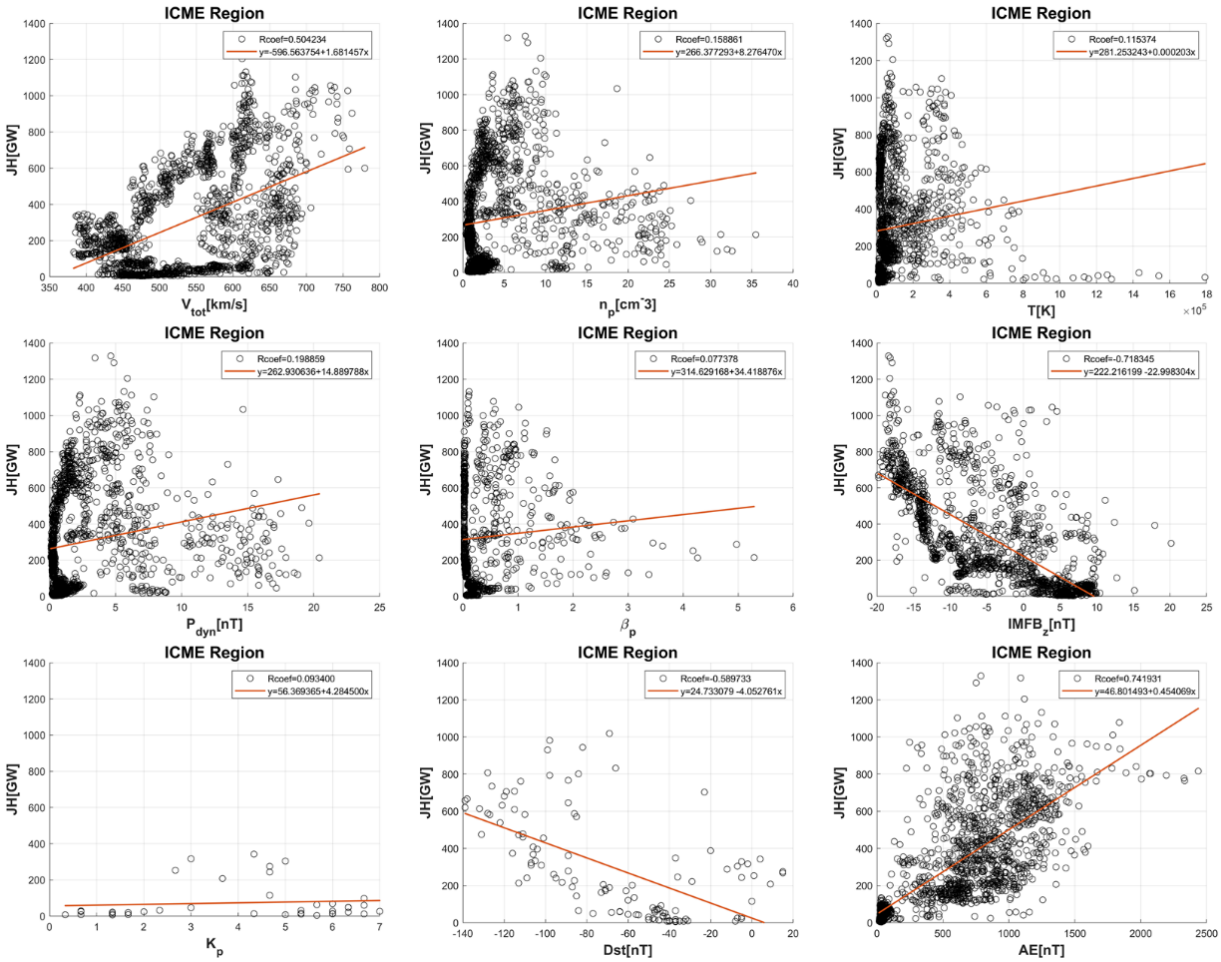

Figure 4.41: ICME regions and Joule heating correlations using selected 9 parameters for the combined data set.

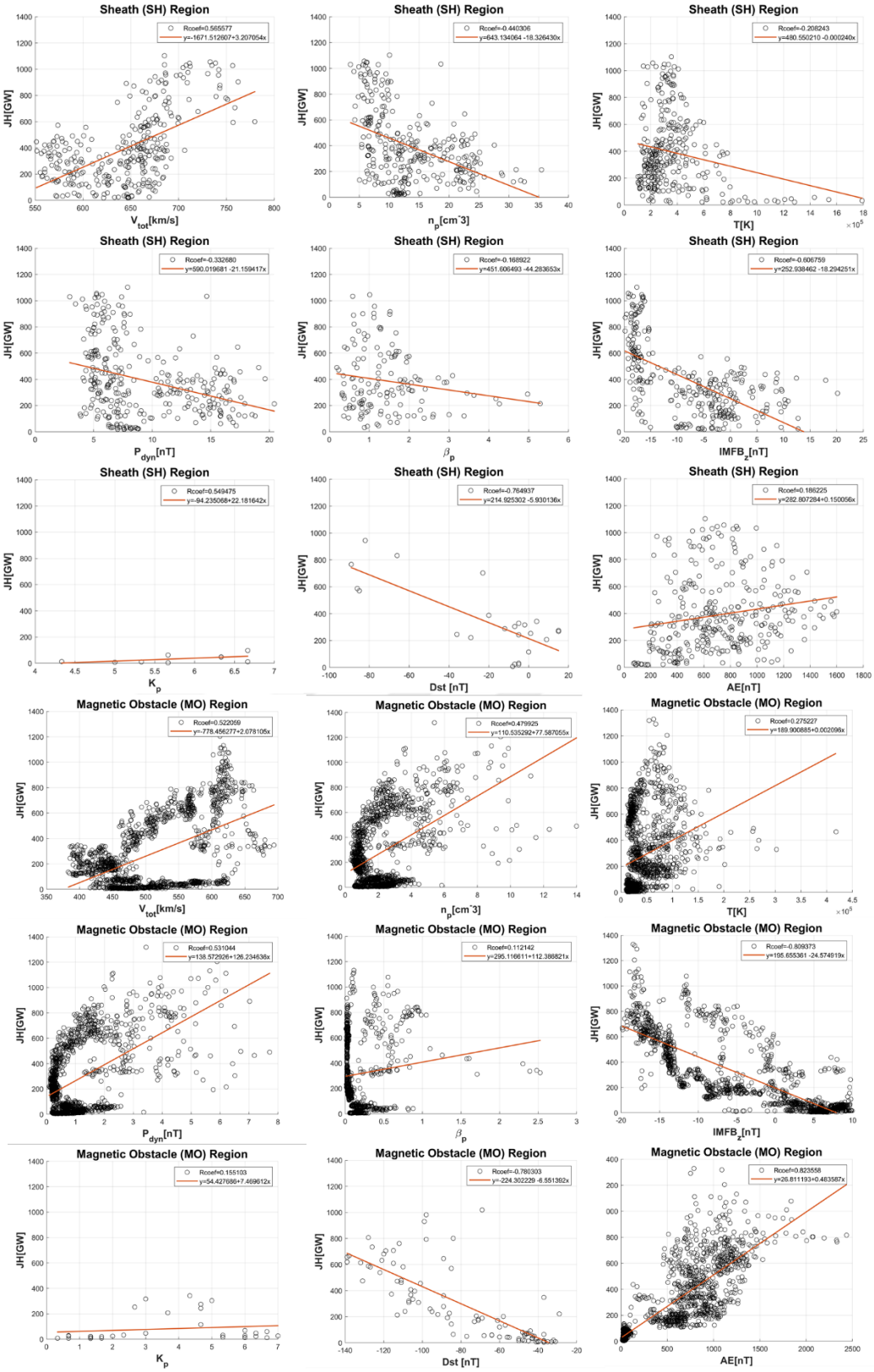

Figure 4.42: SH (top 9) and MO (bottom 9) regions and Joule heating correlations using selected 9 parameters for the combined data set.

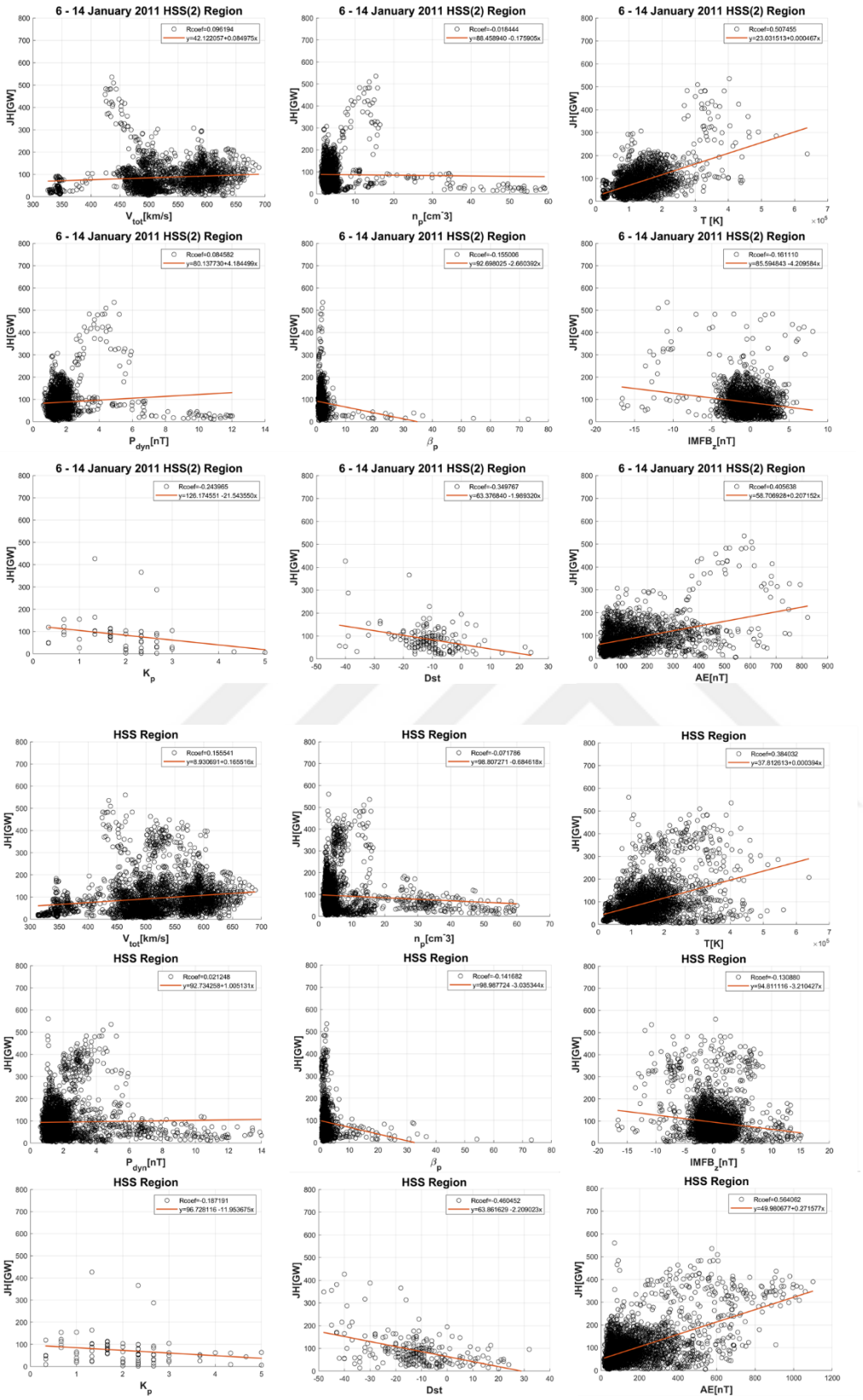

Figure 4.43: HSS2 (top 9) and combined (bottom 9) regions and Joule heating correlations using selected 9 parameters.

For the magnetic obstacle region, almost all the correlations were observed to be the highest compared to the whole ICME or SH region. Solar wind speed, dynamic pressure, $IMFB_Z$, AE and Dst showed correlations as r_{corr} = 0.52, 0.55, -0.80, 0.82 and -0.70, respectively. The same procedure was applied for HSS cases. The pilot event, HSS 2, showe the highest correlations with the temperature and AE as r_{corr} = 0.50, 0.40. The combined HSS data set also showed the highest correlations in temperature, AE and Dst as r_{corr} = 0.38, 0.56, -0.46 respectively. The most remarkable difference here is that the Joule heating driven by HSSs does not seem to mostly depend on solar wind. It shows a dependence on geomagnetic activity parameters measured on the ground after the energy exchange by solar wind-magnetosphere coupling processes. That means, the HSS-driven JH is mainly controlled by the magnetospheric processes that occur after the energy deposited in the magnetotail via near Earth magnetic reconnection. But for the CME-driven JH , it is the opposite. It seems to be that the main controlling parameter is the solar wind kinetic energy. Tables 4.6, 4.7, 4.8 and 4.9 show all correlation coefficients obtained for each CME and HSS cases and also for their corresponding combined data set for 9 parameters; solar wind velocity, proton density, temperature, dynamic pressure, plasma beta, interplanetary magnetic field in z direction, AE, Dst and Kp indices.

Table 4.6: Correlation coefficients of Joule heating rates with parameters for ICME region of CMEs.

Number of Event	Correlation Coefficients for ICME region			
	CME 1	CME 2	CME 3	Combined
Vsw	-0.03	0.41	0.74	0.50
np	0.0003	-0.12	0.57	0.15
T	-0.19	-0.27	0.43	0.11
Pdyn	-0.04	-0.12	0.60	0.19
β	-0.49	-0.20	0.48	0.07
IMFBz	-0.43	-0.68	-0.77	-0.71
AE	0.81	0.52	0.83	0.74
Dst	-0.45	-0.57	-0.60	-0.58
Kp	0.74	-0.70	0.87	0.09

Table 4.7: Correlation coefficients of Joule heating rates with parameters for SH region of CMEs.

Number of Event	Correlation Coefficients for SH region			
	CME 1	CME 2	CME 3	Combined
Vsw	0.32	-0.03	0.56	0.56
np	0.54	-0.06	-0.35	-0.44
T	-0.20	-0.20	-0.46	-0.20
Pdyn	0.55	-0.04	-0.26	-0.33
β	-0.27	0.04	-0.25	-0.16
IMFBz	0.36	0.01	-0.16	-0.60
AE	0.34	0.37	0.14	0.18
Dst	0.62	-0.08	-0.76	-0.76
Kp	0.91	-0.14	0.34	0.54

Table 4.8: Correlation coefficients of Joule heating rates with parameters for MO region of CMEs.

Number of Event	Correlation Coefficients for MO region			
	CME 1	CME 2	CME 3	Combined
Vsw	-0.78	0.88	0.66	0.52
np	-0.43	0.59	0.79	0.47
T	0.15	-0.22	0.65	0.27
Pdyn	-0.58	0.61	0.82	0.55
β	0.47	-0.13	0.49	0.11
IMFBz	-0.80	-0.79	-0.84	-0.80
AE	0.80	0.54	0.92	0.82
Dst	0.62	-0.58	-0.80	-0.70
Kp	0.62	-0.78	0.85	0.15

Table 4.9: Correlation coefficients of Joule heating rates with parameters for HSSs.

Number of Event	Correlation Coefficients for HSSs			
	HSS 1	HSS 2	HSS 3	Combined
Vsw	0.25	0.09	0.33	0.15
np	0.17	-0.01	-0.15	-0.07
T	0.79	0.50	0.27	0.38
Pdyn	0.52	0.08	-0.06	0.02
β	-0.25	-0.15	-0.14	-0.14
IMFBz	-0.24	-0.16	-0.16	-0.13
AE	0.69	0.40	0.64	0.56
Dst	-0.58	-0.34	-0.52	-0.46
Kp	0.60	-0.24	0.14	-0.18

The results of simple linear regression (SLR) analysis clearly indicate that the highest correlations between the Joule heating and the solar wind parameters were observed for solar wind speed, southward IMF Bz and AE index. Table 4.10 shows the p-values, indicating the statistical significance, for the correlations between Joule heating and parameters corresponding to each CME and HSS region.

Table 4.10: Significance levels at $\alpha = 0.05$ level using p-value. P-value < α indicates that the correlation between the parameters given on the top row and Joule heating produced by the solar wind drivers indicated on the first column on the left, exists determined by the Pearson correlation coefficients given in Tables 4.6, 4.7, 4.8 and 4.9.

Number of Event	p-values								
	Vsw	np	T	Pdyn	β	IMFBz	AE	Dst	Kp
ICME1	0.53	0.99	0	0.36	0	0	0	0.01	0.02
ICME2	0	0	0	0	0	0	0	0	0
ICME3	0	0	0	0	0	0	0	0	0
Combined	0	0	0	0	0.01	0	0	0	0.56
SH1	0	0	0	0	0	0	0	0.01	0.02
SH2	0.66	0.38	0	0.53	0.67	0.80	0	0.76	0.81
SH3	0	0	0	0	0.04	0.06	0.09	0.01	0.58
Combined	0	0	0	0	0.04	0	0	0	0.12
MO1	0	0	0.03	0	0	0	0	0.01	0.25
MO2	0	0	0	0	0	0	0	0	0
MO3	0	0	0	0	0	0	0	0	0
Combined	0	0	0	0	0	0	0	0	0.38
HSS1	0	0	0	0	0	0	0	0	0
HSS2	0	0.38	0	0	0	0	0	0	0.07
HSS3	0	0	0	0.30	0	0	0	0	0.48
Combined	0	0	0	0.21	0	0	0	0	0.09

Level of significance (α) was selected as %5 (0.05) with the confidence level of %95 for the significance test in this analysis. When the Table 4.10 is examined, it can be clearly seen that most of p-values are very close to zero, meaning less than alpha significance level determined as 0.05 level here. Overall, with a few exceptions, these results pass the significance test, supporting large correlation coefficients and showing significant correlation between the associated variables, as discussed in detail above. Examining the p-values of CMEs, it is seen that the SH region correlations fall below the level of significance, as also indicated by the linear fits as well as the correlation coefficients given in Figures 4.40 and 4.42. The CME 1 case represents a different flux rope structure and therefore the significance test fails with almost all parameters. However, this case is the subject of a detailed investigation, which is one of our future

studies. Other than that, all individual ICME regions show a p-value of zero meaning the correlations are robust and reliable. While the SH 1 shows p-values less than 0.05 significance level, indicating that the correlation is meaningful, the SH 2 and SH 3 regions of CMEs fail to give a reliable p-value for most parameters. Similarly, the combined SH region presents significant correlations with almost all solar wind parameters. In contrast to the SH region of the CMEs, the MO region of all CMEs presents reliable correlation coefficients. Compared with CME events, it seems that HSS cases did not reliably correlate with the Kp index and density in the case of HSS 1 and pressure in the case of combined HSS. In terms of reliability, although the correlation coefficients are of different strengths, it is seen that the correlation coefficients found for both CME conditions and HSS conditions are equally significant. Finally, it can also be seen that the significance test using p-value indicates that all drivers, except combined cases show low correlation with Kp which is expected since the number of Kp data are very few. As a result of the significance test using p-value, it can be concluded that the results from p-value follow the interpretations of the panels presented in Figures 4.39-4.43. These results are very important in the prediction of Joule heating. The parameters with high correlations can be used to predict and model Joule heating variations that have effects on the upper atmosphere and satellite operations. This leads us to advance our correlation study one step further and apply multi linear regression (MLR) between the Joule heating and most effective solar wind parameters found in the previous section using SLR. Three main equations (4.2, 4.3 and 4.4) were used for MLR in order to find a relationship between the most effective solar wind parameters [IMF Bz (nT), Vsw (km/s) and AE] and Joule heating rate. Tables 4.11, 4.12 and 4.13 show the details of these equations. On the tables, R-squared refers to the determination coefficient, while b0, b1 and b2 refer to the coefficients of the equation.

$$JH = b_0 + b_1 AE + b_2 IMFBz \ [GW] \tag{4.2}$$

$$JH = b_0 + b_1 IMFBz + b_2 Vsw \ [GW] \tag{4.3}$$

$$JH = b_0 + b_1 AE + b_2 IMFBz + b_3 Vsw \ [GW] \tag{4.4}$$

Table 4.11: Coefficients of the equation 4.2 for Joule heating rates with parameters for ICME, SH, MO regions of CMEs and HSSs.

Number of Event	$JH = b_0 + b_1 AE + b_2 IMFBz$			
	b_0	b_1	b_2	R-Squared
ICME1	-18.78	0.86	2.65	0.67
ICME2	54.76	0.18	-19.16	0.51
ICME3	133.05	0.39	-15.33	0.74
Combined	101.97	0.28	-11.58	0.60
SH1	24.68	0.29	5.25	0.28
SH2	159.29	0.14	2.73	0.14
SH3	436.33	0.13	-7.09	0.04
Combined	223.46	0.04	-17.95	0.37
MO1	404.72	0.32	-7.23	0.70
MO2	-43.49	0.13	-30.77	0.64
MO3	101.52	0.42	-11.91	0.87
Combined	88.36	0.28	-12.11	0.72
HSS1	-0.94	0.35	-3.26	0.49
HSS2	58.32	0.20	-1.63	0.17
HSS3	44.50	0.30	-0.45	0.40
Combined	50.22	0.27	-0.54	0.32

Table 4.12: Coefficients of the equation 4.3 for Joule heating rates with parameters for ICME, SH, MO regions of CMEs and HSSs.

Number of Event	$JH = b_0 + b_1 IMFBz + b_2 Vsw$			
	b_0	b_1	b_2	R-Squared
ICME1	-2109.10	-22.78	5.76	0.42
ICME2	-435.77	-22.82	1.18	0.64
ICME3	-640.80	-25.12	1.16	0.76
Combined	-596.21	-22.07	1.53	0.72
SH1	-65.28	3.07	0.39	0.13
SH2	296.81	0.45	-0.05	0.0004
SH3	-3367.70	-8.90	5.71	0.35
Combined	-1062.50	-13.30	2.1	0.48
MO1	1304.30	-9.47	-1.56	0.65
MO2	-898.42	-11.79	2.4	0.81
MO3	-550.83	-32.79	1.55	0.87
Combined	-707.83	-23.28	1.7	0.85
HSS1	-70.84	-8.49	0.30	0.11
HSS2	24.57	-4.83	0.11	0.04
HSS3	-115.25	-3.99	0.46	0.14
Combined	8.83	-3.12	0.16	0.04

Table 4.13: Coefficients of the equation 4.4 for Joule heating rates with parameters for ICME, SH, MO regions of CMEs and HSSs.

Number of Event	$JH = b_0 + b_1 AE + b_2 IMFBz + b_3 Vsw$				
	b_0	b_1	b_2	b_3	R-Squared
ICME1	-1098.70	0.74	-4.81	2.63	0.71
ICME2	-496.35	0.14	-10.79	1.12	0.66
ICME3	-454.62	0.25	-15.31	1.14	0.80
Combined	-569.67	0.16	-15.63	1.35	0.75
SH1	-198.27	0.30	3.38	0.53	0.29
SH2	-545.18	0.21	1.29	1.06	0.20
SH3	-3482.00	-0.06	-9.21	5.95	0.35
Combined	-1376.10	0.14	-11.37	2.4	0.51
MO1	1153.80	0.32	-3.74	-1.68	0.70
MO2	-911.00	0.06	-10.68	2.37	0.82
MO3	-324.45	0.26	-18.31	0.91	0.91
Combined	-681.92	0.16	-16.41	1.61	0.87
HSS1	26.29	0.36	-3.33	-0.05	0.49
HSS2	24.55	0.19	-2.05	0.06	0.17
HSS3	-31.95	0.27	-0.57	0.16	0.41
Combined	7.95	0.26	-0.55	0.08	0.32

Following the MLR analysis with Equation 4.2, the most influential solar wind parameter for ICME, SH, and MO regions as well as for HSSs is seen to be southward IMF Bz. It can also be seen that for HSSs, the IMFBz and AE contributions are not that far, differently than in CME regions. Also, Equation 4.3 provides the information that the IMFBz contribution is much higher than the solar wind speed contribution for all events. Equation 4.4 also indicates that the highest contribution is from IMFBz when it is southward. The highest determination coefficient (R-squared) values from MLR model are observed within the MO interval of the CMEs for all of the three equations respectively as 0.72, 0.85 and 0.87. Here, the best MLR model includes the solar wind speed, southward interplanetary magnetic field and AE parameters for CME cases and regions. But when the solar wind aspect (Equation 4.10) and solar wind-magnetosphere aspect (Equation 4.11) are investigated, CMEs provide much better correlations with the solar wind side (Equation 4.11). The results of these regression analyses suggest that the CME driven JH events are mostly controlled by the solar wind properties, rather than the magnetospheric processes. For the HSS cases, the best determination coefficient is obtained in Equations 4.2 and 4.4 with the same value of 0.32. The first equation has the contribution from solar wind magnetic field and AE

index while the other equation also has the contribution of solar wind speed. So, it can be concluded that the JH is related with to the magnetospheric responses, as it correlates efficiently with AE, and less correlated with only solar wind parameters. These results also reveal that the Joule heating driven by the CME events mostly depends on solar wind parameters, namely parameters with solar origin and that the Joule heating driven by HSS events mostly depends on the magnetospheric processes and thus refer to the magnetotail reconnection and resulting magnetospheric storms and so as the controlling process. To conclude, Equation 4.4 from the MLR model is suggested for Joule heating estimations based on its high determination coefficient rates for the CME and HSS cases and for all different regions of CME structure. To investigate the solar wind-magnetosphere coupling efficiency, Akasofu (1981) epsilon parameter (Equation 2.2) was used as the energy input, and Joule heating estimated from the SWMF/BATS-R-US model is used as the energy output (dissipated energy form) in order to obtain how much dissipation occured in the form of Joule heating from the solar wind properties of ICME and CIR/HSS structures. Epsilon parameter (GW) was obtained from OMNIWeb and Joule heating (GW) is obtained from the SWMF/BATS-R-US model outputs for each case with 4 min resolutions. Equation 4.5 shows the formula used for the calculation of energy efficiency of Joule heating.

$$\text{Efficiency} = \frac{\text{Energy input}}{\text{Energy output}} \text{x } 100 = \frac{U_{JH_{model}}}{\varepsilon} \text{x}100 \tag{4.5}$$

The efficiency calculations are done for each geomagnetic storm interval driven by each solar phenomenon and the results are presented in Table 4.14.

Table 4.14: Joule heating efficiency for geomagnetic storms driven by each solar phenomena (%).

Number of Event	Efficiency		
	Total JH	Total ε	%
CME1	203913,6	568266,7	35,9
CME 2	327137,9	2158702,4	15,2
CME 3	242243,5	440322,7	55,0
Average CME	257765,0	1055763,9	24,4
HSS 1	167742,2	250396,6	67,0
HSS 2	70727,4	130026,2	54,4
HSS 3	108994,1	131963,8	82,6
Average HSS	115821,2	170795,5	67,8

The table shows that the kinetic energy of the solar wind corresponding to the phenomena was dissipated into the Joule heating form by 24.4% for CME cases, where the efficiency was found 67.8% for HSS cases. This result was an unexpected result throughout the study. Since the CMEs are extremely magnetic structures and they have interplanetary fast forward shocks, it is expected that they put more heating into the ionosphere. But at the same time, even though these events are very intense, here it is showwn that only about ¼ of the CME energy input from this structure was converted into the Joule dissipation within the magnetosphere-ionosphere. On the other hand for the HSS cases, about 2/3 of the energy input from the structure was dissipated as Joule heating. This is a very unexpected result. It is clearly seen that HSS events show 2.77 times more effective energy conversion than CME cases in terms of, but overall they result with less Joule heating rates. These results imply that the most important driver for the solar phenomena; the solar wind-magnetosphere dynamo is playing a great role for Joule heating driven by HSS cases. However, this is not the case for the Joule heating resulting from CME cases.

5. SUMMARY AND CONCLUSIONS

Since the solar wind-magnetosphere dynamo processes affecting the Earth's ionosphere is still not fully understood, the results of this work provide important contributions to the literature. The solar phenomena are the major driving energy source for the Earth's magnetic enviroment. The energy from the Sun dissipates into the magnetosphere-ionosphere system in the form of auroral particle precipitation, ring current injection and most importantly Joule heating. In this study, the two major solar phenomena, i.e. coronal mass ejections and high speed solar wind streams were investigated in order to compare their effects on the magnetic storms and ionospheric consequences using Joule heating. Also, a new contribution in our study involves a statistical investigation of CME and HSS structure, i.e. how different parts of these structures affect the ionospheric Joule heating and its quantification. A thorough investigation of CME and HSS structures, their properties have been carried out in order to first to put forward their statistical properties using 3 cases from each at this time. A quantification of ionospheric Joule heating caused by CME and HSS has been made with respect to storm and substorm phases and the results were compared which is a subject with open questions. The parameters that influence the Joule heating for both solar phenomena were revealed and the dependence of the Joule heating on the controlling parameters has been drived through simple statiscal regression methods which can be used in developing models for the prediction of Joule heating. By performing this study starting from the solar wind properties to magnetospheric disturbances and then to the ionospheric dissipation, it was aimed to track the changes from the Sun until the Earth. This way, this study was aimed to be a unique guiding source for further studies of ionospheric Joule heating predictions from the solar activities by using the controlling parameters depending on the phenomena, and also for both the solar side of the solar wind-magnetosphere coupling as well as the magnetospheric side while filling the gap on the influence of CME and HSS on the ionospheric consequences. This study is built on a large literature search to provide a deep understanding on the origin and evolution solar activities, remote sensing observation and in-situ measurement methods for space weather phenomena, coronal

mass ejection and high speed streams in interplanetary space and their structural differences, geomagnetic storms and their phases, magnetosphere-ionosphere coupling and energy exchange processes, energy dissipation processes and estimation methods of Joule heating and physics-based models as MHD solvers coupling the magnetosphere domain to the ionosphere. Following the construction of the guidebook from the wide range literature research, an elaborative data analysis was performed on a large variety of data sets. The methodology in this study can be explained as it follows; selections of the three CME and three HSS cases through remote sensing observations and in-situ measurements, obtaining the event intervals from criteria and catalogues provided in the literature, running the SWMF/BATS-R-US magnetospheric MHD model with special settings and WIND inputs for each case, obtaining the Joule dissipation from the model for each case, defining the structural boundaries of CME and HSS cases and calculating the Joule heating corresponding to the each structural interval in detail, comparison of the structural (solar wind based) differences with obtained Joule heating, defining the driven geomagnetic storm intervals and phases of CME and HSS cases and calculating the Joule heating corresponding to the each storm interval in detail, performing another comparison of the geomagnetic storm (magnetosphere-ionosphere coupling based) differences with obtained Joule heating, then performing a simple linear regression (SLR) and multi linear regression (MLR) analysis for the structural intervals for the corresponding phenomena to obtain relations between solar wind-geomagnetic activity parameters, deriving Joule heating equations based on the statistical relations obtained from MLR analyses, determining the most controlling parameters for each phenomena and investigating the reason behind the correlations by performing energy efficiency analysis and finally putting out the obtained results in details. Our results obtained from the detailed analysis can be summerized as:

1. For the CME cases, the Joule heating maxima was observed around 1400 GW, and for the HSS cases the maximum observed value during the event was around 800 GW. As a preliminary result, it can be said from the peak values that Joule heating is more intense for CME cases, than the HSS cases.
2. CME events show rapid increases following the CME shock and quick returns to the background values of Joule heating, while HSS events show delayed increases, steady and very slow returns to the background values. This can be

explained by the absence of a shock and the continuous pattern of high speed solar wind streams.

3. Coronal mass ejections were found to drive higher rates of Joule heating per unit time than high speed solar wind streams (CIR/HSS) by a factor of 3.3 for the whole structural interval, even though the durations of the CIR/HSS structures were obtained larger than ICME structures. This can be explained with the fact that ICMEs have a fast forward shock, while CIR/HSS structures do not. Also that the closed magnetic field origin of ICMEs make their structure even stronger, compared with the CIR/HSSs originated from the open magnetic field lines.
4. Coronal mass ejections were found to drive higher Joule heating per unit time for their magnetic obstacle (MO) region, than the sheath (SH) region or the whole interval (ICME). Respectively higher by a factor of 1.10 and 1.02 for SH and ICME intervals. This is associated with the solar wind properties within the MO interval; strong magnetic field, longer duration of southward IMFBz and smooth change in the clock angle while the SH interval is mostly turbulent. It is known that a strong and long duration southward magnetic field is the most effective parameter for solar wind-magnetosphere coupling. Thus, the structure of MO drives higher Joule heating rates.
5. Geomagnetic storms driven by ICMEs were found to result on average with more Joule dissipation than CIR/HSS driven ones, within the full storm interval by a factor of 1.83, even though the CIR/HSS storms were found to last longer in duration. This is mostly explained with the intensity of the storms. The structures that drive more intense geomagnetic storms, also cause more Joule dissipation via magnetosphere-ionosphere coupling processes.
6. During initial, main and recovery phases of ICME-driven geomagnetic storms, the contribution to Joule heating was found higher respectively by a factor of 4.45, 2.04 and 1.07 compared with CIR/HSS-driven geomagnetic storms. The difference for the initial phases is dramatic, that can be explained by the absence of storm sudden commencement caused by an interplanetary shock during the HSS events. The difference during the main phase is also due to the wind-magnetosphere coupling processes, which indicates that ICMEs caused more intense disturbances than CIR/HSSs. Finally, the recovery phase contribution to the Joule heating is similar for both phenomena. The ICME-

driven geomagnetic storm recovery phases are shorter in duration and more intense than CIR/HSS-driven ones. This phase of CIR/HSS storms last longer since there is no clear full recovery, and that fact increases the contribution to the Joule dissipation within the interval. Thus, both phenomena can have similar Joule heating participation during the recovery phases.

7. From the Linear Regression (SLR) analysis, in general it was found that the SH region solar wind and geomagnetic activity parameters of the corresponding CMEs show low to moderate correlations. MO region showed moderate to very high correlations in general. Also the ICME region including SH and MO regions showed low to high correlations. Here, it is found that the MO parts are the most controlling structures within the CMEs, considering the significant correlations.
8. From the Simple Linear Regression (SLR) analysis, it was obtained that the CME structures drive the Joule heating mostly depending on the IMFBz, solar wind speed and AE parameters. These relations explain that the Joule heating driven by CMEs are mostly controlled by the solar wind aspect than magnetospheric processes. Also the solar wind speed had a non-negligible contribution. It matches with the literature showing the contribution of the solar wind to the epsilon parameter (energy budget from solar wind), but it is evident that solar wind speed has a lower contribution compared to the southward magnetic field.
9. From the Linear Regression (SLR) analysis, in general it was also found for the HSS structures that there are very low to moderate correlations with solar wind/geomagnetic activity parameters and Joule heating.
10. From the Simple Linear Regression (SLR) analysis, it was also obtained that the HSS structures drive the Joule heating mostly depending on the AE and Dst parameters. The solar wind speed and IMFBz correlations were observed very low. These relations explain that the Joule heating driven by HSSs are mostly controlled by the magnetospheric processes, rather than the solar wind aspect.
11. Multi Linear Regression (MLR) analyses for all cases that were applied for magnetic field z component, solar wind speed and AE index for CME cases and their structures showed the highest determination coefficients for the equations 4.3 and 4.4, including the most contribution from the solar wind aspect. Where the highest determination coefficients were observed for the

equations 4.2 and 4.4 for the HSS cases and structures, showing the most contribution is from the magnetospheric aspect.

12. For the CME structures, the highest determination coefficients are observed within the MO, SH and then in the full ICME intervals respectively for all equations derived.
13. For the HSS structures, the determination coefficients calculated from the three regression models are found even lower than any CME structure; ICME, SH or MO. That demonstrates that the controlling parameters of Joule heating corresponding to CMEs and HSSs are different and for further studies, it is suggested to use a different set of parameters for HSS cases.
14. For the Joule heating estimations/predictions of corresponding CME structures, equations 5.1, 5.2 and 5.3 were derived for the solar wind aspect.

$$\mathrm{JH_{ICME1}} = -596.21 - 22.07\ \mathrm{IMFBz} + 1.53\ \mathrm{Vsw}\ [\mathrm{GW}] \quad (5.1)$$

$$\mathrm{JH_{SH1}} = -1062.50 - 13.30\ \mathrm{IMFBz} + 2.1\ \mathrm{Vsw}\ [\mathrm{GW}] \quad (5.2)$$

$$\mathrm{JH_{MO1}} = -707.83 - 23.28\ \mathrm{IMFBz} + 1.7\ \mathrm{Vsw}\ [\mathrm{GW}] \quad (5.3)$$

15. On the other hand, equations 5.4, 5.5, 5.6 are derived from the combination of solar wind parameters (solar wind speed and interplanetary magnetic field in z direction) for Joule heating estimation/predictions of corresponding CME structures.

$$\mathrm{JH_{ICME2}} = -596.67 + 0.16\ \mathrm{AE} - 15.63\ \mathrm{IMFBz} + 1.35\ \mathrm{Vsw}\ [\mathrm{GW}] \quad (5.4)$$

$$\mathrm{JH_{SH2}} = -1376.10 + 0.14\ \mathrm{AE} - 11.37\ \mathrm{IMFBz} + 2.4\ \mathrm{Vsw}\ [\mathrm{GW}] \quad (5.5)$$

$$\mathrm{JH_{MO2}} = -681.92 + 0.16\ \mathrm{AE} - 16.41\ \mathrm{IMFBz} + 1.61\ \mathrm{Vsw}\ [\mathrm{GW}] \quad (5.6)$$

16. For the HSS structure, equations 5.7 and 5.8 are derived from the solar wind parameters and also from the combination of solar wind and magnetic activity parameters that can be used as well for the estimation of Joule heating driven by HSS structures with the highest determination coefficient values. In other

words, Joule heating is depending mostly on the geomagnetic activity, AE index, for the HSS cases and also IMFBz as a solar wind parameter.

$$JH_{HSS1} = 50.22 + 0.27\ AE - 0.54\ IMFBz\ [GW] \quad (5.7)$$

$$JH_{HSS2} = 7.95 + 0.26\ AE - 0.55\ IMFBz + 0.08\ Vsw\ [GW] \quad (5.8)$$

17. From the equations derived from MLR analyses of CME cases, it was found that the IMFBz is the most contributing parameter, followed by solar wind speed and AE index. The negative coefficient of IMFBz means that when the IMFBz is the most southward, it will increase the JH rate in the ionosphere the most, compared to other parameters. Also solar wind speed is the second most important parameter compared with the AE index. This result is evidence that the solar wind side of the phenomena is more effective to drive Joule heating, than the magnetospheric processes and their contributions for the CME cases.
18. From the equations derived from MLR analyses of HSSs, the highest coefficient was found in IMFBz and AE parameters. But their coefficient contributions were not that distinctive as in CME coefficients. The AE index contribution here poses a greater importance than in CME cases. Also the contribution of the solar wind is found extremely low. This result is evidence that the magnetospheric processes are more effective to drive Joule heating, than the solar wind properties of the HSS.
19. The higher contribution of solar wind speed for the CME cases, compared with HSS cases, even though their speed were similar, shows that the coronal mass ejection speed is more important than “high speed” of the solar wind streams for their contribution to the Joule heating rates. Also the jumps (shock) in CME cases rather than the steady increases in the speeds in HSS cases can be the reason for this difference. Further studies should investigate their speed and Joule heating relations.
20. Overall, the most consistent regression models were found as 5.4, 5.5, 5.6 for CME structures and 5.8 for HSS structures according to their highest determination coefficients calculated respectively as 0.75, 0.51, 0.87 and 0.32. This set of equations can be improved in the further studies in order to predict Joule heating.

21. The efficiency is investigated for CME and HSS structures during their storm intervals, in order to figure out which phenomena is more effective. By comparing the solar wind energy input (epsilon) to the ionospheric Joule dissipation (model) as an energy sink, it is observed that averagely 67.8% of the energy is dissipated in the form of Joule heating during HSS-driven storms, where only %24.4 of it is deposited as Joule heating during CME-driven storms. It can be said that the dissipation in the form of Joule heating occurs 2.77 times more during HSS driven storms than during CME driven storms.
22. The efficiency rates explain that even though CME-driven storms have higher Joule dissipation effect, they are not as efficient as HSS-driven ones. Since the epsilon parameter does just include solar wind input and epsilon values calculated during HSS-driven storms are smaller compared to Joule heating (which causes higher efficiency), that justifies our result. HSS driven Joule heating is mostly affected by magnetospheric processes rather than solar wind properties. So, even though «high speed streams» are high speed phenomena, their energy budget is 6.18 times smaller than CMEs, with less intense geomagnetic storms among all phases and also 2.22 times less heating rate within the geomagnetic storm interval compared to CMEs. But they convert the kinetic energy to heating 2.77 times more than CMEs, more efficiently.

REFERENCES

Ahn, B.-H., Akasofu, S.-I., & Kamide, Y. (1983). The Joule heat production rate and the particle energy injection rate as a function of the geomagnetic indices AE and AL. *Journal of Geophysical Research*, *88*(A8), 6275. doi: https://doi.org/10.1029/ja088ia08p06275

Aikio, A. T., & Selkälä, A. (2009). Statistical properties of Joule heating rate, electric field and conductances at high latitudes. *Annales Geophysicae*, *27*(7), 2661–2673. doi: 10.5194/angeo-27-2661-2009

Akasofu, S.-I. (1981). Energy coupling between the solar wind and the magnetosphere. *Space Science Reviews*, *28*(2). doi: 10.1007/bf00218810

Badruddin,--. (2002). Study of the effectiveness of various solar wind parameters in the development of geomagnetic storms during interplanetary events. *Turkish Journal of Physics: 26*(5), 391-402. doi: 10.3906/fiz-0203-3

Baker, D. N., Turner, N. E., & Pulkkinen, T. I. (2001). Energy transport and dissipation in the magnetosphere during geomagnetic storms. *Journal of Atmospheric and Solar-Terrestrial Physics*, *63*(5), 421–429. doi: 10.1016/s1364-6826(00)00169-3

Beaujardiere, O., Johnson, R., & Wickwar, V. B. (1989). Ground-Based Measurements of Joule Heating Rates (Report No. 1). Massachusetts : Air Force Geophysics Laboratory Report.

Borovsky, J. E., & Denton, M. H. (2006). Differences between CME-driven storms and CIR-driven storms. *Journal of Geophysical Research*, *111*(A7). doi: 10.1029/2005ja011447

Brueckner, G. E., Howard, R. A., Koomen, M. J., Korendyke, C. M., Michels, D. J., Moses, J. D., Socker, D. G., Dere, K. P., Lamy, P. L., Llebaria, A., Bout, M. V., Schwenn, R., Simnett, G. M., Bedford, D. K., & Eyles, C. J. (1995). The Large Angle Spectroscopic Coronagraph (LASCO): Visible light coronal imaging and spectroscopy. *Solar Physics*, *162*(1–2), 357–402. doi: 10.1007/bf00733434

Burkepile, J. T., & St. Cyr, O. C. (1993). *A revised and expanded catalogue of mass ejections observed by the Solar Maximum Mission coronagraph*. Retrieved from: https://ui.adsabs.harvard.edu/abs/1993STIN...9326556B/abstract

Burlaga, L., Sittler, E., Mariani, F., & Schwenn, R. (1981). Magnetic loop behind an interplanetary shock: Voyager, Helios, and IMP 8 observations. *Journal of Geophysical Research*, *86*(A8), 6673. doi: 10.1029/ja086ia08p06673

CDAWeb. (2010,2013). WIND magnetic field and solar wind data. [Data file] Retrieved from ftp://spdf.gsfc.nasa. gov/pub/data/omni/omni_cdaweb/

Chen, G.-M., Xu, J., Wang, W., & Burns, A. G. (2014). A comparison of the effects of CIR- and CME-induced geomagnetic activity on thermospheric densities and spacecraft orbits: Statistical studies: STATISTICAL STORM EFFECTS ON ORBITS. *Journal of Geophysical Research. Space Physics*, *119*(9), 7928–7939. doi: 10.1002/2014ja019831

Cole, K. D. (1962). Joule heating of the upper atmosphere. *Australian Journal of Physics*, *15*(2), 223. doi: 10.1071/ph620223

Cranmer, S. R. (2002). Coronal Holes and the High-Speed Solar Wind. *Space Science Reviews*, *101*(3/4), 229–294. doi: 10.1023/a:1020840004535

European Space Agency. (n.d.). *Space weather and its hazards.* Retrieved from https://www.esa.int/Safety_Security/Space_weather_and_its_hazards3

Fitzpatrick, R. (2011). *Ring Current*. Retrieved from: https://farside.ph.utexas.edu/teaching/plasma/lectures/node23.html

Garton, T. M., Gallagher, P. T., & Murray, S. A. (2017). Automated Coronal Hole Identification via multi-thermal intensity segmentation. In *arXiv [astro-ph.SR]*. Retrieved from: http://arxiv.org/abs/1711.11476

Gerontidou, M., Mavromichalaki, H., & Daglis, T. (2018). High-speed solar wind streams and geomagnetic storms during solar cycle 24. *Solar Physics*, *293*(9). doi: 10.1007/s11207-018-1348-8

Gombosi, T. I., Chen, Y., Glocer, A., Huang, Z., Jia, X., Liemohn, M. W., Manchester, W. B., Pulkkinen, T., Sachdeva, N., Al Shidi, Q., Sokolov, I. V., Szente, J., Tenishev, V., Toth, G., van der Holst, B., Welling, D. T., Zhao, L., & Zou, S. (2021). What sustained multi-disciplinary research can achieve: The space weather modeling framework. *Journal of Space Weather and Space Climate*, *11*, 42. doi: 10.1051/swsc/2021020

Gombosi, T. I., De Zeeuw, D. L., Powell, K. G., Ridley, A. J., Sokolov, I. V., Stout, Q. F., & Tóth, G. (2003). Adaptive mesh refinement for global magnetohydrodynamic simulation. In *Lecture Notes in Physics* (pp. 247–274). Springer Berlin Heidelberg.

Gonzalez, W. D., Joselyn, J. A., Kamide, Y., Kroehl, H. W., Rostoker, G., Tsurutani, B. T., & Vasyliunas, V. M. (1994). What is a geomagnetic storm? *Journal of Geophysical Research*, *99*(A4), 5771. doi: 10.1029/93ja02867

Gonzalez, W. D., Tsurutani, B. T., & Clúa de Gonzalez, A. L. (1999). *Space Science Reviews*, *88*(3/4), 529–562. doi: 10.1023/a:1005160129098

Gopalswamy, N. (2003). Coronal mass ejections: Initiation and detection. *Advances in Space Research: The Official Journal of the Committee on Space Research (COSPAR)*, *31*(4), 869–881. doi: 10.1016/s0273-1177(02)00888-8

Gopalswamy, N. (2007). Properties of interplanetary coronal mass ejections. *Space Science Reviews*, *124*(1–4), 145–168. doi: 10.1007/s11214-006-9102-1

Gopalswamy, N. (2008). Solar connections of geoeffective magnetic structures. *Journal of Atmospheric and Solar-Terrestrial Physics*, *70*(17), 2078–2100. doi: 10.1016/j.jastp.2008.06.010

Gopalswamy, N. (2009). Halo coronal mass ejections and geomagnetic storms. *Earth, Planets, and Space: EPS*, *61*(5), 595–597. doi: 10.1186/bf03352930

Gopalswamy, N., Yashiro, S., & Akiyama, S. (2007). Geoeffectiveness of halo coronal mass ejections: GEOEFFECTIVENESS OF HALO CMES. *Journal of Geophysical Research*, *112*(A6). doi: 10.1029/2006ja012149

Gopalswamy, N., Yashiro, S., Michalek, G., Stenborg, G., Vourlidas, A., Freeland, S., & Howard, R. (2009). The SOHO/LASCO CME catalog. Earth, Moon, and Planets, *104*(1–4), 295–313. doi: 10.1007/s11038-008-9282-7

Gopalswamy, N., Yashiro, S., Michalek, G., Xie, H., Lepping, R. P., & Howard, R. A. (2005). Solar source of the largest geomagnetic storm of cycle 23: LARGEST MAGNETIC STORM OF CYCLE 23. *Geophysical Research Letters*, *32*(12). doi: 10.1029/2004gl021639

Gosling, J. T. (1993). Coronal mass ejections: The link between solar and geomagnetic activity. *Physics of Fluids*, *5*(7), 2638–2645. doi: 10.1063/1.860701

Gosling, J. T., Bame, S. J., McComas, D. J., & Phillips, J. L. (1990). Coronal mass ejections and large geomagnetic storms. *Geophysical Research Letters*, *17*(7), 901–904. doi: 10.1029/gl017i007p00901

Hosteaux, S., Chané, E., & Poedts, S. (2019). Effect of the solar wind density on the evolution of normal and inverse coronal mass ejections. *Astronomy and Astrophysics*, *632*, A89. doi: 10.1051/0004-6361/201935894

Hudson, H. S., Bougeret, J.-L., & Burkepile, J. (2006). Coronal mass ejections: Overview of observations. *Space Science Reviews*, *123*(1–3), 13–30. doi: 10.1007/s11214-006-9009-x

Hundhausen, A. J., Burkepile, J. T., & St. Cyr, O. C. (1994). Speeds of coronal mass ejections: SMM observations from 1980 and 1984-1989. *Journal of Geophysical Research*, *99*(A4), 6543. doi: 10.1029/93ja03586

Hundhausen, A. J., Sawyer, C. B., House, L., Illing, R. M. E., & Wagner, W. J. (1984). Coronal mass ejections observed during the Solar Maximum Mission: Latitude distribution and rate of occurrence. *Journal of Geophysical Research*, *89*(A5), 2639. doi: 10.1029/ja089ia05p02639

Illing, R. M. E., & Hundhausen, A. J. (1985). Observation of a coronal transient from 1.2 to 6 solar radii. *Journal of Geophysical Research*, *90*(A1), 275–282. doi: 10.1029/ja090ia01p00275

Kalafatoglu Eyiguler, E. C., Kaymaz, Z., Frissell, N. A., Ruohoniemi, J. M., & Rastätter, L. (2018). Investigating upper atmospheric joule heating using cross-combination of data for two moderate substorm cases. *Space Weather: The International Journal of Research & Applications*, *16*(8), 987–1012. doi: 10.1029/2018sw001956

Kataoka, R., & Miyoshi, Y. (2006). Flux enhancement of radiation belt electrons during geomagnetic storms driven by coronal mass ejections and corotating interaction regions: RADIATION BELT DURING

CME/CIR STORMS. *Space Weather: The International Journal of Research & Applications*, *4*(9). doi: 10.1029/2005sw000211

Kavanagh, A., & Denton, M. (2007). High-speed solar-wind streams and geospace interactions. *Astronomy & Geophysics*, *48*(6), 24-26. doi:10.1111/j.1468-4004.2007.48624.x

Kilpua, E., Koskinen, H. E. J., & Pulkkinen, T. I. (2017). Coronal mass ejections and their sheath regions in interplanetary space. *Living Reviews in Solar Physics*, *14*(1), 5. doi: 10.1007/s41116-017-0009-6

Kosch, M. J., & Nielsen, E. (1995). Coherent radar estimates of average high-latitude ionospheric Joule heating. *Journal of Geophysical Research*, *100*(A7), 12201. doi: 10.1029/95ja00821

Koskinen, H. E. J., & Tanskanen, E. I. (2002). Magnetospheric energy budget and the epsilon parameter. *Journal of Geophysical Research*, *107*(A11). doi: 10.1029/2002ja009283

Kumar, S., & Singh, A. K. (2011). Storm time response of GPS-derived total electron content (TEC) during low solar active period at Indian low latitude station Varanasi. *Astrophysics and Space Science*, *331*(2), 447–458. doi: 10.1007/s10509-010-0459-y

Lepping, R. P., Jones, J. A., & Burlaga, L. F. (1990). Magnetic field structure of interplanetary magnetic clouds at 1 AU. *Journal of Geophysical Research*, *95*(A8), 11957. doi: 10.1029/ja095ia08p11957

Lepping, R. P., Wu, C.-C., & Berdichevsky, D. B. (2005). Automatic identification of magnetic clouds and cloud-like regions at 1 AU: occurrence rate and other properties. *Annales Geophysicae*, *23*(7), 2687–2704. doi: 10.5194/angeo-23-2687-2005

Li, W., Knipp, D., Lei, J., & Raeder, J. (2011). The relation between dayside local Poynting flux enhancement and cusp reconnection: POYNTING FLUX ENHANCEMENT. *Journal of Geophysical Research*, *116*(A8). doi: 10.1029/2011ja016566

Loewe, C. A., & Prölss, G. W. (1997). Classification and mean behavior of magnetic storms. *Journal of Geophysical Research*, *102*(A7), 14209–14213. doi: 10.1029/96ja04020

Lu, G. (2006). High-speed streams, coronal mass ejections, and interplanetary shocks: A comparative study of geoeffectiveness. In *Recurrent Magnetic Storms: Corotating Solar Wind Streams* (pp. 97–111). American Geophysical Union.

Lu, G., Baker, D. N., McPherron, R. L., Farrugia, C. J., Lummerzheim, D., Ruohoniemi, J. M., Rich, F. J., Evans, D. S., Lepping, R. P., Brittnacher, M., Li, X., Greenwald, R., Sofko, G., Villain, J., Lester, M., Thayer, J., Moretto, T., Milling, D., Troshichev, O., … Hayashi, K. (1998). Global energy deposition during the January 1997 magnetic cloud event. *Journal of Geophysical Research*, *103*(A6), 11685–11694. doi: 10.1029/98ja00897

Mac-Mahon, R. M., & Gonzalez, W. D. (1997). Energetics during the main phase of geomagnetic superstorms. *Journal of Geophysical Research*, *102*(A7), 14199–14207. doi: 10.1029/97ja01151

Mavromichalaki, H., & Vassilaki, A. (1998). Fast Plasma Streams Recorded Near the Earth During 1985–1996. *Solar Physics*, *183*(1), 181–200. doi: 10.1023/a:1005004328071

Mavromichalaki, H., Vassilaki, A., & Marmatsouri, E. (1988). A catalogue of high-speed solar-wind streams: Further evidence of their relationship to Ap-index. *Solar Physics*, *115*(2), 345–365. doi: 10.1007/bf00148733

Mishra, A. P., & Tripath, R. (1996, February 19-24). *ILWS WORKSHOP:* Characteristic features of coronal mass ejections and their effect on geomagnetosphere [Pdf]. Retrieved from: https://cdaw.gsfc.nasa.gov/publications/ilws_goa2006/091_Mishra.pdf

Moestl, C., Bailey, R. L., Reiss, M., & Weiss, A. (2020). Helio4Cast SIRCAT 1.0 for solar wind stream interaction regions and high speed streams (Wind, STEREO, MAVEN). figshare. [Data file]. doi: 10.6084/m9.figshare.12416906.v2

National Aeronautics and Space Administration. (n.d.). *Sunspots and solar flares.* Retrieved from https://spaceplace.nasa.gov/solar-activity/en/

National Aeronautics and Space Administration. (n.d.). *SWMF*. Retrieved from https://ccmc.gsfc.nasa.gov/models/SWMF~20180525/

National Oceanic and Atmospheric Administration. (n.d.). *Coronal mass ejections.* Retrieved from https://www.swpc.noaa.gov/phenomena/coronal-mass-ejections

National Oceanic and Atmospheric Administration. (n.d.). *Geomagnetic storms.* Retrieved from https://www.swpc.noaa.gov/phenomena/geomagnetic-storms

National Oceanic and Atmospheric Administration. (n.d.). *NOAA Space Weather Scales.* Retrieved from https://www.swpc.noaa.gov/noaa-scales-explanation

National Oceanic and Atmospheric Administration. (n.d.). *Planetary K-index.* Retrieved from https://www.swpc.noaa.gov/products/planetary-k-index

National Oceanic and Atmospheric Administration. (n.d.). *The disturbance storm time index.* Retrieved from https://www.ngdc.noaa.gov/stp/geomag/dst.html

Ni, B., Thorne, R. M., Zhang, X., Bortnik, J., Pu, Z., Xie, L., Hu, Z.-J., Han, D., Shi, R., Zhou, C., & Gu, X. (2016). Origins of the earth's diffuse auroral precipitation. *Space Science Reviews*, *200*(1–4), 205–259. doi: 10.1007/s11214-016-0234-7

Nieves-Chinchilla, T., Vourlidas, A., Raymond, J. C., Linton, M. G., Al-haddad, N., Savani, N. P., Szabo, A., & Hidalgo, M. A. (2018). Understanding the internal magnetic field configurations of ICMEs using more than 20 years of wind observations. *Solar Physics*, *293*(2). doi: 10.1007/s11207-018-1247-z

Nieves-Chinchilla, Teresa, Jian, L. K., Balmaceda, L., Vourlidas, A., dos Santos, L. F. G., & Szabo, A. (2019). Unraveling the internal magnetic field structure of the earth-directed interplanetary coronal mass ejections during 1995 – 2015. *Solar Physics*, *294*(7). doi: 10.1007/s11207-019-1477-8

Olsson, A., Janhunen, P., Karlsson, T., Ivchenko, N., & Blomberg, L. G. (2004). Statistics of Joule heating in the auroral zone and polar cap using Astrid-2 satellite Poynting flux. *Annales Geophysicae*, *22*(12), 4133–4142. doi: 10.5194/angeo-22-4133-2004

Oner, K., Ceren, E., & Kaymaz, Z. (2011). Spatial variation of Joule heating and its relationship with the motion of polar cap boundary. *Proceedings of 5th International Conference on Recent Advances in Space Technologies - RAST2011*.

Østgaard, N. (2002). Energy analysis of substorms based on remote sensing techniques, solar wind measurements, and geomagnetic indices. *Journal of Geophysical Research*, *107*(A9). doi: 10.1029/2001ja002002

Palmroth, M., Janhunen, P., Pulkkinen, T. I., & Koskinen, H. E. J. (2004). Ionospheric energy input as a function of solar wind parameters: global MHD simulation results. *Annales Geophysicae*, *22*(2), 549–566. doi: 10.5194/angeo-22-549-2004

Palmroth, M., Janhunen, P., Pulkkinen, T. I., Aksnes, A., Lu, G., Østgaard, N., Watermann, J., Reeves, G. D., & Germany, G. A. (2005). Assessment of ionospheric Joule heating by GUMICS-4 MHD simulation, AMIE, and satellite-based statistics: towards a synthesis. *Annales Geophysicae*, *23*(6), 2051–2068. doi: 10.5194/angeo-23-2051-2005

Papitashvili, N. E. and King, J. H. (2020). OMNI 1-min Data" [Epsilon, 2010-2013], NASA Space Physics Data Facility, doi: 10.48322/45bb-8792

Partamies, N., Juusola, L., Tanskanen, E., & Kauristie, K. (2013). Statistical properties of substorms during different storm and solar cycle phases. *Annales Geophysicae*, *31*(2), 349–358. doi: 10.5194/angeo-31-349-2013

Powell, K. G., Roe, P. L., Linde, T. J., Gombosi, T. I., & De Zeeuw, D. L. (1999). A solution-adaptive upwind scheme for ideal magnetohydrodynamics. *Journal of Computational Physics*, *154*(2), 284–309. doi: 10.1006/jcph.1999.6299

Pradhan, S. M., & Singh, K. (1979). Computation of Joule dissipation in the ionosphere. *Indian Journal of Radio & Space Physics 8*(3), 97-100. Taken from: http://nopr.niscair.res.in/handle/123456789/37085

Pulkkinen, T. I., Ganushkina, N. Y., Kallio, E. I., Lu, G., Baker, D. N., Turner, N. E., Fritz, T. A., Fennell, J. F., & Roeder, J. (2002). Energy dissipation during a geomagnetic storm: May 1998. *Advances in Space Research: The Official Journal of the Committee on Space Research (COSPAR)*, *30*(10), 2231–2240. doi: 10.1016/s0273-1177(02)80232-0

Rastätter, L., Shim, J. S., Kuznetsova, M. M., Kilcommons, L. M., Knipp, D. J., Codrescu, M., Fuller-Rowell, T., Emery, B., Weimer, D. R., Cosgrove, R., Wiltberger, M., Raeder, J., Li, W., Tóth, G., & Welling, D. (2016). GEM-CEDAR challenge: Poynting flux at DMSP and modeled Joule heat. *Space Weather: The International Journal of Research & Applications*, *14*(2), 113–135. doi: 10.1002/2015sw001238

Rathore, B. S., Gupta, D. C., & Parashar, K. K. (2014). Relation between solar wind parameter and geomagnetic sorm condition during cycle-23. In *International Journal of Geosciences 05*(13), 1602–1608. doi: 10.4236/ijg.2014.513131

Richmond, A. D. (1992). Assimilative mapping of ionospheric electrodynamics. *Advances in Space Research: The Official Journal of the Committee on Space Research (COSPAR)*, *12*(6), 59–68. doi: 10.1016/0273-1177(92)90040-5

Richmond, A. D. (2021). Joule Heating in the Thermosphere. In *Upper Atmosphere Dynamics and Energetics* (pp. 1–18). Wiley. doi: 10.1002/9781119815631.ch1

Richmond, A. D., & Kamide, Y. (1988). Mapping electrodynamic features of the high-latitude ionosphere from localized observations: Technique. *Journal of Geophysical Research*, *93*(A6), 5741. doi: 10.1029/ja093ia06p05741

Robinson, R. M., & Zanetti, L. J. (2021). Auroral energy flux and Joule heating derived from global maps of field-aligned currents. *Geophysical Research Letters*, *48*(7), e2020GL091527. doi: 10.1029/2020GL091527

Rodger, A. S., Wells, G. D., Moffett, R. J., & Bailey, G. J. (2001). The variability of Joule heating, and its effects on the ionosphere and thermosphere. *Annales Geophysicae*, *19*(7), 773–781. doi: 10.5194/angeo-19-773-2001

Russian Geomagnetic Database. (n.d.). *Frictional/Joule heating.* Retrieved from magbase.rss.ru/REFMAN/SPPHTEXT/frcton.html

Salice, J. A. (2020). *Solar wind drivers of energetic electron precipitation* [Master's thesis, University of Bergen]. Bergen Open Research Archive. Retrieved from https://hdl.handle.net/1956/23139

SILSO World Data Center. (1920, 2022). Total sunspot number. [Data file] Retrieved from http://www.sidc.be/SILSO/

Solar and Heliospheric Observatory. (2012, 2013). Coronagraph images [Image]. Retrieved from https://soho.nascom.nasa.gov/data/Theater/

Solar Dynamics Observatory. (2010, 2011). AIA, HMI, and EVE images [Image]. Retrieved from https://sdo.gsfc.nasa.gov/data/aiahmi/

Space Weather Services. (n.d.). *What is a Coronal Hole?*. Retrieved from https://www.sws.bom.gov.au/Educational/2/1/5

Strangeway, R. J. (2012). The equivalence of Joule dissipation and frictional heating in the collisional ionosphere: JOULE DISSIPATION AND

FRICTIONAL HEATING. *Journal of Geophysical Research, 117*(A2). doi: 10.1029/2011ja017302

Suess, S. T., & Tsurutani, B. T. (2003). SOLAR WINDS. In *Encyclopedia of Atmospheric Sciences* (pp. 2078–2085). Elsevier.

Sugiura, M. (1986, June 1). *Thermosphere Dynamics Workshop, Volume 2:* Characteristic Joule heating and field-aligned currents: Preliminary results from DE-2 [Pdf]. Retrieved from: https://ntrs.nasa.gov/citations/19860019864

Syun-Ichi, A. (2018). A review of the current understanding in the study of geomagnetic storms. *International Journal of Earth Science and Geophysics*, *4*(1), 1–13. doi: 10.35840/2631-5033/1818

Temmer, M., Reiss, M. A., Nikolic, L., Hofmeister, S. J., & Veronig, A. M. (2017). Preconditioning of interplanetary space due to transient CME disturbances. *The Astrophysical Journal*, *835*(2), 141. doi: 10.3847/1538-4357/835/2/141

Tenfjord, P., & Østgaard, N. (2013). Energy transfer and flow in the solar wind-magnetosphere-ionosphere system: A new coupling function: ENERGY TRANSFER AND FLOW. *Journal of Geophysical Research. Space Physics, 118*(9), 5659–5672. doi: 10.1002/jgra.50545

The University of New Hampshire Coronal Mass Ejection Group. (n.d.). *In situ measurements of CMEs*. Retrieved from https://eos.unh.edu/CMEGroup/research/situ-measurements-cmes

Tóth, G., Sokolov, I. V., Gombosi, T. I., Chesney, D. R., Clauer, C. R., De Zeeuw, D. L., Hansen, K. C., Kane, K. J., Manchester, W. B., Oehmke, R. C., Powell, K. G., Ridley, A. J., Roussev, I. I., Stout, Q. F., Volberg, O., Wolf, R. A., Sazykin, S., Chan, A., Yu, B., & Kóta, J. (2005). Space Weather Modeling Framework: A new tool for the space science community. *Journal of Geophysical Research*, *110*(A12). doi: 10.1029/2005ja011126

Tsurutani, B. T., & Gonzalez, W. D. (1997). The interplanetary causes of magnetic storms: A review. In *Magnetic Storms* (pp. 77–89). American Geophysical Union. doi: 10.1029/GM098p0077

Tsurutani, B. T., Gonzalez, W. D., Gonzalez, A. L. C., Guarnieri, F. L., Gopalswamy, N., Grande, M., Kamide, Y., Kasahara, Y., Lu, G., Mann, I., McPherron, R., Soraas, F., & Vasyliunas, V. (2006). Corotating solar wind streams and recurrent geomagnetic activity: A review. *Journal of Geophysical Research*, *111*(A7). doi: 10.1029/2005ja011273

Tsurutani, B. T., Gonzalez, W. D., Gonzalez, A. L. C., Tang, F., Arballo, J. K., & Okada, M. (1995). Interplanetary origin of geomagnetic activity in the declining phase of the solar cycle. *Journal of Geophysical Research, 100*(A11), 21717–21733. doi: 10.1029/95ja01476

Turner, N. E., Cramer, W. D., Earles, S. K., & Emery, B. A. (2009). Geoefficiency and energy partitioning in CIR-driven and CME-driven storms. *Journal*

of Atmospheric and Solar-Terrestrial Physics, *71*(10–11), 1023–1031. doi: 10.1016/j.jastp.2009.02.005

University Corporation for Atmospheric Research. (n.d.). *Sunspots.* Retrieved from https://scied.ucar.edu/learning-zone/sun-space-weather/sunspots

Vasyliūnas, V. M. (2005). Meaning of ionospheric Joule heating. *Journal of Geophysical Research, 110*(A2). doi: 10.1029/2004ja010615

Verbanac, G., Vršnak, B., Veronig, A., & Temmer, M. (2011). Equatorial coronal holes, solar wind high-speed streams, and their geoeffectiveness. *Astronomy and Astrophysics, 526,* A20. doi: 10.1051/0004-6361/201014617

Verbanac, G., Živković, S., Vršnak, B., Bandić, M., & Hojsak, T. (2013). Comparison of geoeffectiveness of coronal mass ejections and corotating interaction regions. *Astronomy and Astrophysics, 558,* A85. doi: 10.1051/0004-6361/201220417

Vickrey, J. F., Vondrak, R. R., & Matthews, S. J. (1982). Energy deposition by precipitating particles and Joule dissipation in the auroral ionosphere. *Journal of Geophysical Research, 87*(A7), 5184–5196. doi: 10.1029/ja087ia07p05184

Webb, D. F., & Howard, T. A. (2012). Coronal mass ejections: Observations. *Living Reviews in Solar Physics*, *9*(1), 1–83. doi: 10.12942/lrsp-2012-3

Weimer, D. R. (2005). Improved ionospheric electrodynamic models and application to calculating Joule heating rates. *Journal of Geophysical Research, 110*(A5). doi: 10.1029/2004ja010884

World Data Center for Geomagnetism, Kyoto, Nose, M., Iyemori, T., Sugiura, M., & Kamei, T (2015). Geomagnetic AE index. doi:10.17593/15031-54800

World Data Center for Geomagnetism, Kyoto, Nose, M., Iyemori, T., Sugiura, M., & Kamei, T. (2015), Geomagnetic Dst index. doi:10.17593/14515-74000.

World Data Center for Geomagnetism. (n.d.). *On AE index.* Retrieved from https://wdc.kugi.kyoto-u.ac.jp/aedir/ae2/onAEindex.html

World Data Center for Geomagnetism. (n.d.). *On Dst index.* Retrieved from https://wdc.kugi.kyoto-u.ac.jp/dstdir/dst2/onDstindex.html

World Meteorological Organization. (n.d.). *Space weather, extending the borders beyond the Earth.* Retrieved from https://public.wmo.int/en/resources/bulletin/space-weather-extending-borders-beyond-earth

World Meteorological Organization. (n.d.). *Space weather.* Retrieved from https://communty.wmo.nt/actvty-areas/avaton/hazards/space-weather

Xystouris, G., Sigala, E., & Mavromichalaki, H. (2014). A complete catalogue of high-speed solar wind streams during solar cycle 23. *Solar Physics*, *289*(3), 995–1012. doi: 10.1007/s11207-013-0355-z

Younas, W., Amory-Mazaudier, C., Khan, M., & Le Huy, M. (2021). Magnetic signatures of ionospheric disturbance dynamo for CME and HSSWs

generated storms. *Space Weather: The International Journal of Research & Applications*, *19*(9). doi: 10.1029/2021sw002825

Zhang, J., Dere, K. P., Howard, R. A., & Bothmer, V. (2003). Identification of solar sources of major geomagnetic storms between 1996 and 2000. *The Astrophysical Journal*, *582*(1), 520–533. doi: 10.1086/344611

Zhang, X. X., Wang, C., Chen, T., Wang, Y. L., Tan, A., Wu, T. S., Germany, G. A., & Wang, W. (2005). Global patterns of Joule heating in the high-latitude ionosphere. *Journal of Geophysical Research*, *110*(A12). doi: 10.1029/2005ja011222

Zirker, J. B. (1977). Coronal holes and high-speed wind streams. *Reviews of Geophysics (Washington, D.C.: 1985)*, *15*(3), 257. doi: 10.1029/rg015i003p00257

APPENDICES

APPENDIX A: Time series of JH with 9 parameters for corresponding the interval of CME 1, CME 2 and CME 3

APPENDIX B: Time series of JH with 9 parameters for corresponding the interval of HSS 1, HSS 2 and HSS 3

APPENDIX C: SLR analysis of JH with 9 parameters for corresponding intervals of CME 1 (ICME, SH, MO)

APPENDIX D: SLR analysis of JH with 9 parameters for corresponding intervals of CME 3 (ICME, SH, MO)

APPENDIX E: SLR analysis of JH with 9 parameters for corresponding intervals of HSS 1 and HSS 3

APPENDIX A

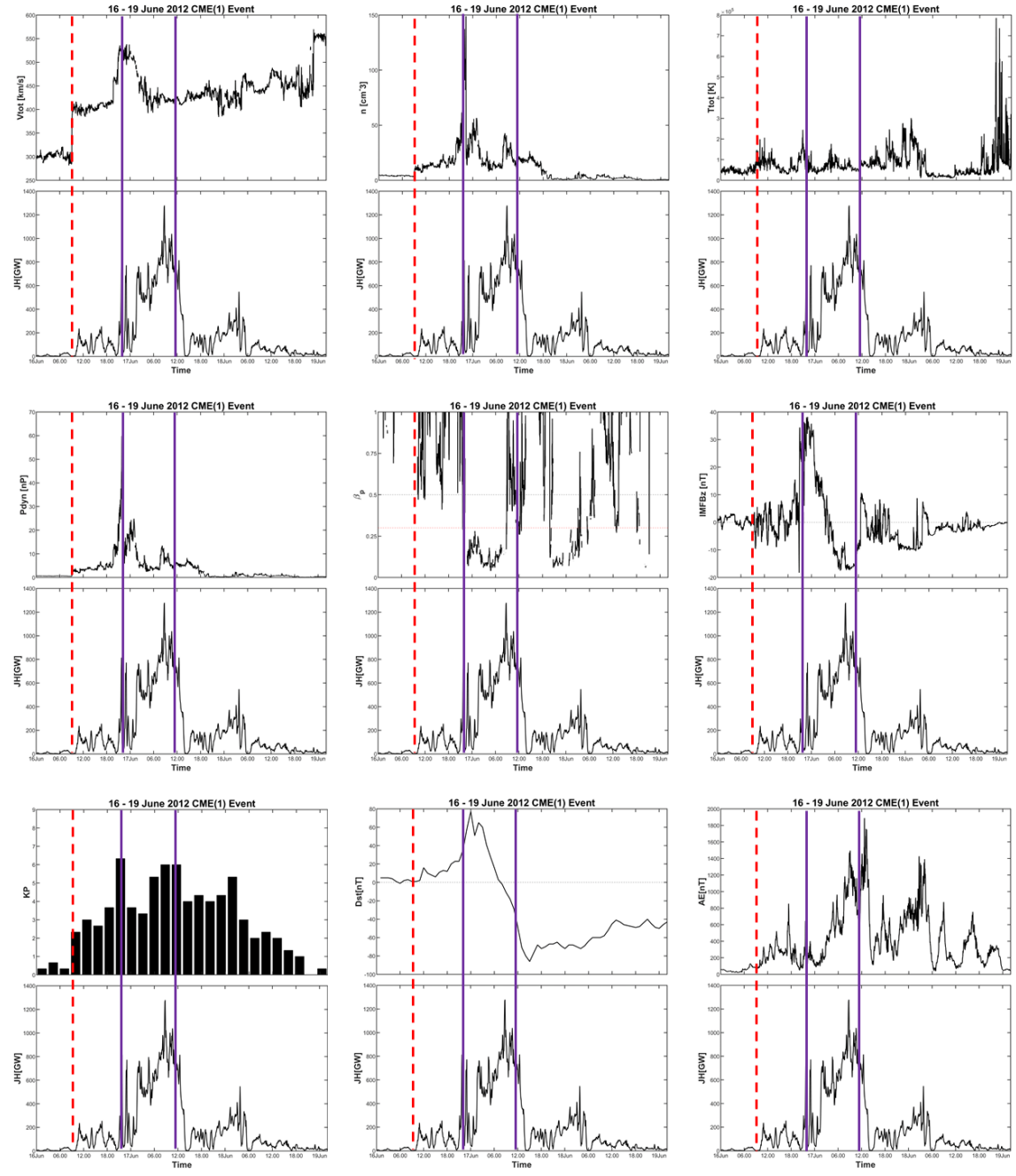

Figure A.1 : Time series of JH with 9 parameters for CME 1, in which the red dashed line represents the shock, and the purple solid lines represent the magnetic obstacle start and end times.

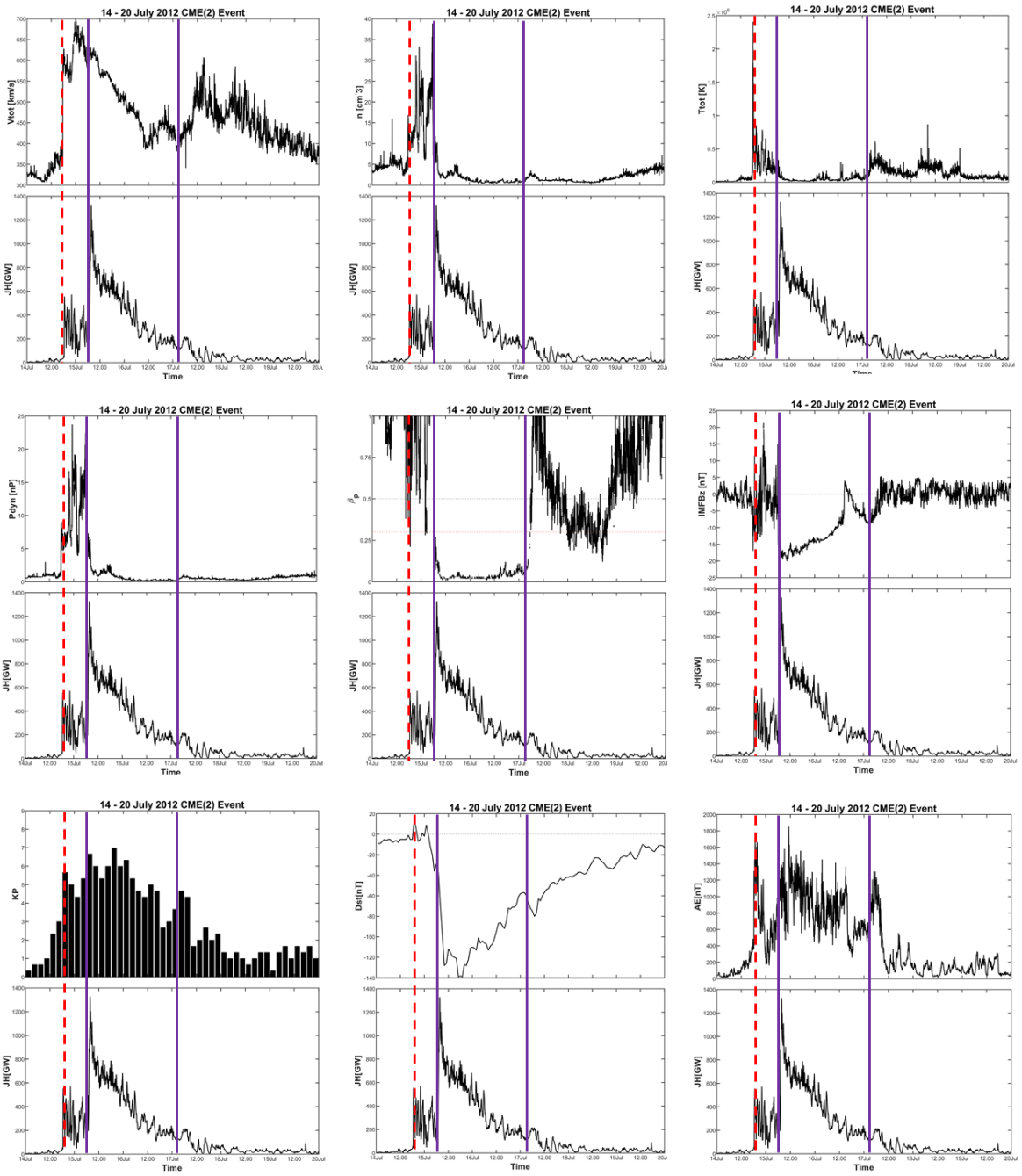

Figure A.2 : Time series of JH with 9 parameters for CME 2, in which the red dashed line represents the shock, and the purple solid lines represent the magnetic obstacle start and end times.

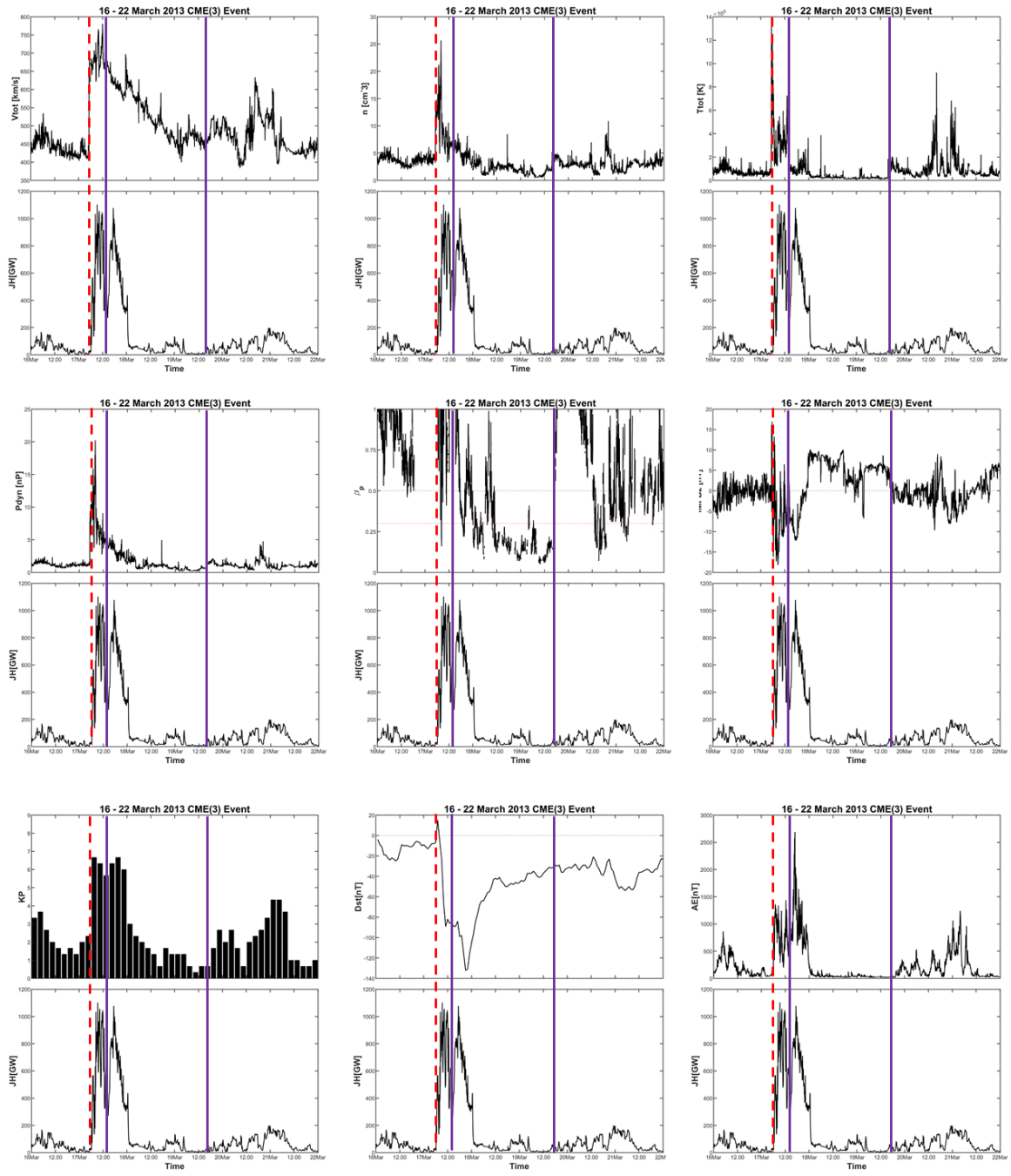

Figure A.3 : Time series of JH with 9 parameters for CME 3, in which the red dashed line represents the shock, and the purple solid lines represent the magnetic obstacle start and end times.

APPENDIX B

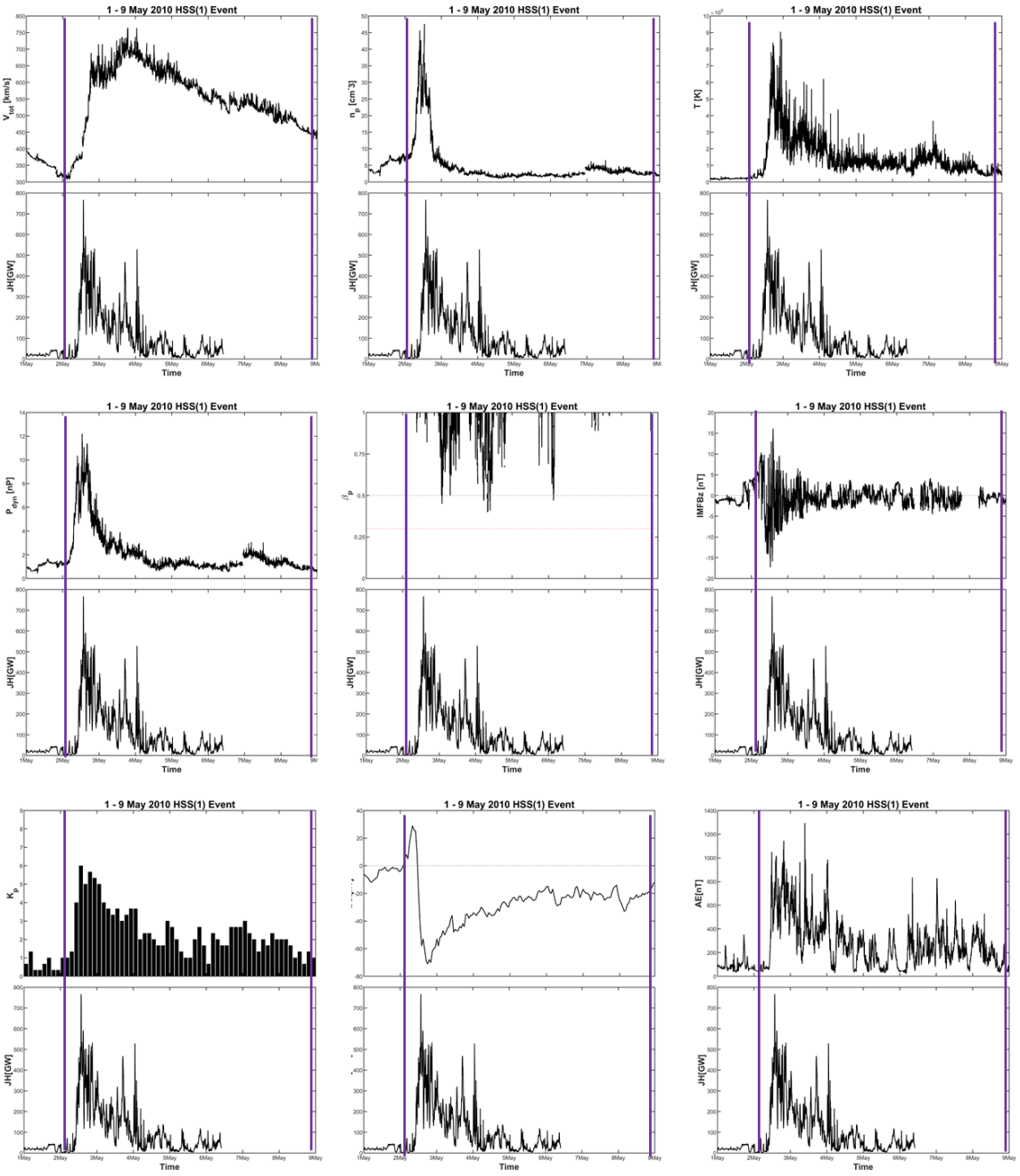

Figure B.1: Time series of JH with 9 parameters for HSS 1, in which the red dashed line represents the shock, and the purple solid lines represent the magnetic obstacle start and end times.

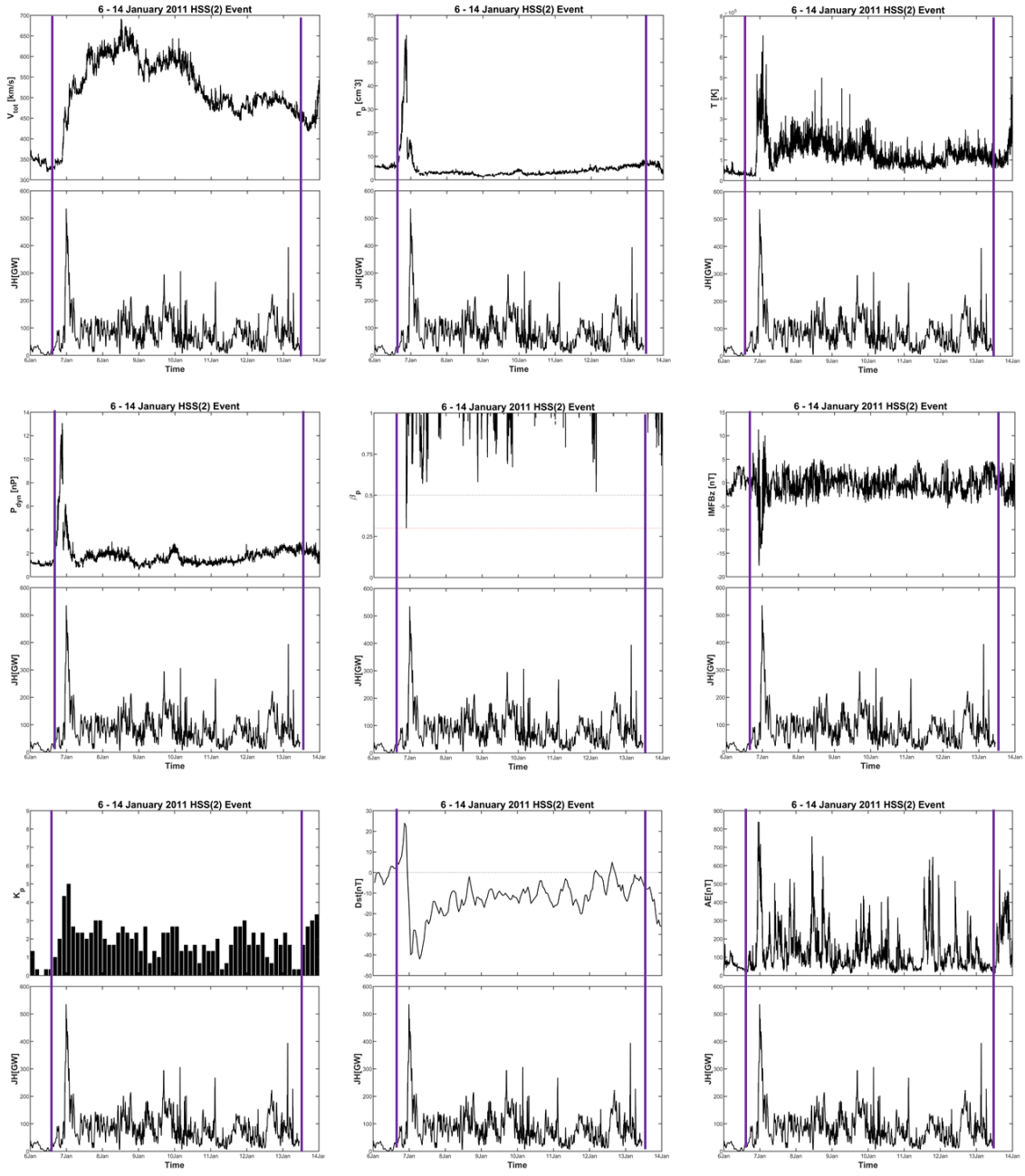

Figure B.2: Time series of JH with 9 parameters for HSS 2, in which the red dashed line represents the shock, and the purple solid lines represent the magnetic obstacle start and end times.

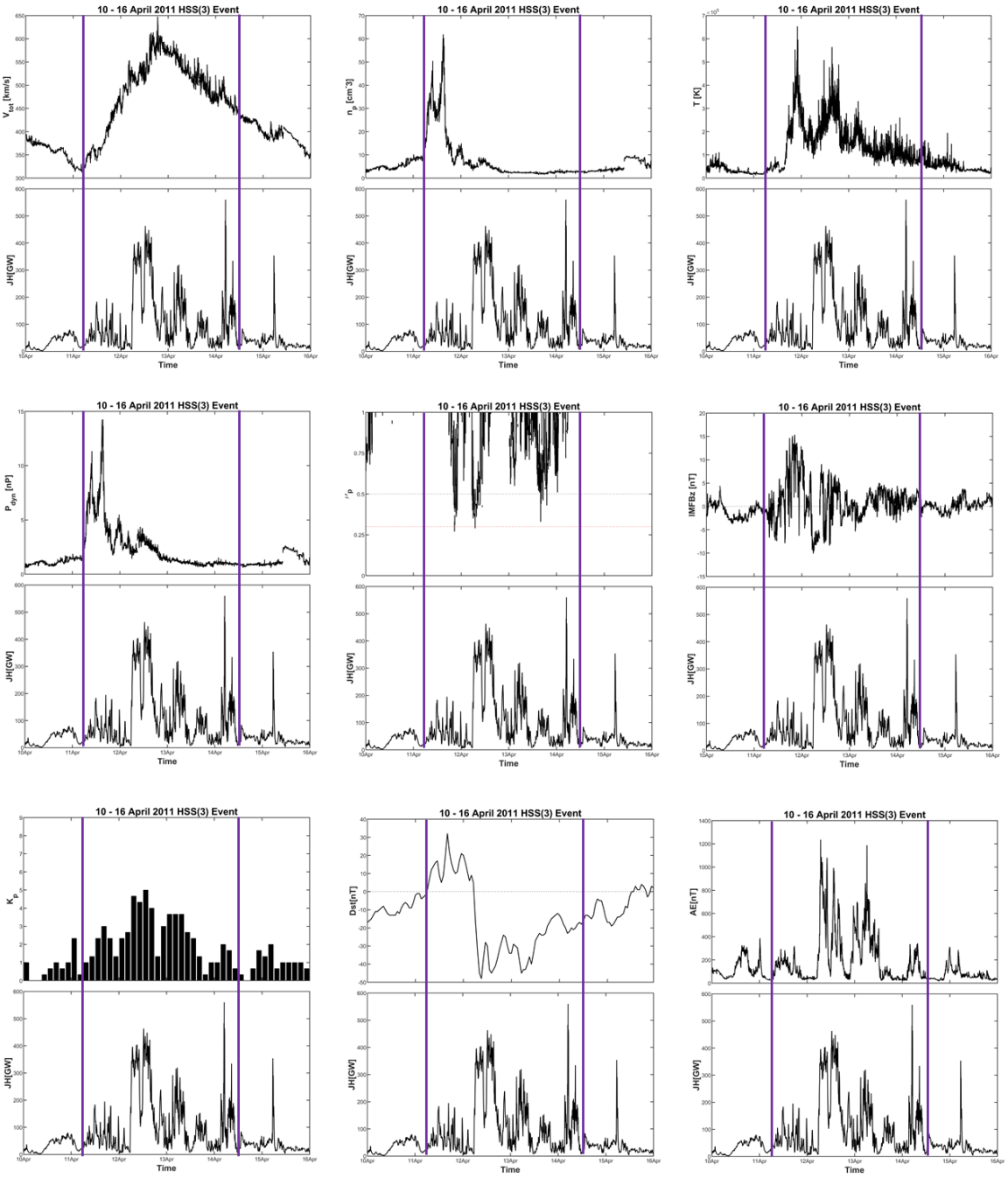

Figure B.3: Time series of JH with 9 parameters for HSS 3, in which the red dashed line represents the shock, and the purple solid lines represent the magnetic obstacle start and end times.

APPENDIX C

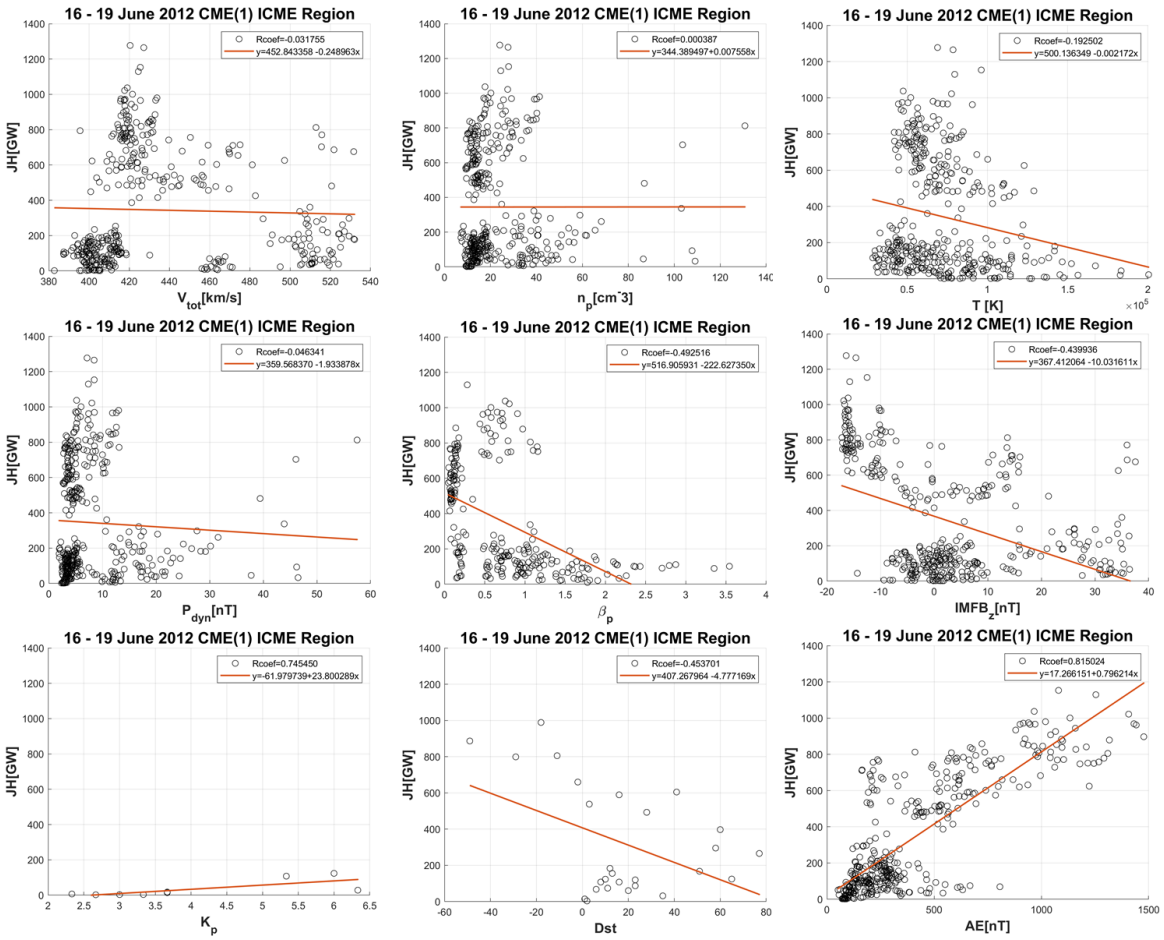

Figure C.1: SLR analysis of JH with 9 parameters for ICME interval of CME 1.

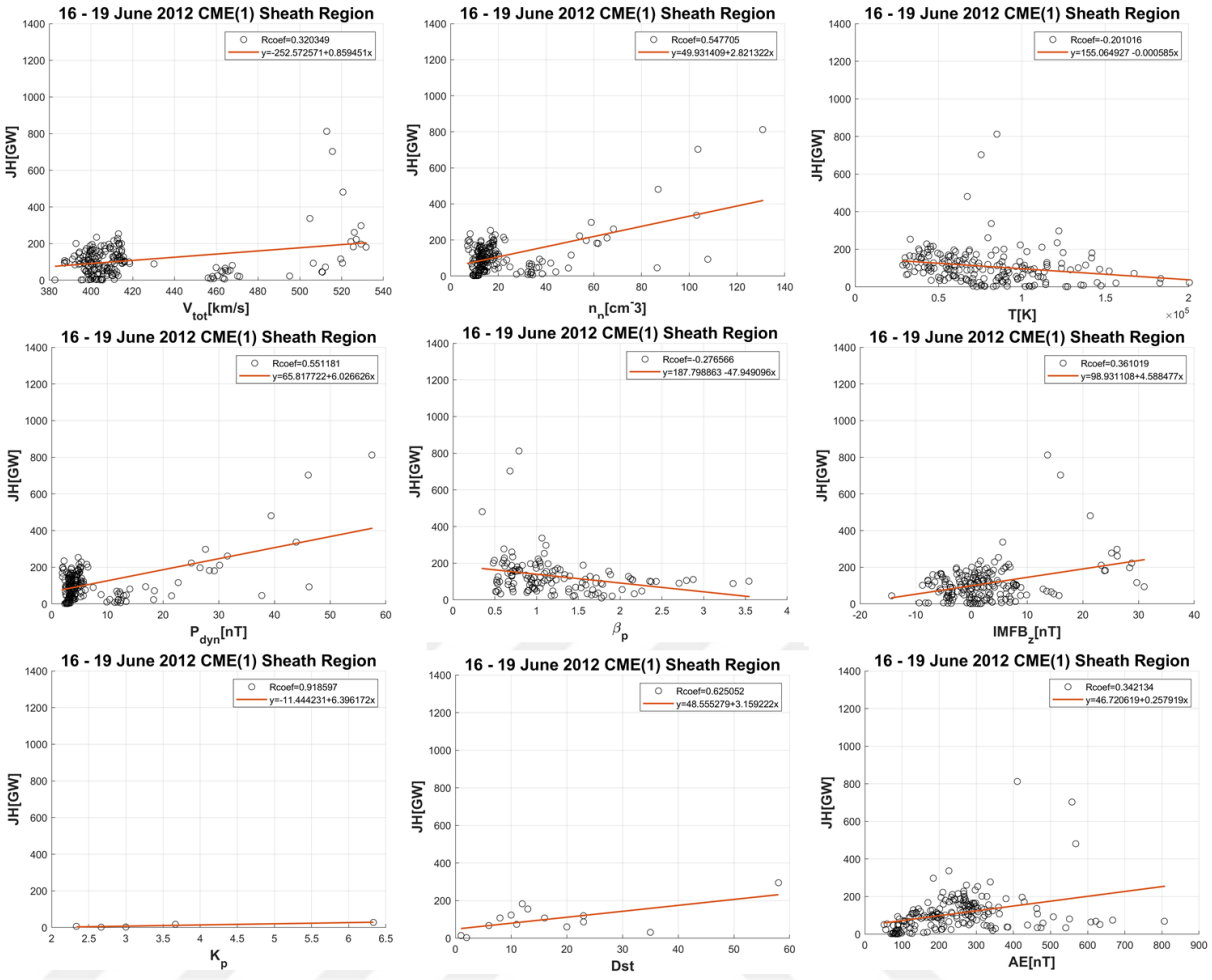

Figure C.2: SLR analysis of JH with 9 parameters for SH interval of CME 1.

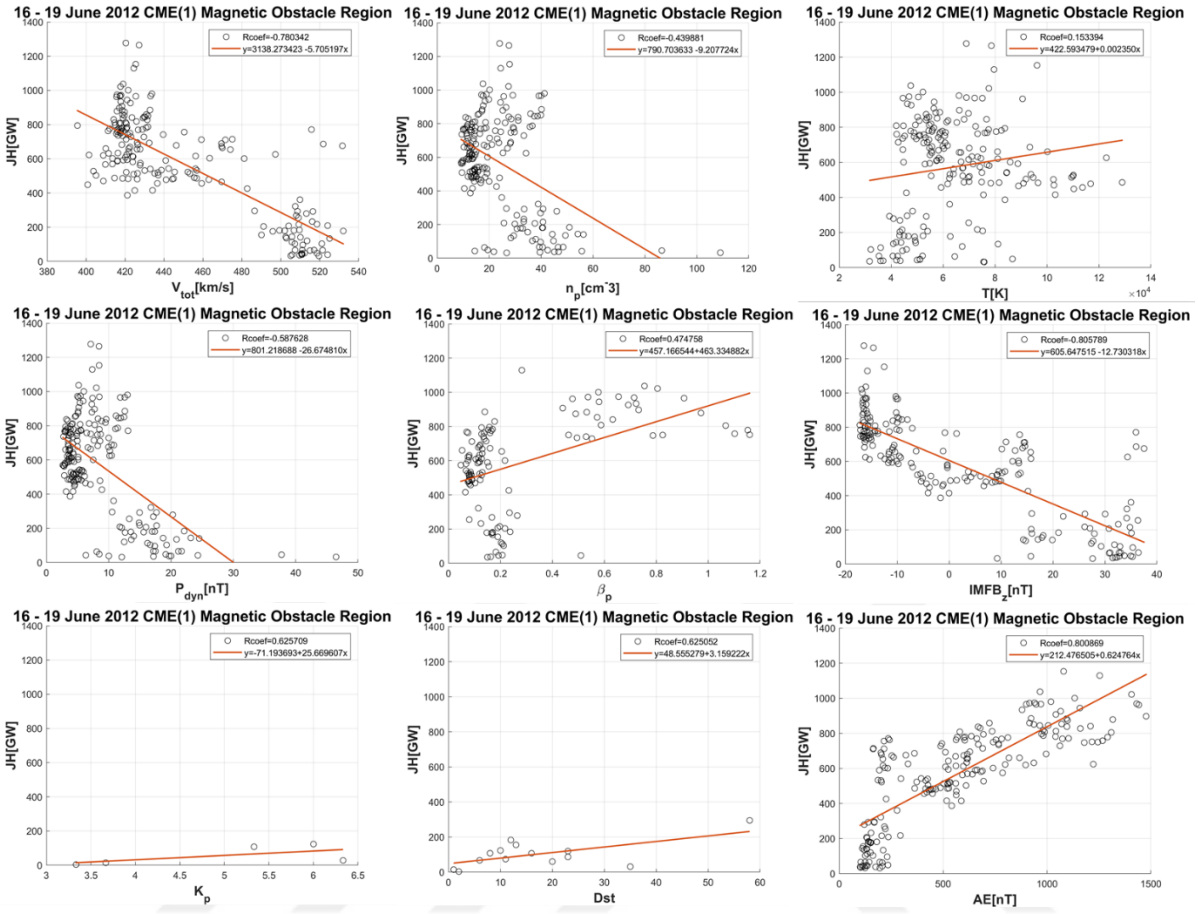

Figure C.3: SLR analysis of JH with 9 parameters for MO interval of CME 1.

APPENDIX D

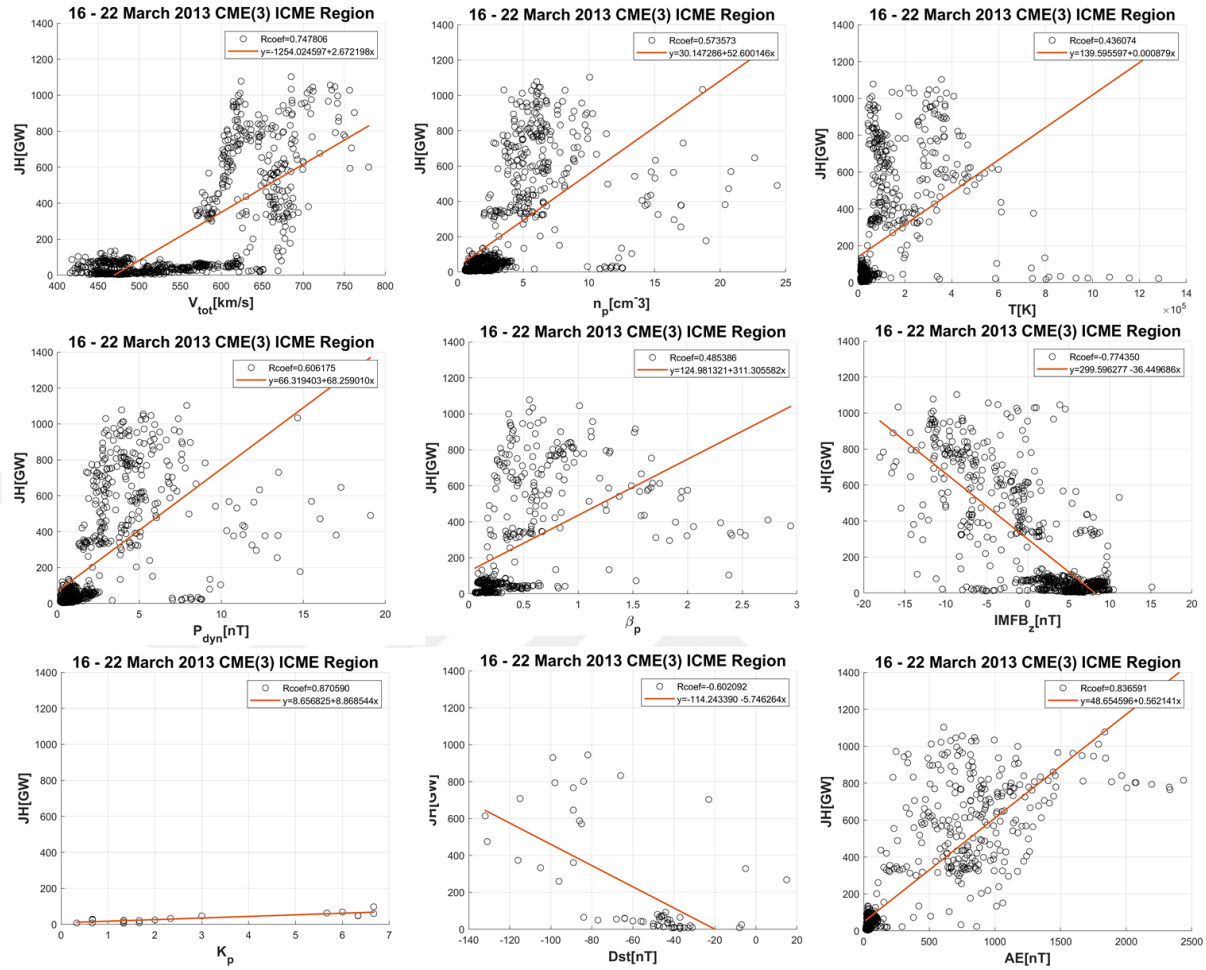

Figure D.1: SLR analysis of JH with 9 parameters for ICME interval of CME 3.

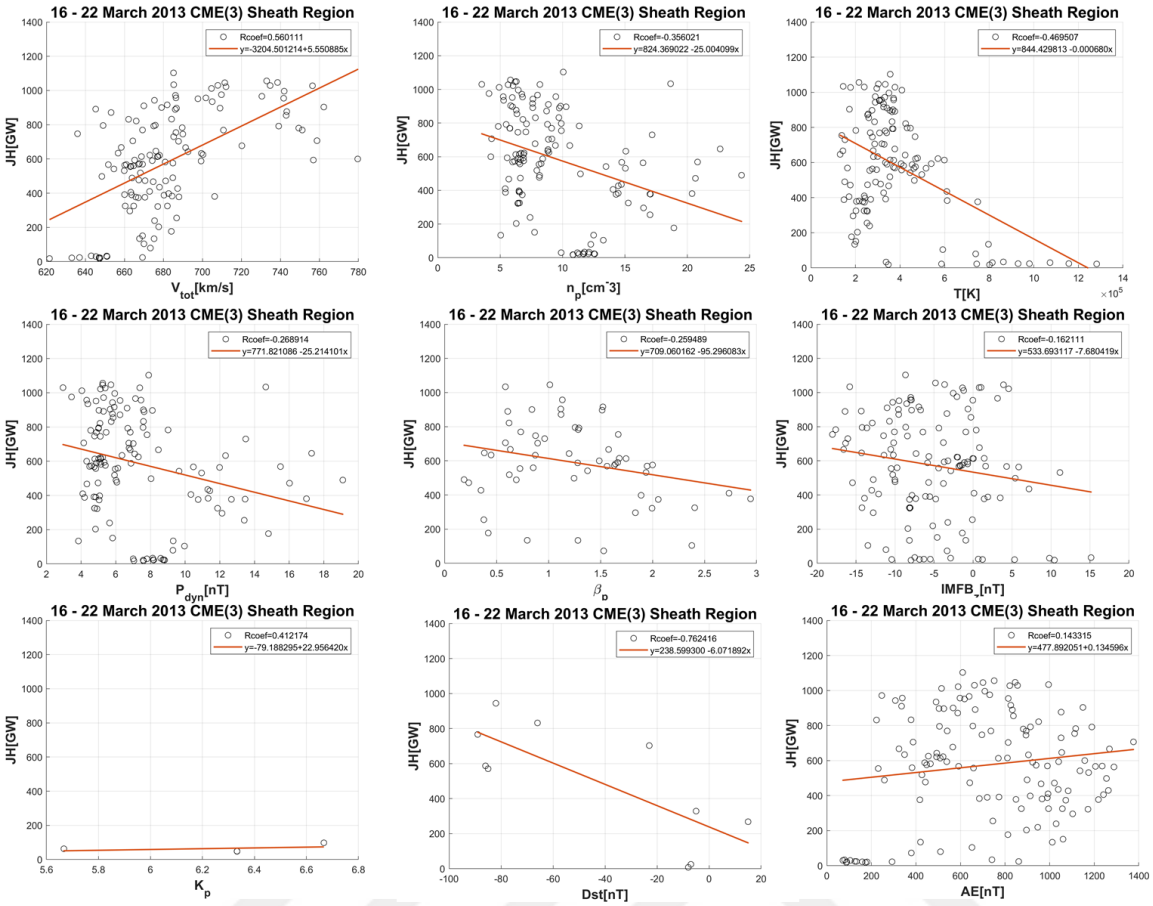

Figure D.2: SLR analysis of JH with 9 parameters for SH interval of CME 3.

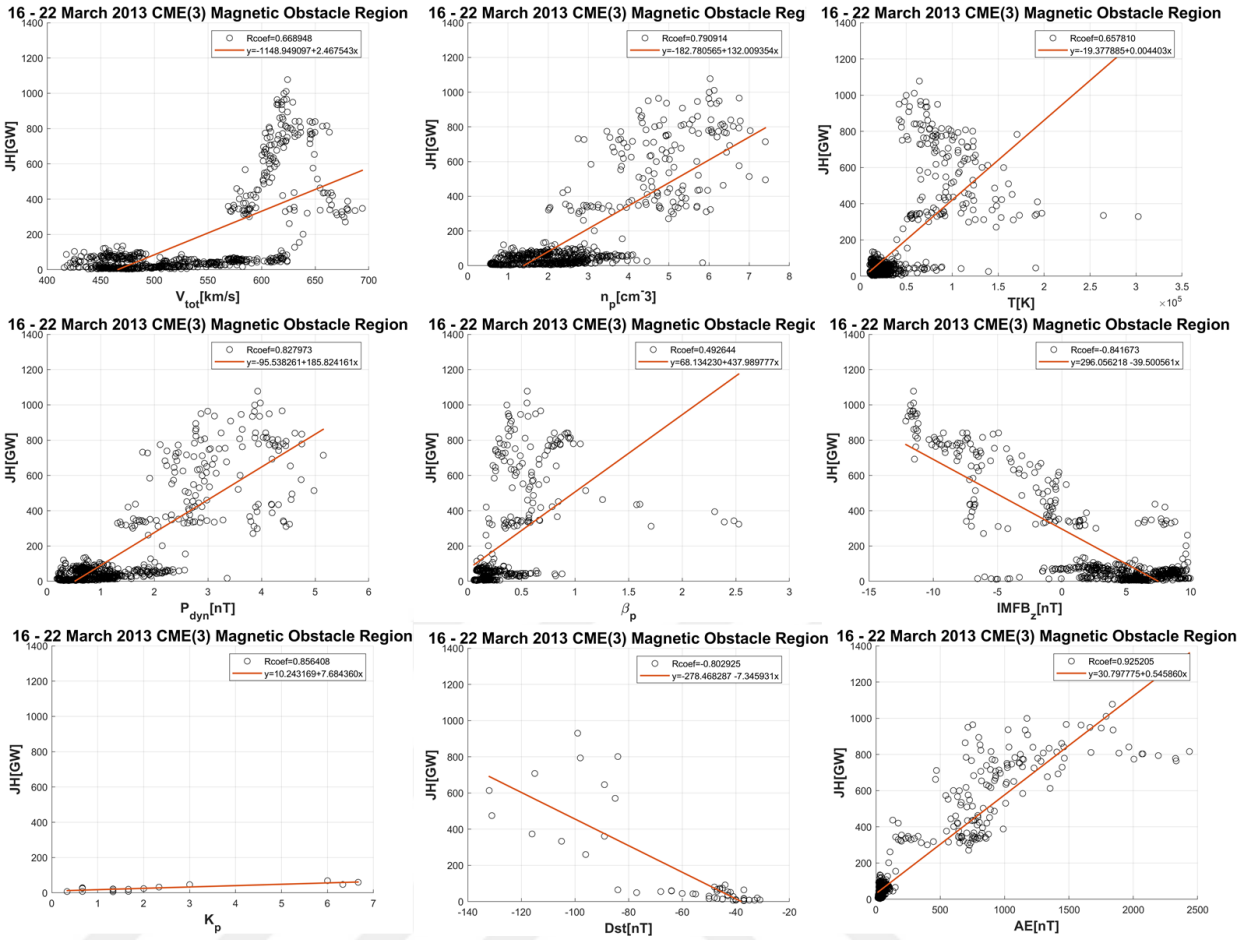

Figure D.3: SLR analysis of JH with 9 parameters for MO interval of CME 3.

APPENDIX E

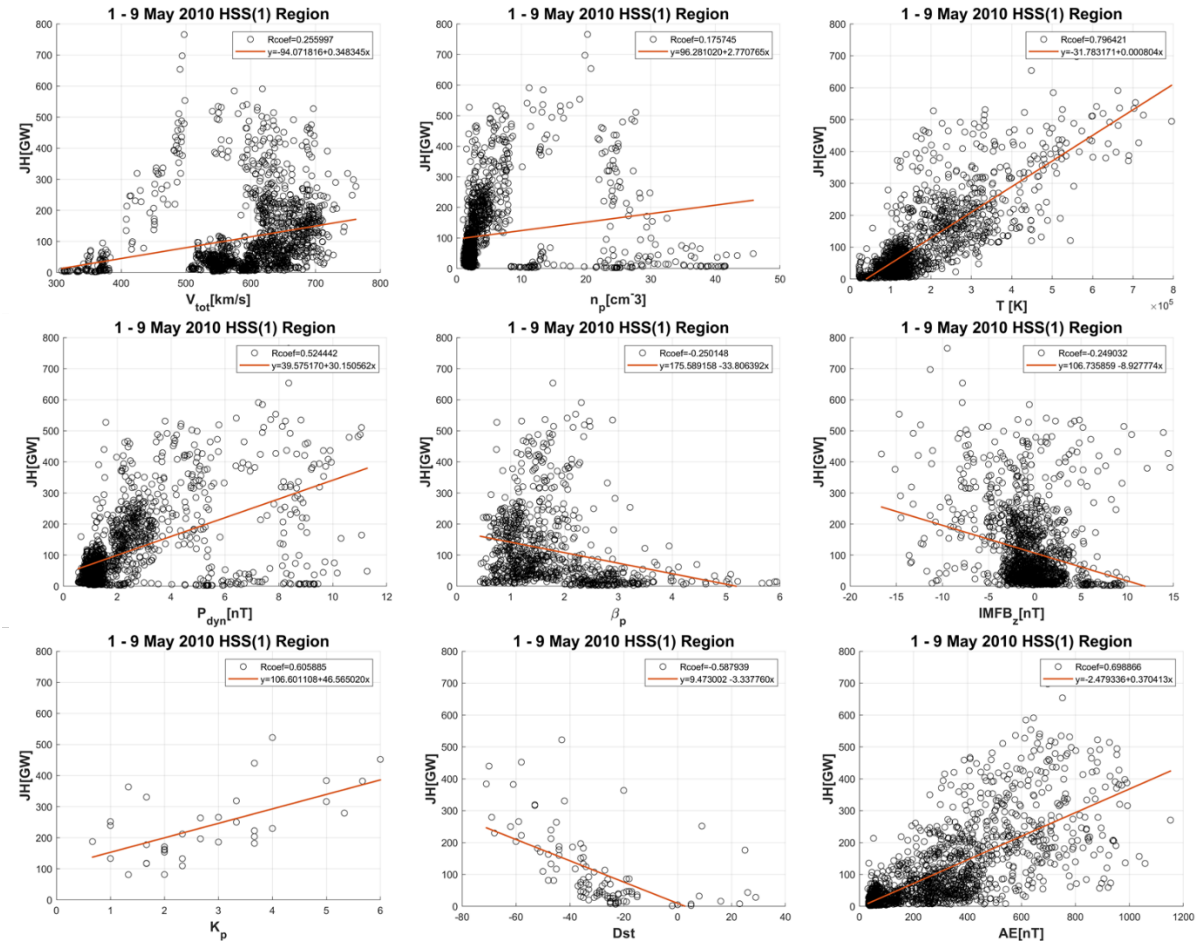

Figure E.1: SLR analysis of JH with 9 parameters for HSS 1 interval.

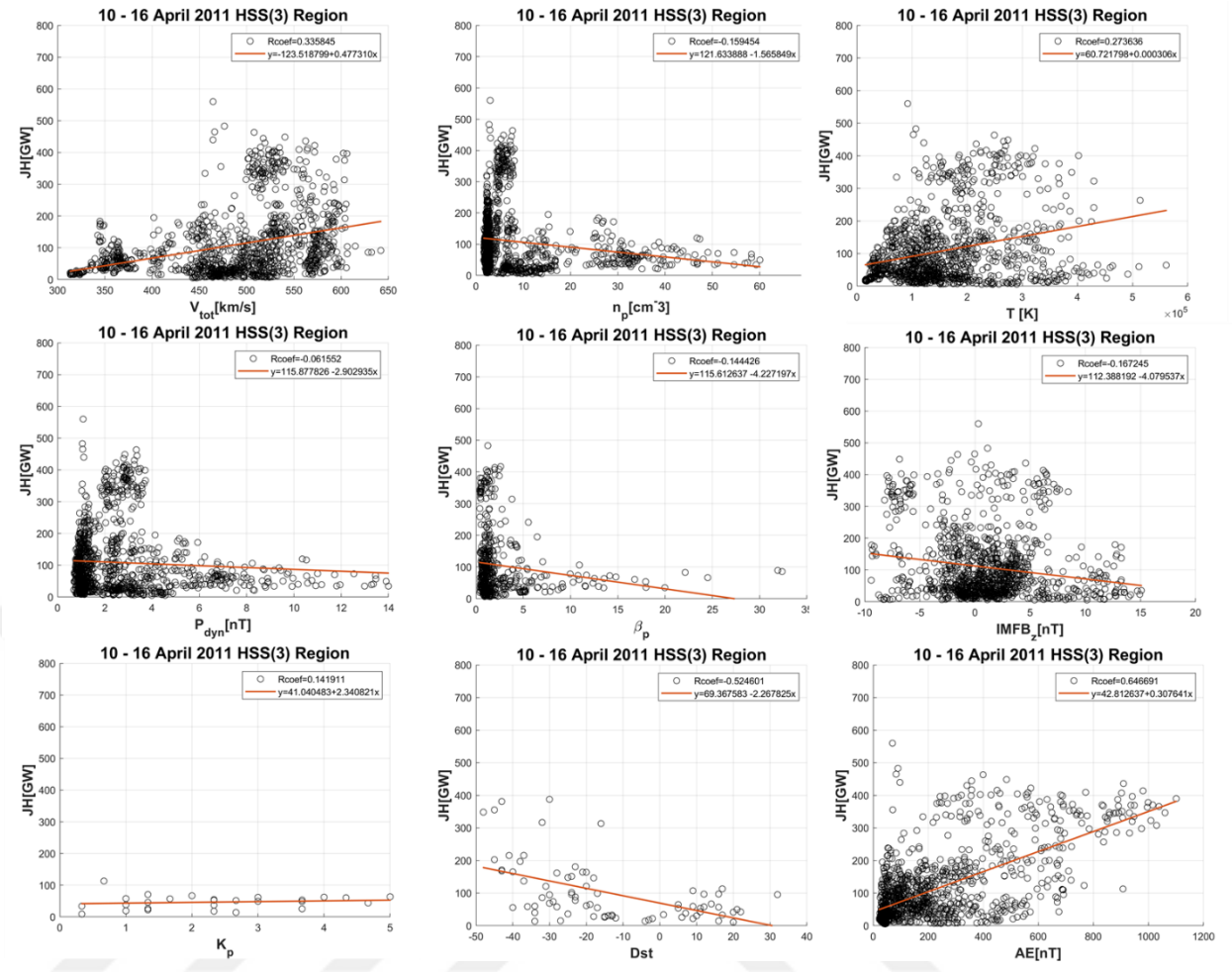

Figure E.2: SLR analysis of JH with 9 parameters for HSS 3 interval.

CURRICULUM VITAE

Name Surname **:** Pelin ERDEMIR

EDUCATION

- **M.Sc.** **:** 2022, Istanbul Technical University, Faculty of Aeronautics and Astronautics, Department of Meteorological Engineering, Programme of Atmospheric Sciences
- **B.Sc.** **:** 2020, Istanbul Technical University, Faculty of Aeronautics and Astronautics, Meteorological Engineering
- **Double Major** **:** 2016-2018, Istanbul Technical University, Faculty of Aeronautics and Astronautics, Astronautical Engineering

PROFESSIONAL EXPERIENCE AND REWARDS:

- 2020-now, Research Assistant at Istanbul Technical University, Faculty of Aeronautics and Astronautics, Department of Meteorological Engineering

CONFERENCES & PROCEEDINGS

- **P. Erdemir, Z. Kaymaz, E. C. Kalafatoglu Eyiguler & L. Rastaetter,** 'Dependence of Joule heating on ICME parameters', *The General Assembly 2022 of the European Geosciences Union (EGU)*, May 23-27, 2022, Vienna, Austria. (Oral contribution) https://meetingorganizer.copernicus.org/EGU22/EGU22-481.html
- **P. Erdemir, Z. Kaymaz, E. C. Kalafatoglu Eyiguler & L. Rastaetter,** 'Investigation of CME and HSS driven Joule heating during high geomagnetic activity using MHD model', *Central European Astrophysical Bulletin*, 2022, Zagreb, Croatia. (accepted for publication)
- **P. Erdemir, Z. Kaymaz, E. C. Kalafatoglu Eyiguler & L. Rastaetter,** 'Investigation of CME and HSS driven Joule heating during high geomagnetic activity using BATS-R-US MHD model', *XVIIth Hvar Astrophysical Colloquium*, September 20-24, 2021, Hvar, Croatia. (Poster contribution, p.47). https://oh.geof.unizg.hr/images/meetings/XVII-HAC/xvii-hac-abstract-book.pdf

- **P. Erdemir, Z. Kaymaz, E. C. Kalafatoglu Eyiguler & L. Rastaetter,** 'Model comparisons of CME and HSS driven Joule heating', *3rd Joint Scientific IAGA-IASPEI Assembly 2021*, August 21-27, 2021, Hyderabad, India. (Oral and Poster contribution, p.370). http://iaga-iaspei-india2021.in/NGRI_IAGA%20IASPEI%202021%20(Final)_13%20Sep%202021.pdf
- **P. Erdemir, Z. Kaymaz, E. C. Kalafatoglu Eyiguler & L. Rastaetter,** 'A comparison of upper atmospheric Joule heating resulting from CMEs and HSSs using SWMF/BATS-R-US model', *The 3rd ISEE Symposium PWING-ERG conference and school on the inner magnetosphere*, March 8-12, 2021, Nagoya, Japan. (Oral contribution, p.16). https://is.isee.nagoya-u.ac.jp/pwing-erg/img/Abstract_book_v3.pdf

WORKSHOPS & SEMINARS

- **06.2022, 8th International HEPPA-SOLARIS Meeting –** Bergen, Norway (In-Person Participant with travel grant)
- **05.2022, Solar Orbiter School 2022 –** France, Sète (In-Person Participant)
- **05.2022, EGU General Assembly 2022 –** Austria, Vienna (In-Person Participant with travel grant)
- **11.2021 ,2-3 Nov The ISWI Workshop on Space Weather –** UNOOSA (Online Attendee)
  09.2021, XVIIth Hvar Astrophysical Colloquium – Hvar Observatory, Croatia (Online Participant)
- **08.2021, IAGA-IASPEI 2021 -** CSIR /National Geophysical Research Institute, India (Online Participant)
- **07.2021, The Geospace Environment Modeling (GEM) Virtual Workshop –** NSF/Division of Atmospheric Sciences, US (Online Participant)
- **07.2021, Iberian Space Science Summer School –** University of Coimbra, Portugal & University of Alcalá, Spain (Online Attendee)
- **07.2021, First Summer School on Space Research, Technology and Applications -** National Astronomical Observatory, Rozhen, Bulgaria (Online Student Participant-granted)
- **05.2021, 24-26 May SolFER 2021 Spring Meeting –** NASA/SolFER (Online Attendee)
- **05.2021, 5-7 May Heliophysics 2050 Workshop** – USRA/Lunar and Planetary Institute (Online Attendee)
- **03.2021, The 3rd ISEE Symposium PWING-ERG conference and school on the inner magnetosphere -** Nagoya University/ISEE – (Online Participant)
- **11.2017,8th Atmospheric Sciences Symposium –** İstanbul Technical University (Attendee)
- **07.2017, 4th Turkey Climate Change Congress –** Water Foundation, ITU, Medipol University (Attendee)